UNIVERSITY OF OKLAHOMA

GRADUATE COLLEGE

X-RAY CRYSTAL STRUCTURES AND CHARACTERIZATION OF THE PRODUCTS FROM THE INTERACTIONS OF MYOGLOBIN WITH NITROGEN OXIDES AND ARYLHYDRAZINES, AND NITROREDUCTASE INTERACTIONS WITH ORGANIC NITRO COMPOUNDS

A DISSERTATION

SUBMITTED TO THE GRADUATE FACULTY

in partial fulfillment of the requirements for the

Degree of

DOCTOR OF PHILOSOPHY

By

BING WANG
Norman, Oklahoma
2016

X-RAY CRYSTAL STRUCTURES AND CHARACTERIZATION OF THE PRODUCTS FROM THE INTERACTIONS OF MYOGLOBIN WITH NITROGEN OXIDES AND ARYLHYDRAZINES, AND NITROREDUCTASE INTERACTIONS WITH ORGANIC NITRO COMPOUNDS

A DISSERTATION APPROVED FOR THE
DEPARTMENT OF CHEMISTRY AND BIOCHEMISTRY

BY

_____
Dr. George B. Richter-Addo, Chair

_____
Dr. Ann H. West

_____
Dr. Kenneth M. Nicholas

_____
Dr. Jun Li

_____
Dr. Jessica Ruyle

I dedicate this work to my mom, Yongying Zhou, an angel from God in my mind.

I wish her still to be peaceful and enjoyable in Heaven.

Acknowledgements

First of all, I would like to thank my supervisor Dr. George B. Richter-Addo for his endless support and faith in me in my research experiments, writing, and personal behavior. His careful scientific attitude and hard work impressed me a lot. He always properly teaches me in detail with his deep knowledge in both biochemistry and inorganic chemistry and guides me to continuously look for the unknown with his patience. I appreciate his help!

I also appreciate the help from my advisory committee members: Dr. Ann H. West, Dr. Kenneth M. Nicholas, Dr. Jun Li, and Dr. Jessica Ruyle. I also thank Dr. David Nagle who was previously on my committee prior to his retirement. I would like to thank Dr. Leonard M. Thomas, the manager of our macromolecular X-ray lab, for his help with X-ray crystallography.

I enjoyed the five years of Ph.D. life in our lab with our current and past group members: Dr. Nan Xu, Dr. Jun (Eva) Yi, Dr. Adam Warhausen, Dr. Ye Guan, Dr. Dennis Awasabisah, Erwin G. Abucayon, Neda Hessami, and Samantha M. Powell. I gained a lot when I communicated with them from both the inorganic and biochemistry side regarding scientific questions. Special thanks to Neda for what she has done for our MFP project, and I thank Samantha for our exchange of views in our field and her kind revision of my English writing all the time, and I also thank Erwin for the assistance of IR spectroscopy.

I also would like to thank our collaborators, the group members from Dr. Ann H. West's group: Dr. Smita K. Menon, Jamie R. Sykes, and Skyler D.

Hebdon, a group member from Dr. Elizabeth A. Karr's group: Dr. Catherine E. Bishop, our specialist Dr. Fares Z. Najar and Dr. Philip C. Bourne, and also our collaborators in New York, the Albert Einstein College of Medicine (AECOM) team. Dr. Najar has been helpful to us in the bioinformatics field, and in all kinds of research conversations. I thank Dr. Menon for her suggestions on research.

Last but not least, I thank my family, my dad, Yijun Wang, and my mom, Yongying Zhou, for their everlasting, unrequited, constant support and faith, my wife, Jianlan You for what she has done and what she has sacrificed for my family, and my cute daughter, Carrieann K. Wang. Thank God for bringing these wonderful people to be around me!

Table of Contents

List of Tables

List of Figures

Abstract

This thesis describes research into the roles that metalloproteins and non-metalloproteins play in the biological inorganic/organic chemistry of common nitrogen oxides. There are three main chapters on this work: the first details the reactions of wild-type and mutant myoglobins (Mbs) in their interactions with nitrite and nitric oxide (NO), the second deals with these Mbs and their formation of bioorganometallic derivatives when reacted with arylhydrazines, and the third deals with an FMN-dependent nitroreductase enzyme and its reactions with the clinically relevant metronidazole drug.

Mutations to the distal pocket in the active site of Mb were made; specifically, the ferric-aqua derivatives of the H64A, H64Q, and V68A/I107Y mutants were expressed, purified, crystallized, and their crystal structures solved to 1.78-1.85 Å resolution. The proteins crystallized in either the $P2_1$ (wt, H64Q, V68A/I107Y) or *P6* (H64A, H64Q) space groups. The crystals were soaked with nitrite to form their *O*-bonded MbIII(ONO) complexes whose structures were also solved to 1.57-1.85 Å resolution. In the case of the H64A distal pocket mutant missing the H-bonding amino-acid residue in the 64th position, a water bridge was observed to form linking the protein exterior with the bound nitrite ligand, thus replacing the expected wt H64 H-bonding feature. Further, we noted that the distal pocket Val68 residue adapted its conformation to accommodate the nitrite ligands in some of these complexes. Notably, the *O*-binding modes observed in the four structures wt Mb(ONO), H64A-Mb(ONO), H64Q-Mb(ONO), and V68A/I107Y-Mb(ONO) held up exceedingly well even

with the variation in H-bonding capacities. These wt and mutant Mb(ONO) compounds can be reduced with sodium dithionite to their respective nitrosyl Mb(NO) products. Surprisingly, although the precursor nitrite Mb(ONO) compounds had similar Fe-ONO orientations in the protein active site pockets, two different orientations of the Fe-NO moieties in the products were observed; one had the NO ligand tilted and pointing towards the hydrophobic protein interior (for wt and V68A/I107Y), whereas the other had it pointing towards the hydrophilic protein exterior (for H64A and H64Q). Verification of the formation of the nitrosyl Fe-NO derivative, and not the closely related nitroxyl Fe-HNO, was provided by FT-infrared spectroscopy.

Arylhydrazines and derivatives are prevalent in nature and in pharmaceutical drugs. They interact with various heme proteins resulting in deactivation of the proteins. Eleven X-ray crystal structures of the products from the reactions of wt and mutant (H64A, H64Q, V68A/I107Y) Mbs with arylhydrazines (ArNHNH2; Ar = Ph, *m*-tol, and *p*-chlorophenyl) were obtained to 1.70-1.98 Å resolution. Direct Fe-carbon bonds were observed in all these derivatives, establishing that the hydrazine -NHNH2 moieties had been released from the reagents during their reactions with the Fe centers of the Mbs. Importantly, the C-atoms coordinating to the Fe centers were the same as those that bonded to the hydrazine functional groups, implying that the carbon-based radical intermediates were formed in close proximity to the Fe centers allowing for facile and efficient reactions to give the bioorganometallic Mb-aryl products. Significant distal pocket amino acid movements were observed in

some cases with the larger *p*-chlorophenyl ligand aryl; for example, in the H64Q-chlorophenyl derivative, the Gln64 residue swings to a position outside the pocket towards the solvent region.

We report the first expression, purification, crystallization, and X-ray crystal structure of a nitroreductase (NR) protein from the hypervirulent *Clostridium difficile* R20291 strain. This NR protein was isolated in dimeric form, and possesses the classical NR fold, with one FMN cofactor per monomer. The crystal structure was solved to 2.1 Å resolution, and shows a phosphate anion in one of the active sites. Evidence of functional nitroreductase capacity was demonstrated by the ability of the reduced NR protein to reduce a commonly prescribed drug for *C. difficile* infections, namely metronidazole.

Chapter 1 Introduction

In Dr. Richter-Addo's lab, we are mainly interested in the structures and reactivities of heme active sites in hemeprotein derivatives (hemeprotein + ligand). We examine the interactions of hemeproteins with endogenous and exogenous small molecules. We are also interested in the mode of attachments of these ligands to heme iron, and the effect of distal amino acid residues on ligand binding and reactivity.

Hemeproteins containing heme prosthetic groups are a group of metalloproteins that broadly exist in nature and are also intensively explored due to their diverse biological functions ranging from oxygen binding and transport (e.g., hemoglobin (Hb) and myoglobin (Mb)), electron transfer (e.g., cytochrome *c*), catalysis (e.g., cytochrome P450), to signaling (e.g., soluble guanylyl cyclase (sGC)) [1]. We currently focus on Hb and Mb. Hb and Mb are probably the most investigated heme-containing macromolecules. They occur widely in our body and are now believed to perform multiple roles. New functions of these two proteins, other than their known function as the oxygen carriers and storage units, have been assessed and some of these possible new functions are being studied. More attention has been drawn to these two proteins due to their new likely roles as nitrite reductases. Hb and Mb can reduce nitrite (NO_2^-) to nitric oxide (NO) which vasodilates blood vessels as a compensatory pathway for NO biosynthesis by nitric oxide synthase (NOS) during the hypoxia [2-4].

Sperm whale myoglobin (sw Mb) is used in this work. In *Chapter 2*, the interaction of Mb with nitrite and nitric oxide ligands is explored. Mb is a monomeric protein of ~18 kD. Mb can reduce nitrite to NO in the cardiomyocyte and in the rat heart [5, 6]. NO derived from Mb inhibits cellular respiration through binding to cytochrome *c* oxidase, limiting electron flow and oxygen utilization. In addition, knockout $Mb^{-/-}$ mice do not display the conversion of nitrite to NO, and exhibit a loss of nitrite protection against myocardial infarction [6]. Based on these results, Mb is suggested to behave as an intrinsic nitrite reductase that regulates cardiac function [7]. X-ray crystallography allows us to examine the interactions of Mb with nitrogen oxide ligands. Different mutants around the heme distal pocket were prepared in this work to investigate the effect of these residues on ligand binding modes and orientations. The liganded complexes of the wild-type and mutant Mbs were characterized by UV-vis, protein IR spectroscopy, and X-ray crystallography.

Humans encounter an increasing number of exogenous compounds, including environmental contaminants from industrial factories and pharmaceutical companies. Hemeproteins can be inhibited by metabolites of these compounds through the formation of organometallic iron-carbon (Fe-C) bonds. For example, cytochrome P450 can interact with phenylhydrazine, an intermediate in the synthesis of various dyes and pharmaceuticals in industry, to form Fe-phenyl complexes resulting in the inhibition of P450 activity [8-10]. A similar result was also observed in Mb [11-13]. The sw Mb protein is used in *Chapter 3* to investigate its interaction with arylhydrazines. X-ray

crystallography and UV-vis spectroscopy are the main characterization tools used in this work.

Clostridium is a Gram-positive bacterium, which includes several significant human pathogens, such as *Clostridium botulinum* and *Clostridium difficile* [14]. One of our projects, funded by the Price Family Foundation, focuses on finding druggable targets in the hypervirulent *Clostridium difficile* strain R20291. While searching for iron-sulfur metalloproteins from R20291 (these iron-sulfur proteins are important in energy metabolism [15]), we also found some other interesting targets, e.g. nitroreductases, which are FMN-containing proteins. In bacteria, nitroreductases are non-metal enzymes that catalyze the reduction of nitro-containing compounds to produce toxic hydroxylamines. One of the commonly used antibiotics is the nitro compound, metronidazole. Nitroreductases are implicated with metronidazole resistance *C. difficle*. We are interested in the interaction of nitroreductases and metronidazole, and have employed X-ray crystallography and UV-vis spectroscopy to examine this protein and the interaction with metronidazole. This work is described in *Chapter 4*.

1.1 Metal containing hemeproteins interact with nitrogen oxides

The research history of the inorganic nitrite salt seems like riding on a roller coaster. It is filled with controversies. Writing this Ph.D. thesis provided me with a good opportunity to examine this area.

Nitrate and nitrite were used to preserve food >5000 years ago [16]. An ancient written document originating in 8th century China described people using nitrate/nitrite to treat cardiovascular disorders [7]. In the 19th century, nitrite rather than nitrate was used in curing and preserving meats in industry, after it was realized that nitrate is reduced to nitrite by bacteria (see equation 1-1) [17]. Nitrite serves three functions in the preservation of meats. Nitrite contributes to the fresh-like pink color of cured meat caused by the formation of Mb-NO from the reaction of nitrite and Mb, enhances flavor due to the inhibition of rancid smell, and enables a longer shelf life because of the growth inhibition of *Clostridium botulinum* [15, 17, 18].

$$NO_3^- + e^- + 2H^+ \longrightarrow NO_2^- + H_2O \qquad (1\text{-}1)$$

The health concern of nitrate/nitrite, from both academic and public realms, began drawing more attention in the 1950s because carcinogenic *N*-nitrosamines [19] from nitrate/nitrite were identified from heated or cooked nitrite treated meats [20-22]. On the other hand, it was doubted that nitrate/nitrite was the direct link to cancer because treated meats also contain many other “harmful” components such as saturated fat [23]. Although the controversy still exists, these data helped enable the strict control of the nitrate/nitrite levels in food and drinking water. Nitroso compounds can also

form from the reactions of nitrite with various peptides or amino compounds in the acidic environment of the stomach [15]. Much more attention in the scientific community has been put into the possible link of ingested nitrite and gastric cancer [24-27]. However there is no conclusive evidence to date that directly links the carcinogenicity to nitrate/nitrite [25, 28].

The endogenous nitrite in mammals can derive from the oxidation of nitric oxide (NO), which is an important signaling gas molecule and serves many physiological functions, including host defense in the immune system, regulation of blood flow as a vasodilator, platelet activity and aggregation, and leukocyte trafficking [29-37]. NO is biosynthesized from L-arginine oxidation by nitric oxide synthases (NOS) in the presence of oxygen (see the scheme below) [38]. The reduced NO bioactivity in vasculature has been associated with cardiovascular diseases induced by inflammation, aging, hypertension, hypercholesterolemia, smoking, diabetes, postmenopause, and physical inactivity [32-37].

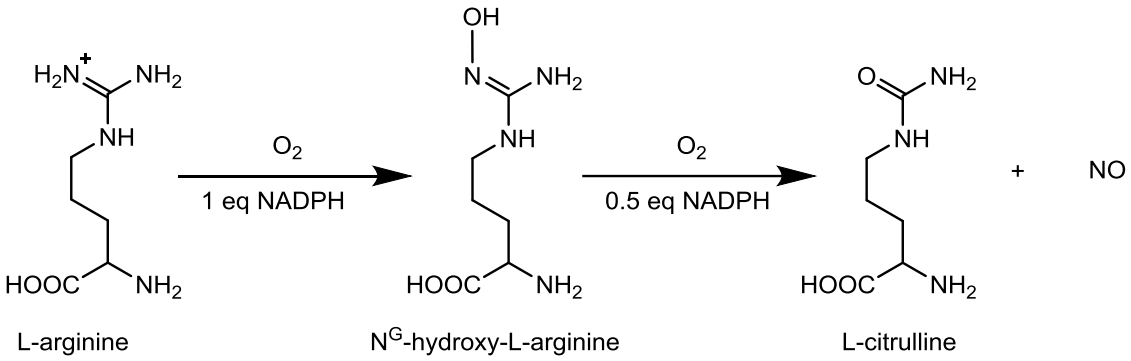

It is interesting to point out that once NO is formed from NOS, it will be quickly converted to nitrate by oxymyoglobin ($Mb^{II}O_2$) or nitrite by the ceruloplasmin in plasma [39]. Are these nitrite molecules a threat to our health? The answer is obviously “NO”. Despite public anxiety regarding nitrite exposure, some seminal work has been reported in the recent 20 year period that suggests nitrite to be a vital nitrite oxide reservoir no matter where the nitrite comes from [7, 18, 40, 41]. When nitrate/nitrite containing food is consumed, part of this nitrate will be reduced to nitrite by the nitrate reductases from the bacteria in the oral cavity [42]. Mammals lack the enzymatic capacity to reduce nitrate to nitrite. The commensal bacteria provide a reciprocal metabolic pathway. The stomach can consume some of the nitrite by protonating the nitrite to form nitrous acid (HNO_2) [29, 30]. The remaining nitrate and nitrite will be absorbed by the intestine and enter into circulation [7]. The nitrite in blood can be reduced to NO by deoxyhemoglobin ($HbFe^{II}$) (see equation 1-2 below) under hypoxic conditions, and nitrite can work as a stable storage of NO [2-4, 43]. NO diffuses into the smooth muscle and dilates the vessels causing increased local blood flow to meet O_2 needs during ischemia or hypoxia [4].

Nitrite induced vasodilation is an important regulatory mechanism during hypoxia since endogenous NOS-synthesized NO with O_2 present will be limited.

$$NO_2^- + HbFe^{II} + H^+ \longrightarrow NO + metHbFe^{III} + OH^- \quad (1\text{-}2)$$

Deoxymyoglobin ($MbFe^{II}$), like Hb, can also reduce nitrite to NO like Hb [5, 6]. This implies that Mb may play similar roles as Hb in nitrite induced vasodilation. It was recently shown that Mb is expressed in the vasculature and contributes to nitrite induced vasodilation [44]. Mb also displays specific functions in vasodilation because it is mainly expressed in cardiomyocytes and muscle cells [45]. NO, from nitrite reduction by Mb, can interact with cytochrome *c* oxidase in the mitochondrial electron transport chain and further limit cellular respiration and oxygen usage [5]. We thus need a better understanding of the conversion of nitrite to NO. Possible treatments using nitrate/nitrite for hypertension [46, 47], tissue protection in ischemia-reperfusion (IR) injury [48-50], myocardial infraction [7], antimicrobial effects [51], and gastric ulcers [52] are currently being pursued by others .

It has been contended that nitrate/nitrite should be recognized as bioactive and indispensable nutrients, specifically for patients with a dysfunctional L-arginine-NOS pathway [53]. The supplementation of nitrate/nitrite in the diet has also been suggested for the treatment and prevention of cardiovascular disease [41]. However, it is undoubtable that nitrite is toxic to humans in high concentrations. The oxidation of oxyhemoglobin ($HbFe^{II}O_2$) by nitrite can produce methemoglobin with loss of oxygen binding capacity, and cause the acute methemoglobinemia. This can be fatal, especially

for infants. The “blue baby syndrome” caused by methemoglobinemia has been associated with high nitrate/nitrite intake [54]. Thus, toxicity and benefit coexists in nitrate/nitrite, just like with most other chemical drugs.

This background explains why our lab focuses on the reactions between Hb/Mb and NOx, currently between Hb/Mb and nitrite/NO. We are interested in the binding modes of nitrite in Hb/Mb, the relative effects of heme distal pocket on the nitrite ligands, and NO orientation preferences in Hb/Mb. Mb is my target in this work as shown in *Chapter 2*. The Mb protein fold is shown in Fig. 1-1.

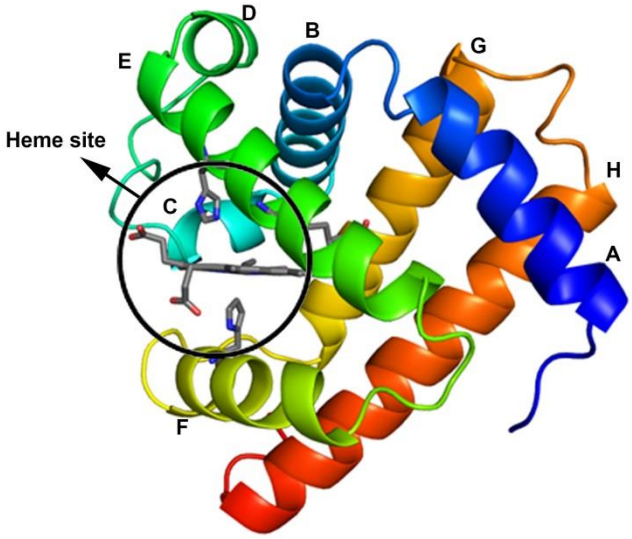

Fig. 1-1. Mb with each helix and heme site labled (PDB ID 2MBW [55]). The circled area shows the heme site. In the heme site, the area above heme containing His64 is called the “distal pocket”, and the area underneath the heme containing a proximal His93 is called the “proximal pocket”.

1.2 Metal containing hemeproteins react with arylhydrazines

Applied organometallic chemistry has been associated with the catalysis industry and diverse areas in biology and medicine, such as anticancer therapy [56], antibacterial [57], radioimaging [58], and fluorescent cell imaging [59]. The first association of organometallics with biology was with vitamin B_{12} or cobalamin which works in a variety of life processes using a metal-carbon bond [60]. Heme containing proteins can also involve organometallic chemistry when they react with arylhydrazines [61, 62].

As I detail in *Chapter 3*, arylhydrazines ($ArNHNH_2$; Ar = aryl) occur in nature and are important chemical species in both the agrochemical and pharmaceutical industries [63], and synthetic hydrazines are also prevalent in the general environment [64].

Phenylhydrazine is toxic to red blood cells [65], and the hemoglobin-phenylhydrazine interaction has been used to examine and model hemolytic anemia. Interactions of various substituted hydrazines with Mb [11-13], cytochrome P450 [8-10], and catalase [66] have been reported in the literature [67]. Direct organometallic bond Fe–C(aryl) linkages may form from these reactions.

New X-ray structural data that clarify which aryl C atoms bind to the Fe centers, and information regarding preferred aryl ligand orientations from reactions involving substituted arylhydrazines as a function of active site structure are thus desirable. My research in this area is described in *Chapter 3*.

1.3 Non-metal nitroreductases metabolize organic nitro compounds

Clostridium difficile infections (CDIs) cause ~14,000 deaths yearly out of the total ~250,000 cases reported by the CDC in 2013 [68]. Only two years later, these numbers doubled to ~29,000 deaths out of the total ~500,000 cases [69]. CDC labeled this pathogen as “Urgent” which is the top threat level [68]. CDIs result in at least $1 billion in excess medical costs every year [68]. *C. difficile* multiplies in the colon and causes life-threatening diarrhea [70]. The incidence and mortality rate are continuously increasing. One of the reasons is the frequent usage of antibiotics and chemotherapeutics which creates an imbalance in the intestinal flora and allow the rapid expansion of *C. difficile* [71]. Currently, metronidazole (MTZ) is a commonly prescribed drug for the treatment of CDI [72-74]. However, MTZ resistance has been reported recently [75, 76]. The search for the multiple therapeutic approaches is urgent, including the exploration of new therapeutic methods, the development of new drugs and the discovery of new druggable targets.

As a collaborative project, we contribute to the search for new therapeutic approaches to CDIs. Nitrite is applied in meat preservation due to its inhibition against the growth of pathogens, in particular *Clostridium botulinum [15]*. This antibacterial role of nitrite is actually due to NO formation [77]. NO is toxic to *Clostridium* by inactivating the iron-sulfur proteins which are important in bacterial energy metabolism [78]. Accordingly, *C. difficile* does display only a low concentration of nitrite reductase capacity [79], avoiding the generation of toxic NO. Sobko et al. [80] measured the NO gas generation from fecal and gut

bacteria. The data showed that *C. difficile* did not produce significant amounts of NO in the presence of either nitrate or nitrite. It was also reported that reduced gastric acidification from pH 2 to 5 caused the abolishment of nitrite reduction to NO and increased the risk of CDIs in patients [81]. These data suggest NO can be an efficient anti-CDI reagent. In fact, the antibacterial activity of NO against *Helicobacter pylori* has been assessed [52]. Both *H. pylori* and *C. difficile* colonize the lower gastrointestinal tract. The bactericidal effect of NO to *H. pylori* allows for hypothesis that NO could be used as the possible treatment for CDI. Our group focuses on the reaction mechanism of NO and iron-sulfur proteins (data not included in this thesis). We believe the knowledge of NO inhibition of *Clostridium* can result in future pharmaceutical applications.

While we were working on selected iron-sulfur proteins from *C. difficile*, another group of enzymes, namely nitroreductases, also attracted our attention. Nitroreductases in pathogens reduce nitro compounds to toxic hydroxylamines [82]. Many nitro-containing prodrugs are designed based on this characterization of nitroreductases. MTZ is also a nitro drug. The emergence of MTZ resistance is linked to the nitroreductases in *Helicobacter pylori* [83] and *Bacteroides fragilis* [84]. A frame-shift mutation in one of the nitroreductases in the hypervirulent *C. difficile* strain R20291 is associated with MTZ resistance [85]. Understanding nitroreductase interaction with MTZ is urgently needed to combat MTZ resistance in *C. difficile*. The crystal structure of an nitroreductase and its activity with MTZ is described in *Chapter 4*.

1.4 References

1. Lin, Y.W. and J. Wang, Structure and function of heme proteins in non-native states: a mini-review. *J. Inorg. Biochem*. **2013**, *129*, 162-71.
2. Brooks, J., The action of nitrite on haemoglobin in the absence of oxygen. *P. Roy. Soc B-Biol. Sci.* **1937**, *123*, 368-382.
3. Doyle, M.P., et al., Kinetics and Mechanism of the Oxidation of Human Deoxyhemoglobin by Nitrites. *J. Biol. Chem.* **1981**, *256*, 2393-2398.
4. Cosby, K., et al., Nitrite reduction to nitric oxide by deoxyhemoglobin vasodilates the human circulation. *Nat. Med*. **2003**, *9*, 1498-1505.
5. Shiva, S., et al., Deoxymyoglobin is a nitrite reductase that generates nitric oxide and regulates mitochondrial respiration. *Circ. Res*. **2007**, *100*, 654-661.
6. Rassaf, T., et al., Nitrite reductase function of deoxymyoglobin - Oxygen sensor and regulator of cardiac energetics and function. *Circ. Res.* **2007**, *100*, 1749-1754.
7. Lundberg, J.O., E. Weitzberg, and M.T. Gladwin, The nitrate-nitrite-nitric oxide pathway in physiology and therapeutics. *Nat. Rev. Drug. Discov*. **2008**, *7*, 156-67.
8. Battioni, P., et al., Reaction of Monosubstituted Hydrazines and Diazenes with Rat-Liver Cytochrome-P450 - Formation of Ferrous-Diazene and Ferric Sigma-Alkyl Complexes. *Eur. J. Biochem.* **1983**, *134*, 241-248.
9. Muakkassah, S.F. and W.C.T. Yang, Mechanism of the Inhibitory-Action of Phenelzine on Microsomal Drug-Metabolism. *J. Pharmacol. Exp. Ther.* **1981,** *219*, 147-155.
10. Raag, R., et al., Formation, Crystal-Structure, and Rearrangement of a Cytochrome-P-450cam Iron Phenyl Complex. *Biochemistry* **1990**, *29*, 8119-8126.
11. Ringe, D., et al., Reaction of Myoglobin with Phenylhydrazine: A Molecular Doorstop. *Biochemistry* **1984**, *23*, 2-4.
12. Swanson, B.A. and P.R. Ortiz de Montellano, Structure and Absolute Stereochemistry of the 4 N-Phenylprotoporphyrin-Ix Regioisomers Isolated from Phenylhydrazine-Treated Myoglobin. *J. Am. Chem. Soc.* **1991**, *113*, 8146-8153.
13. Ortiz de Montellano, P.R. and D.E. Kerr, Inactivation of Myoglobin by Ortho-Substituted Arylhydrazines. Formation of Prosthetic Heme Aryl-Iron but Not N-Aryl Adducts. *Biochemistry* **1985**, *24*, 1147-1152.
14. Hatheway, C.L., *Toxigenic Clostridia. Clin. Microbiol. Rev.* **1990**, *3*, 66-98.
15. Cammack, R., et al., Nitrite and nitrosyl compounds in food preservation. *BBA-Bioenergetics* **1999**, *1411*, 475-488.
16. Huffman, R. and N. Bryan, Nitrite and nitrate in the meat industry. Food, Nutrition and the Nitric Oxide Pathway: Biochemistry and Bioactivity. NS Bryan, ed. DESTech Publications Inc., Lancaster PA, **2010**.

17. Binkerd, E. and O. Kolari, The history and use of nitrate and nitrite in the curing of meat. *Food cosmet. toxicol.* **1975**, *13*, 655-661.
18. Bryan, N.S., Nitrite in nitric oxide biology: Cause or consequence? A systems-based review. *Free Radical Bio. Med.* **2006**, *41*, 691-701.
19. Magee, P.N. and J.M. Barnes, The Production of Malignant Primary Hepatic Tumours in the Rat by Feeding Dimethylnitrosamine. *Brit. J. Cancer* **1956**, *10*, 114.
20. Ender, F., et al., Isolation and identification of a hepatotoxic factor in herring meal produced from sodium nitrite preserved herring. *Naturwissenschaften* **1964**, *51*, 637-638.
21. Massey, R.C. and D. Lees, Surveillance of Preservatives and Their Interactions in Foodstuffs. *Food Addit. Contam.* **1992**, *9*, 435-440.
22. Gloria, M.B.A., J.F. Barbour, and R.A. Scanlan, Volatile nitrosamines in fried bacon. *J. Agr. Food Chem.* **1997**, *45*, 1816-1818.
23. Milkowski, A., et al., Nutritional epidemiology in the context of nitric oxide biology: A risk-benefit evaluation for dietary nitrite and nitrate. *Nitric Oxide-Biol. Ch.* **2010**, *22*, 110-119.
24. Eichholzer, M. and F. Gutzwiller, Dietary nitrates, nitrites, and N-nitroso compounds and cancer risk: A review of the epidemiologic evidence. *Nutr. Rev.* **1998**, *56*, 95-105.
25. Moller, H. Adverse health effects of nitrate and its metabolites: epidemiological studies in humans. in PotI Workshop,(Ed.), Health Aspects of Nitrates and its Metabolites (Particularly Nitrite), Council of Europe Press, Strasbourg Cedex, France. **1995**.
26. Bartsch, H. and R. Montesano, Relevance of nitrosamines to human cancer. *Carcinogenesis* **1984**, *5*, 1381-93.
27. Craddock, V.M., Nitrosamines and human cancer: proof of an association? *Nature* **1983**, *306*, 638.
28. Ward, M.H., et al., Workgroup report: Drinking-water nitrate and health-recent findings and research needs. *Environ. Health Persp.* **2005**, *113*, 1607-1614.
29. Benjamin, N., et al., Stomach No Synthesis. *Nature* **1994**, *368*, 502-502.
30. Lundberg, J.O.N., et al., Intragastric Nitric-Oxide Production in Humans - Measurements in Expelled Air. *Gut* **1994**, *35*, 1543-1546.
31. Bjorne, H., et al., Nitrite in saliva increases gastric mucosal blood flow and mucus thickness. *J. Clin. Invest.* **2004**, *113*, 106-114.
32. Cines, D.B., et al., Endothelial cells in physiology and in the pathophysiology of vascular disorders. *Blood* **1998**, *91*, 3527-61.
33. Quyyumi, A.A., Endothelial function in health and disease: new insights into the genesis of cardiovascular disease. *Am. J. Med.* **1998**, *105*, 32S-39S.
34. Naseem, K.M., The role of nitric oxide in cardiovascular diseases. *Mol. Aspects Med.* **2005**, *26*, 33-65.
35. Ajay, M., et al., Direct effects of quercetin on impaired reactivity of spontaneously hypertensive rat aortae: comparative study with ascorbic acid. *Clin Exp Pharmacol Physiol.* **2006**. *33*, 345-50.

36. Hadi, H.A., C.S. Carr, and J. Al Suwaidi, Endothelial dysfunction: cardiovascular risk factors, therapy, and outcome. *Vasc. Health Risk Manag.* **2005**, *1*, 183-98.
37. Hirata, Y., et al., Diagnosis and treatment of endothelial dysfunction in cardiovascular disease. *Int. Heart J.* **2010**, *51*, 1-6.
38. Marletta, M.A., Nitric oxide synthase structure and mechanism. *J. Biol. Chem.* **1993**, *268*, 12231-4.
39. Dejam, A., et al., Erythrocytes are the major intravascular storage sites of nitrite in human blood. *Blood* **2005**, *106*, 734-9.
40. Gladwin, M.T., et al., Nitrite as a vascular endocrine nitric oxide reservoir that contributes to hypoxic signaling, cytoprotection, and vasodilation. *Am. J. Physiol-Heart C.* **2006**, *291,* H2026-H2035.
41. Machha, A. and A.N. Schechter, Dietary nitrite and nitrate: a review of potential mechanisms of cardiovascular benefits. *European J. Nutr.* **2011**, *50*, 293-303.
42. Lundberg, J.O. and M. Govoni, Inorganic nitrate is a possible source for systemic generation of nitric oxide. *Free Radical Bio. Med.* **2004**, *37*, 395-400.
43. Nagababu, E., et al., Active nitric oxide produced in the red cell under hypoxic conditions by deoxyhemoglobin-mediated nitrite reduction. *J. Biol. Chem.* **2003**, *278*, 46349-46356.
44. Ormerod, J.O.M., et al., The role of vascular myoglobin in nitrite-mediated blood vessel relaxation*. Cardiovasc. Res.* **2011**, *89*, 560-565.
45. Totzeck, M., et al., Nitrite regulates hypoxic vasodilation via myoglobin-dependent nitric oxide generation. *Circulation* **2012**, *126*, 325-34.
46. Webb, A.J., et al., Acute blood pressure lowering, vasoprotective, and antiplatelet properties of dietary nitrate via bioconversion to nitrite. *Hypertension* **2008**, *51*, 784-790.
47. Sobko, T., et al., Dietary nitrate in Japanese traditional foods lowers diastolic blood pressure in healthy volunteers. *Nitric Oxide-Biol. Ch.* **2010**, *22*, 136-140.
48. Gonzalez, F.M., et al., Nitrite anion provides potent cytoprotective and antiapoptotic effects as adjunctive therapy to reperfusion for acute myocardial infarction. *Circulation* **2008**, *117*, 2986-2994.
49. Duranski, M.R., et al., Cytoprotective effects of nitrite during in vivo ischemia-reperfusion of the heart and liver. *J. Clin. Invest.* **2005**, *115*, 1232-1240.
50. Webb, A., et al., Reduction of nitrite to nitric oxide during ischemia protects against myocardial ischemia-reperfusion damage. *P. Natl. Acad. Sci. USA* **2004**, *101*, 13683-13688.
51. Carlsson, S., et al., In vitro evaluation of a new treatment for urinary tract infections caused by nitrate-reducing bacteria. *Antimicrob. Agents Ch.* **2003**, *47*, 3713-3718.
52. Dykhuizen, R.S., et al., Helicobacter pylori is killed by nitrite under acidic conditions*. Gut* **1998**, *42*, 334-337.

53. Bryan, N.S., et al., Dietary nitrite supplementation protects against myocardial ischemia-reperfusion injury. *Proc. Natl. Acad. Sci. USA* **2007**, *104*, 19144-19149.
54. Fan, A.M. and V.E. Steinberg, Health implications of nitrate and nitrite in drinking water: An update on methemoglobinemia occurrence and reproductive and developmental toxicity. *Regul. Toxicol. Pharm.* **1996**, *23,* 35-43.
55. Brucker, E.A., et al., High resolution crystal structures of the deoxy, oxy, and aquomet forms of cobalt myoglobin. *J. Biol. Chem.* **1996**, *271*, 25419-22.
56. Gasser, G., I. Ott, and N. Metzler-Nolte, Organometallic anticancer compounds. *J. Med. Chem.* **2011**, *54*, 3-25.
57. Patra, M., G. Gasser, and N. Metzler-Nolte, Small organometallic compounds as antibacterial agents. *Dalton T.* **2012**, *41*, 6350-6358.
58. Taillefer, R., et al., Comparative diagnostic accuracy of Tl-201 and Tc-99m sestamibi SPECT imaging (perfusion and EGG-gated SPECT) in detecting coronary artery disease in women. *J. Am. Coll. Cardiol.* **1997**, *29*, 69-77.
59. Coogan, M.P., P.J. Dyson, and M. Bochmann, Introduction to the Organometallics in Biology and Medicine Issue. *Organometallics* **2012**, *31*, 5671-5672.
60. Sigel, A., H. Sigel, and R.K.O. Sigel, Metal-carbon bonds in enzymes and cofactors. Metal ions in life sciences. **2009**, Cambridge, UK: RSC Pub. xxvii, 510.
61. Setsune, J.I. and D. Dolphin, Organometallic Aspects of Cytochrome-P-450 Metabolism. *Can. J. Chem.* **1987**, *65,* 459-467.
62. Brothers, P.J. and J.P. Collman, The Organometallic Chemistry of Transition-Metal Porphyrin Complexes. *Accounts Chem. Res.* **1986**, *19*, 209-215.
63. Malcamor, L. and A.A. Stark, Mutagenicity and Toxicity of Carcinogenic and Other Hydrazine Derivatives - Correlation between Toxic Potency in Animals and Toxic Potency in Salmonella-Typhimurium Ta1538. *Appl. Environ. Microbiol.* **1982**, *44*, 801-808.
64. Toth, B., Synthetic and Naturally Occurring Hydrazines as Possible Cancer Causative Agents. *Cancer Res.* **1975**, *35*, 3693-3697.
65. Berger, J., Phenylhydrazine Haematotoxicity. *J. Appl. Biomed.* **2007**, *5*, 125-130.
66. Ortiz de Montellano, P.R. and D.E. Kerr, Inactivation of Catalase by Phenylhydrazine - Formation of a Stable Aryl-Iron Heme Complex. *J. Biol. Chem.* **1983**, *258*, 10558-10563.
67. Ortiz de Montellano, P.R. Arylhydrazines as Probes of Hemoprotein Structure and Function. *Biochimie* **1995**, *77*, 581-593.
68. Centers for Disease Control and Prevention, Antibiotic resistance threats in the United States. **2013**.
69. Lessa, F.C., et al., Burden of Clostridium difficile infection in the United States*. N. Engl. J. Med.* **2015**, *372*, 825-34.

70. Poutanen, S.M. and A.E. Simor, Clostridium difficile-associated diarrhea in adults. *CMAJ* **2004**, *171*, 51-8.
71. Voth, D.E. and J.D. Ballard, Clostridium difficile toxins: mechanism of action and role in disease. *Clin. Microbiol. Rev.* **2005**, *18*, 247-63.
72. Leffler, D.A. and J.T. Lamont, Treatment of Clostridium difficile-associated disease. *Gastroenterology* **2009**, *136*, 1899-912.
73. Freeman, J., et al., Surveillance for resistance to metronidazole and vancomycin in genotypically distinct and UK epidemic Clostridium difficile isolates in a large teaching hospital. *J. Antimicrob. Chemother.* **2005**, *56*, 988-9.
74. Pelaez, T., et al., Reassessment of Clostridium difficile susceptibility to metronidazole and vancomycin. *Antimicrob. Agents Ch.* **2002**, *46*, 1647-50.
75. Baines, S.D., et al., Emergence of reduced susceptibility to metronidazole in Clostridium difficile. *J. Antimicrob. Chemoth.* **2008**, *62*, 1046-52.
76. Huang, H., et al., Antimicrobial resistance in Clostridium difficile. *Int. J. Antimicrob. Ag.* **2009**, *34*, 516-22.
77. Reddy, D., J.R. Lancaster, and D.P. Cornforth, Nitrite Inhibition of Clostridium-Botulinum - Electron-Spin Resonance Detection of Iron Nitric-Oxide Complexes. *Science* **1983**, *221*, 769-770.
78. Tompkin, R., L. Christiansen, and A. Shaparis, The effect of iron on botulinal inhibition in perishable canned cured meat. *Int. J. Food Sci. Tech.* **1978**, *13,* 521-527.
79. Payne, M.J., et al., Electron-Paramagnetic Resonance Spectroscopic Investigation of the Inhibition of the Phosphoroclastic System of Clostridium-Sporogenes by Nitrite. *J. Gen. Microbiol.* **1990**, *136*, 2067-2076.
80. Sobko, T., et al., Gastrointestinal bacteria generate nitric oxide from nitrate and nitrite. *Nitric Oxide-Biol. Ch.* **2005**, *13*, 272-278.
81. Cunningham, R., et al., Acidified nitrite: a host defence against colonization with C. difficile spores? *J. Hosp. Infect.* **2014**, *86*, 155-157.
82. Roldan, M.D., et al., Reduction of polynitroaromatic compounds: the bacterial nitroreductases. *FEMS Microbiol. Rev.* **2008**, *32*, 474-500.
83. Mirzaei, N., et al., The mutation of the rdxA gene in metronidazole-resistant Helicobacter pylori clinical isolates. *Adv. Biomed. Res.* **2014**, *3*, 90.
84. Leitsch, D., et al., A study on Nim expression in Bacteroides fragilis. *Microbiology* **2014**, *160*, 616-622.
85. Lynch, T., et al., Characterization of a stable, metronidazole-resistant Clostridium difficile clinical isolate. *PLoS One* **2013**, *8*, e53757.

Chapter 2 Interactions of sperm whale myoglobin with nitrite and nitric oxide ligands

2.1 Introduction

Nitrite reduction to nitric oxide (NO) is an important component of the global N-cycle, where nitrite reductase (NiR) enzymes are the key metalloenzyme species involved (equation 2-1).

$$NO_2^- + e^- + 2H^+ \longrightarrow NO + H_2O \qquad (2\text{-}1)$$

Although the mammalian heme proteins hemoglobin (Hb) and myoglobin (Mb) are known to stoichiometrically reduce nitrite to NO, it was only during the last decade or so that these Hb [1-4] and Mb-induced [5-7] processes were proposed to be physiologically relevant. Interestingly, prior to our work in this area, all published heme-NO_2 complexes contained *N*-bound nitrite ligands (Fig. 2-1) [8-11].

The heme pockets of the heme-nitrite adducts in Fig. 2-1 are quite diverse. Cytochrome cd_1 NiR (top left) has a heme pocket that supplies two H-bonds to one O-atom of the coordinated nitrite. Sulfite reductase (top right) has a heme pocket that stabilize both nitrite O-atoms using three H-bonds; here, the heme also contains a proximal cysteine. Cytochrome *c* NiR (bottom left) and cytochrome *c* NiR Y218F (bottom right) stabilize bound nitrite using two H-bonds; here, the heme is coordinated by a proximal lysine.

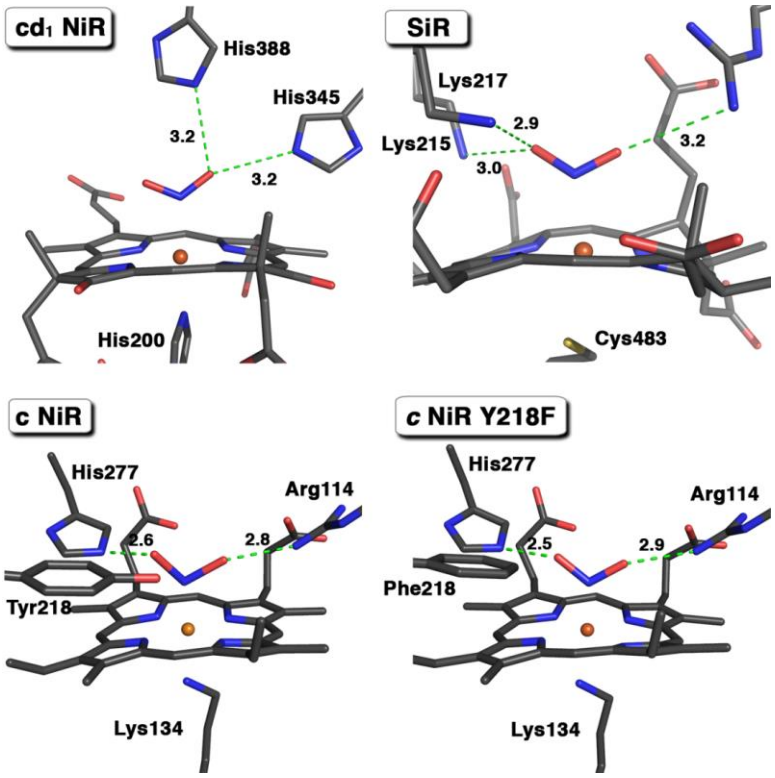

Fig. 2-1. Heme sites of the nitrite complexes of cytochrome cd_1 NiR from *P. pantotrophus* (top left; PDB ID 1AOM), sulfite reductase from *E. coli* (top right; PDB ID 3GEO), cytochrome *c* NiR (bottom left; 2E80) and its Y218F mutant (bottom right; PDB ID 3BNH) from *W. succinogenes*.

Based on the published work, we thought that Mb and Hb would also coordinate nitrite via the *N*-binding mode. Our lab determined the crystal structures of the nitrite adducts of Hb [12] and Mb [13], and showed, surprisingly, that the nitrite coordinated via the *O*-binding mode (Fig. 2-2).

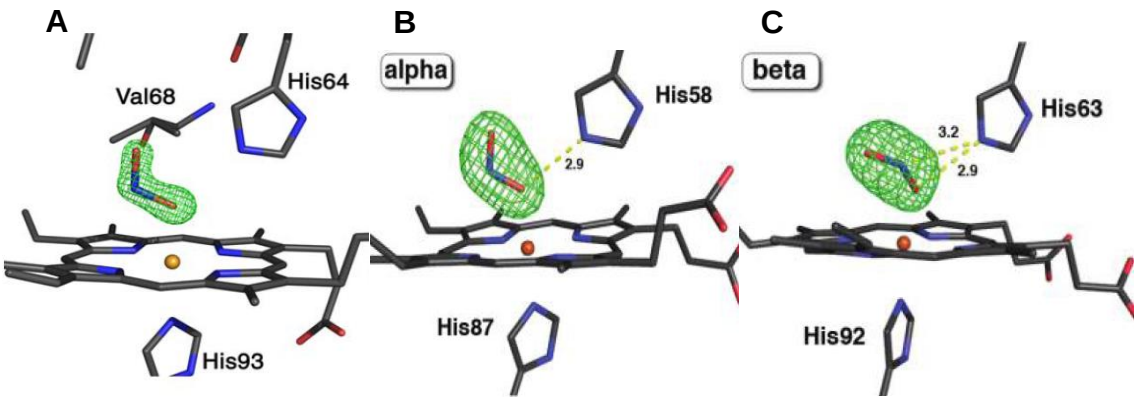

Fig. 2-2. F_o-F_c omit electron density maps (contoured at 3σ) and final models of the heme sites of ferric horse heart Mb (A; PDB ID 2FRF) and human Hb (α subunit in B, β subunit in C; PDB ID 3D7O).

Theoretical calculations on the model (P)Fe(NO)(NO_2) compound showed that the nitrito (O-bound) FeONO isomer was only ~4.3 kcal/mol higher in energy than the nitro (N-bound) $FeNO_2$ isomer [14]. *Why then does the nitrite bind with heme iron in Hb and Mb with this unique O-binding mode?* This question raised our interest in determining what factors influence the NOx ligand binding mode in these heme proteins. It is expected that the reactivity of a ligand is a direct consequence of its binding mode. Therefore, understanding the binding modes of nitrite in Hb/Mb-NO_2 is important to explain the inherent chemical properties of these NOx species.

We proposed earlier that three components in the heme pocket could impose restrictions on the ligand binding mode: (i) the type of metal in the heme, (ii) the distal residues around the ligand, and (iii) the type of macrocycle. In our Mb and Hb systems, nitrite binds to the ferric centers in their proteins. Thus, the O-bound nitrite in ferric Hb/Mb (d^5) may not be in the same

conformation in the reduced ferrous Hb/Mb (d^6) systems. We reported the X-ray structures of the related Mn^{III} (d^4) and Co^{III} (d^6) substituted derivatives (Fig. 2-3A and B) [15]. The *O*-binding modes were exclusively adopted by the nitrite ligands even with these different metal substituted derivatives. In addition, utilizing synchrotron X-ray radiation at high photon flux (3 X 10^{10} protons/s, λ = 1.0 Å, total X-ray dose of ~0.42 MGy), to photoreduce the ferric center to ferrous, still showed the *O*-binding mode of nitrite in the reduced $Mb^{II}ONO$ (d^6) derivative (Fig. 2-3C) [16].

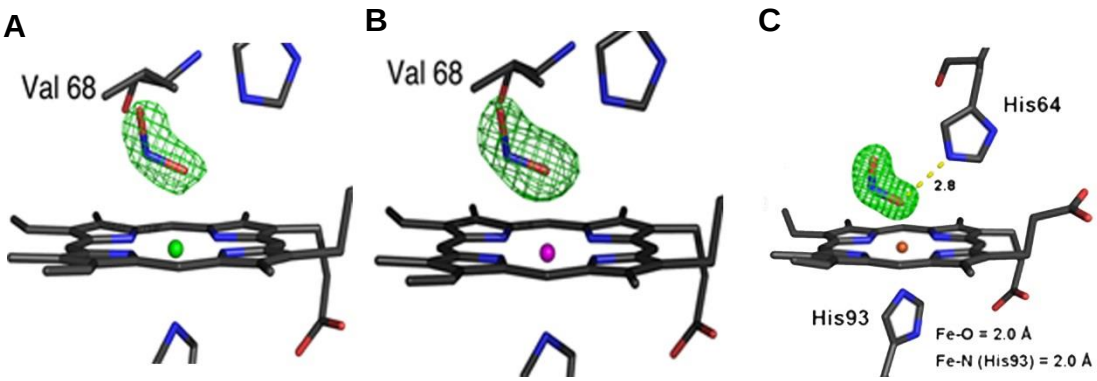

Fig. 2-3. F_o-F_c omit electron density maps and final models of the heme sites of Mn^{III}-substituted Mb (A; contoured at 3σ; PDB ID 2O5O), Co^{III}-substituted Mb (B; contoured at 3σ; PDB ID 2O5S), and ferrous Mb^{II}(ONO) product obtained after exposure of the ferric precursor to high intensity X-ray radiation (C; contoured at 5σ; PDB ID 3LR9).

As noted above, the distal residues may, in principle, also affect the binding mode of nitrite ligands. Most likely, His64 plays an important role in the ligand *O*-binding mode since there is a H-bond between the Nε(H64) atom and the O1(NO_2) atom. A mutant H64V-nitrite derivative was prepared and its structure solved (Fig. 2-4A) [14]. It was exciting to see that the nitrite sits in the

pocket with the (now) *N*-binding mode but with a very weak Fe-NO_2 interaction (~2.6 Å). A double mutant H64V/V67R, replacing the H-bond from His64 by one from Arg67 in the hydrophilic side of heme, recruits the nitrite ligand and adopting an *O*-binding mode again (Fig. 2-4B) [14]. These results strongly support that the H-bond from His64 does play a significant role in the nitrite binding mode, at least in horse heart Mb.

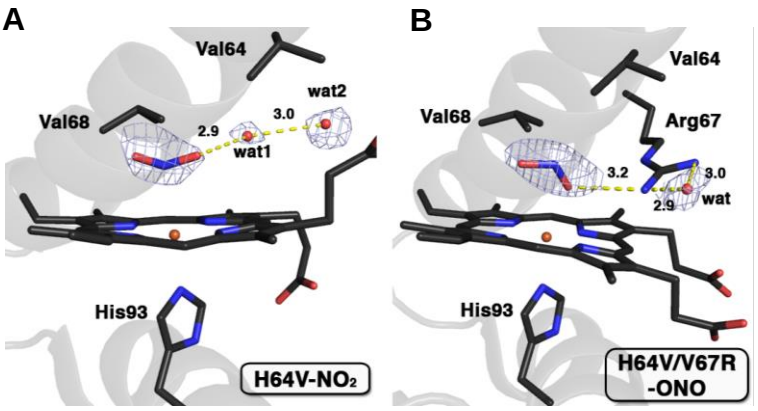

Fig. 2-4. F_o-F_c omit electron density maps (contoured at 3σ) and final models of the heme sites of the N-bound nitrite adduct of the ferric Mb H64V (A; PDB ID 3HEP) and the O-bound nitrite adduct of the ferric Mb H64V/V67R (B; PDB ID 3HEO).

Our lab then proceeded to determine the structures of a heme-reconstituted Mb-nitrite, but with heme replaced by a chlorin (FeMPPa, MPPa = pyropheophorbide-*a* methyl ester) (see two structures below) [17].

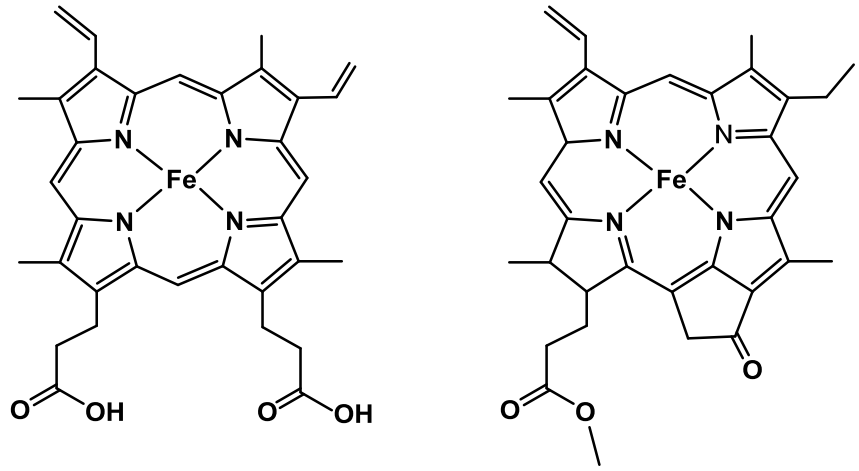

Heme (FePPIX) **Chlorin (FeMPPa)**

A crystal structure of the product obtained from the insertion of the preformed (MPPa)Fe-nitrite into a apoMb displayed a *N*-binding mode (Fig. 2-5A). In contrast, an alternate structure, obtained from addition of nitrite to the reconstituted MbChl(H_2O), was shown to contain the nitrite *O*-binding mode (Fig. 2-5B). Our results demonstrated that both *N*-binding and *O*-binding of nitrite are possible when the macrocycle heme was replaced by a chlorin macrocycle.

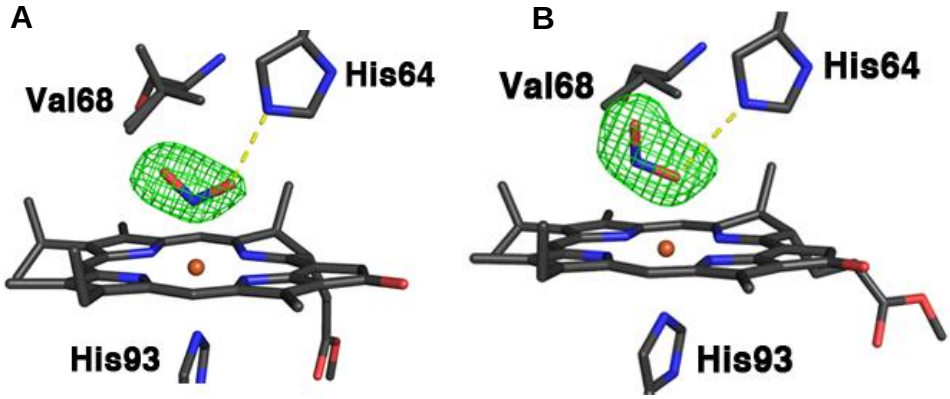

Fig. 2-5. F_o-F_c omit electron density maps (contoured at 3σ) and final models of the heme sites of the N-bound nitrite adduct of the MbChl(NO_2) (A; PDB ID 3V2Z) and the O-bound nitrite adduct of the MbChl(ONO) (B; PDB ID 3V2V).

Based on our lab's result, we arrived at the tentative conclusion that Mb prefers the *O*-binding mode with nitrite. Also, we concluded that His64 plays an important role in the ligand binding mode by donating a H-bond to the nitrite.

The goals of my research in this area were to (i) determine if the nitrite binding modes were species-dependent (e.g., hh Mb vs sw Mb), (ii) to introduce additional H-bonding modifications in the Mb distal pocket and examine their effects on nitrite binding, and (iii) to determine the crystal structures and preferred orientations of the NO products from the nitrite reduction reactions.

Three mutants were designed. In the H64A mutant, the non-H-bonding Ala64 replaces the His64. The H64Q mutant provides a possible hydrogen bond by Gln64. The double mutant V68A/I107Y creates more space in the pocket by replacing Val68 with Ala68, and contributes an additional hydrogen bond from Tyr107 (see the diagram below).

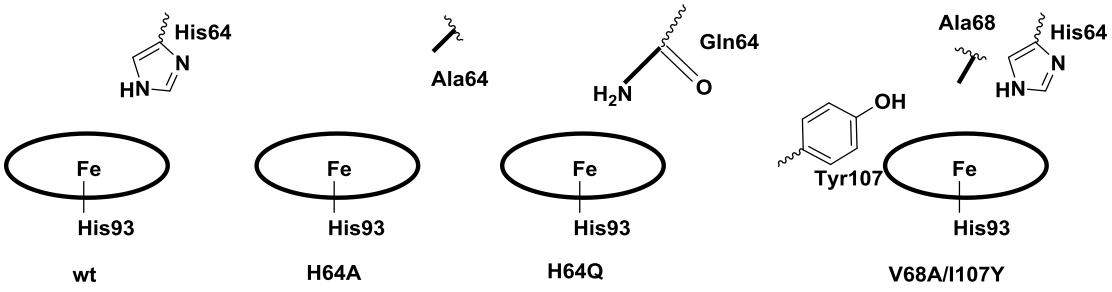

2.2 Materials and methods

2.2.1 Cloning

The plasmid (pET-28a-wt) containing the gene for recombinant wild-type sperm whale myoglobin (wt sw Mb) was kindly provided by Prof. Mario Rivera at the University of Kansas. The wt recombinant protein from this plasmid has two differences in the sequence compared with native sperm whale myoglobin: a Met residue added to the N-terminus as a result of expression by *E. coli*, as well as a mutation made at Asp122 to Asn122 due to an error in the former's sequence determination [18].

Mutagenesis was performed using the Quick-Change method (Stratagene). The steps included (i) PCR with designed primers of mutants depending on the wt sw Mb plasmid; (ii) purification of PCR products; (iii) digestion of templates with the Dpn1 enzyme; (iv) transformation of the products into DH5α (*E. coli*) competent cells; (v) purification of new plasmids. The mutants were confirmed by sequencing. For the double mutant V68A/I107Y, the V68A mutation was performed first, followed by the I107Y mutation.

2.2.2 Expression and purification of the sw Mb proteins

The wt and mutant H64Q proteins were expressed in *E. coli* BL21(DE3) and purified as described by Springer and Sligar [19] with slight modifications. The resuspended cells were sonicated in 50 mM Tris, 1mM EDTA, pH 7.4, and appropriate amounts of DNase, RNase, PMSF, and Pepstatin A. The Mb was obtained pure with a 90% ammonium sulfate (AS) precipitation, after initially

removing other proteins with 60% AS. Dialysis was performed to remove AS using a low salt buffer (20 mM Tris, 1 mM EDTA, 40 mM NaCl, pH 7.4). The sample was subjected to DEAE (Sigma) anion exchange chromatography and eluted using a linear salt gradient from low salt (40 mM NaCl) to high salt (1 M NaCl). A G50 (Sigma) gel filtration with 20 mM Tris, 1 mM EDTA, pH 7.4 was the last purification step to obtain samples pure enough for crystallization.

The purification methods for the H64A and V68A/I107Y proteins were similar to those used for wt and H64Q, except that the DEAE anion exchange column was replaced by a CM-32 cellulose (Whatman) cation exchange column. The CM-32 column was equilibrated with 100 mM potassium phosphate at pH 5.8, and eluted using a linear salt gradient from 0 mM NaCl to 1M NaCl at the same pH value. The proteins produced from this purification procedure contained apo- and heme-bound proteins. In order to obtain homogeneous proteins for the following steps, heme reconstitution was performed for all four proteins between the ion exchange and gel filtration steps. Reconstitution was performed using an excess (15 mM) of heme in 0.1 M NaOH which was added slowly dropwise into the protein solution and stirred overnight at 4 °C. The final purified protein samples were concentrated to ~20 mg/ml for hanging-drop crystallization or 60 mg/ml for crystallization by using the batch method. Protein concentrations were estimated by measuring the absorbance of the heme Soret band at 408 nm using the extinction coefficient of metMb (188 mM^{-1} cm^{-1})

2.2.3 UV-vis and IR spectroscopy of the sw Mb with nitrite and nitric oxide

Aquamet sw Mb proteins were reacted with sodium nitrite directly to form the sw Mb-NO_2 complexes. The sw Mb-NO and mutant derivatives were generated from the reduction of sw Mb-NO_2 by excess dithionite. The reactions were examined by UV-vis spectroscopy and infrared spectroscopy.

UV-vis Spectroscopy

A Hewlett Packard 8453 spectrophotometer was used to obtain the UV-vis spectra of the complexes to determine the reaction times and the stabilities of the complexes. The protein samples in 20 mM Tris, 1 mM EDTA, pH 7.4 were purified as stated above. For all reactions, 10-15 µl of protein (10-20 mg/ml) were added into 2.5 ml 0.1 M phosphate buffer at pH 7.4 in a cuvette to first obtain the *met*Mb spectrum. Next, 5 µl of 1 M sodium nitrite in phosphate buffer were added to obtain the spectra of sw Mb-NO_2. In order to obtain the spectrum of sw Mb-NO, *met*Mb was reduced first by the addition of 5 µl 1 M dithionite, followed by the addition of 5 µl of 1 M sodium dithionite into the cuvette. The spectra were recorded at different time points.

Infrared Spectroscopy

A TENSOR II FTIR spectrometer equipped with BioATR II unit (Bruker) and liquid N_2 cooled MCT detector was used to obtain the NO (ν_{NO}) vibrational frequencies in the Mb derivatives. Phosphate buffer (0.1 M, pH 7.4) was used for all experiments. Each spectrum was obtained at 22 °C. The background spectrum was collected using phosphate buffer. Spectrum 1 was 17 µl of sample containing 10 µl of 0.4-0.7 mM protein solution plus 7 µl of buffer.

Spectrum 2 was 10 µl of the same protein with the addition of 1 µl of 10 M sodium nitrite and after 5 min 6 µl of 1.7 M dithionite was added. The last difference spectrum (spectrum 3) upon the formation of Mb-NO complex was obtained by subtracting spectrum 2 from spectrum 1. Each spectrum condition is listed in Table 2-1.

Table 2-1. Spectra of IR spectroscopy

	Protein solution	NO_2^-/dithionite
Spectrum 1	√	
Spectrum 2	√	√
Spectrum 3		√

2.2.4 Crystallization of the ferric sw Mb and mutant proteins

Crystals of the recombinant myoglobins were grown in AS as described by Phillips *et al*. [20, 21]. For wt, H64Q, and V68A/I107Y, the hanging drop vapor diffusion was used with 2.56-3.20 M AS in the well solution containing 100 mM Tris•HCl, 1 mM EDTA, pH 7.4 or pH 9.0. A 5 µl drop of 20 mg/ml protein was mixed with 5 µl of the well solution on a cover slip. The cover slip was inverted and sealed over the well and allowed to stand at 20 °C. After the drop equilibrated overnight, seeding was performed. The batch method was applied for crystallization of the H64A mutant, in which 10-20 µl of 60 mg/ml protein was mixed with 3.2 M ammonium sulfate in 100 mM Tris•HCl, 1 mM EDTA, pH 9.0 to reach 2.3-2.6 M ammonium sulfate as the final concentration in 10.25x64 mm Monoject^{TM} blood collection tubes (COVIDIEN).

2.2.5 Preparation of the sw Mb-NO_2 and -NO derivatives for X-ray crystallography

Mb-nitrite complexes for X-ray crystallography

The crystal structures of the *met*Mb-H_2O precursors were solved prior to ligand soaking. In addition, the structures of deoxy form without any ligands (i.e., ferrous Mb) were solved using crystals from the reduction of *met* forms using dithionite. Specifically, the appropriately sized *met* form crystals were transferred into a 4 µl droplet (well solution containing 10% glycerol) on a cover slide. The cover slide with the drop was placed in a layer of light mineral oil. Solid dithionite was added into the droplet and after ~10 min the color changed from red to pink signifying the formation of the ferrous deoxy form of Mb. The treated crystals were harvested and stored in liquid nitrogen until used for X-ray diffraction data collection.

The Mb-nitrite complexes were obtained using a similar method as described above. A few solid crystalline particles of sodium nitrite were added into the droplet to react with the Mb crystals for 20-30 min. The treated crystals were harvested using cryo-loops at different time periods and stored in liquid nitrogen.

Mb-NO complex preparation for X-ray crystallography

After soaking the *met* form crystals with nitrite for 20-30 min, excess solid dithionite was added into the droplet to reduce the ferric sw Mb-NO_2 to the ferrous sw Mb-NO derivatives. A clear color change from brown to pink was observed. The treated crystals were harvested as above.

2.2.6 X-ray data collection

The diffraction data was collected at home source using a Rigaku MicroMax 007HF microfocus X-ray generator coupled to a R-AXIS IV++ detector or a PILATUS 200K detector (Table 2-2). The data was collected at 100 K with the Cu Kα radiation (λ = 1.54178 Å) from the generator operated at the working condition 40 kV/30 mA.

Table 2-2. Data collection parameters

	Detector	Detector distance (mm)	Oscillation angles (º)	Oscillation Range (º)	Exposure time (s)
*met*wt-H_2O	PILATUS	35	0.5	116	30
deoxy wt	PILATUS	35	0.5	137	30
*met*wt-NO_2	R-AXIS IV	130	1	90	300
*met*wt-NO	R-AXIS IV	110	1	100	300
*met*H64A-H_2O	R-AXIS IV	130	1	90	300
deoxy H64A	PILATUS	35	0.5	135.5	30
*met*H64A-NO_2	R-AXIS IV	130	0.5	360	120
*met*H64A-NO	PILATUS	35	0.5	114	30
*met*H64Q-H_2O	PILATUS	35	0.5	106	30
deoxy H64Q	PILATUS	35	0.5	95.5	30
*met*H64Q-NO_2	PILATUS	35	0.5	360	180
*met*H64Q-NO	PILATUS	35	0.5	135.5	30
*met*V68A/I107Y-H_2O	PILATUS	35	0.5	360	30
deoxy V68A/I107Y	PILATUS	35	0.5	172	30
*met*V68A/I107Y-NO_2	R-AXIS IV	120	1	100	300
*met*V68A/I107Y-NO	PILATUS	35	0.5	176	30

2.2.7 Data processing, structure solution and refinement

The data were processed using *iMOSFLM* [22] or *HKL3000* [23]. The output *mtz* files from *iMOSFLM* were scaled by Aimless [24]. If *HKL3000* was used, the *sca* output file were transformed into MTZ files by *Scalepack2mtz* as implemented in the CCP4 program suite [25].

Initial phases were obtained by molecular replacement using *PHASER* (CCP4) [26]. The starting model used was wt sw Mb (*met*Mb-H_2O) at 1.5 Å resolution (PDB accessioncode 2MBW) with the heme, sulfates, and water molecules removed from the structure. Refinements were performed using either *Refmac5* (CCP4) or *Phenix.refine* (PHENIX) [27, 28]. Models were rebuilt using *COOT* [29]. The *MolProbity* server was used for structure validation [30]. The details are described below for each of the structures.

The figures of the final models for each structure were generated using *Pymol* [31]. $2F_o$-F_c electron density maps were initially calculated by Fast Fourier Transform (*FFT*) in the CCP4 software package [32]. The resulting *map* files were converted to CCP4 format files and displayed in *Pymol*. F_o-F_c electron density maps were generated as follows: (i) a new PDB file in which ligands were removed from the heme pocket was initially refined for 5 cycles in *Refmac5*; (ii) the new *mtz* file that was generated from the first step was input into *FFT* to generate the *map* that was then displayed in *Pymol*. This procedure was followed for the following structures except when stated otherwise.

wt Mb-H_2O

Ten initial cycles of restrained refinement were run with *Refmac*, and the *R* factor decreased from 0.363 to 0.226. Ligands and water were added to the model depending on the F_o-F_c electron density map in the subsequent refinement cycles. Three sulfate anions were added to the model. The N-terminal Met residue and the residue Gly153 in C-terminus were omitted due to

the lack of electron density. The final *R* factor and R_{free} are 0.144 and 0.193, respectively.

wt Mb deoxy form

Ten initial cycles of restrained refinement were run with *Refmac*, and the *R* factor decreased from 0.380 to 0.271. Ligands and water were added to the model depending on the F_o-F_c electron density map in the subsequent refinement cycles. Two sulfate anions were added to the model. Two conformations for each of the sidechains of Leu115, Asn132 and Tyr151 were modeled with 50% occupancy each. The N-terminal Met residue and the C-terminal residue Gly153 were omitted due to the lack of electron density. The final *R* factor and R_{free} are 0.149 and 0.201, respectively.

wt Mb-NO_2

Ten initial cycles of restrained refinement were run with *Refmac*, and the *R* factor decreased from 0.470 to 0.318. Ligands and water were added to the model depending on the F_o-F_c electron density map in the subsequent refinement cycles. Three sulfate anions, seven nitrite anions and one glycerol were added to the model. Two conformations for each of the sidechains of Lys133 and Lys145 were modeled with 50% occupancy each. The final *R* factor and R_{free} are 0.148 and 0.187, respectively.

wt Mb-NO

Ten initial cycles of restrained refinement were run with *Refmac*, and the *R* factor decreased from 0.444 to 0.307. Ligands and water were added to the model depending on the F_o-F_c electron density map in the subsequent

refinement cycles. One sulfate anion, one nitrite anion, one nitric oxide and one glycerol molecule were added to the model. The C-terminal residues Gln152 and Gly153 were omitted due to the lack of electron density. The final *R* factor and R_{free} are 0.138 and 0.191, respectively.

Mb H64A-H_2O

Ten initial cycles of restrained refinement were run with *Refmac*, and the *R* factor decreased from 0.373 to 0.276. Ligands and water were added to the model depending on the F_o-F_c electron density map in the subsequent refinement cycles. Six sulfate anions and six glycerol molecules were added to the model. Two conformations for each of the sidechains of Lys87, Lys133, and Glu136 were modeled with 50% occupancy each. The N-terminal Met residue was omitted due to the lack of electron density. The final *R* factor and R_{free} are 0.138 and 0.167, respectively.

Mb H64A deoxy form

Ten initial cycles of restrained refinement were run with *Refmac*, and the *R* factor decreased from 0.372 to 0.255. Ligands and water were added to the model depending on the F_o-F_c electron density map in the subsequent refinement cycles. Six sulfate anions and one glycerol molecule were added to the model. Two conformations for each of the sidechains of Leu115, Asn132 and Tyr151 were modeled with 50% occupancy each. The N-terminal Met residue was omitted due to the lack of electron density. The final *R* factor and R_{free} are 0.148 and 0.171, respectively.

Mb H64A-NO_2

Ten initial cycles of restrained refinement were run with *Refmac*, and the *R* factor decreased from 0.347 to 0.255. Ligands and water were added to the model depending on the F_o-F_c electron density map in the subsequent refinement cycles. Three sulfate anions, eight nitrite anions and one glycerol molecule were added to the model. Two conformations for each of the sidechains of Asn122 were modeled with 50% occupancy each. The N-terminal Met residue was omitted due to the lack of electron density. The final *R* factor and R_{free} are 0.148 and 0.187, respectively.

Mb H64A-NO

Ten initial cycles of restrained refinement were run with *Refmac*, and the *R* factor decreased from 0.334 to 0.245. Ligands and water were added to the model depending on the F_o-F_c electron density map in the subsequent refinement cycles. Three sulfate anions, seven nitrite anions, one nitric oxide and two glycerol molecule were added to the model. Two conformations for each of the sidechains of His12, Asn122, and Lys133 were modeled with 50% occupancy each. The N-terminal Met residue was omitted due to the lack of electron density. The final *R* factor and R_{free} are 0.149 and 0.186, respectively.

Mb H64Q-H_2O

Ten initial cycles of restrained refinement were run with *Refmac*, and the *R* factor decreased from 0.348 to 0.254. Ligands and water were added to the model depending on the F_o-F_c electron density map in the subsequent refinement cycles. Six sulfate anions and three glycerol molecules were added

to the model. Two conformations for each of the sidechains of Lys133 and Glu136 were modeled with 50% occupancy each. The N-terminal Met residue was omitted due to the lack of electron density. The final *R* factor and R_{free} are 0.139 and 0.168, respectively.

Mb H64Q deoxy form

Ten initial cycles of restrained refinement were run with *Refmac*, and the *R* factor decreased from 0.361 to 0.253. Ligands and water were added to the model depending on the F_o-F_c electron density map in the subsequent refinement cycles. Six sulfate anions and five glycerol molecules were added to the model. Two conformations for each of the sidechains of Lys87 and Lys133 were modeled with 50% occupancy each. The N-terminal Met residue was omitted due to the lack of electron density. The final *R* factor and R_{free} are 0.147 and 0.183, respectively.

Mb H64Q-NO_2

Ten initial cycles of restrained refinement were run with *Refmac*, and the *R* factor decreased from 0.294 to 0.222. Ligands and water were added to the model depending on the F_o-F_c electron density map in the subsequent refinement cycles. Two sulfate anions, ten nitrite anions and two glycerol molecules were added to the model. Two conformations for each of the sidechains of Lys16, Val68 and Asn122 were modeled with 50% occupancy each. The N-terminal Met residue was omitted due to the lack of electron density. The final *R* factor and R_{free} are 0.160 and 0.201, respectively.

Mb H64Q-NO

Ten initial cycles of restrained refinement were run with *Refmac*, and the *R* factor decreased from 0.317 to 0.240. Ligands and water were added to the model depending on the F_o-F_c electron density map in the subsequent refinement cycles. Three sulfate anions, seven nitrite anions, one nitric oxide and three glycerol molecules were added to the model. Two conformations for each of the sidechains of Asn122 were modeled with 50% occupancy each. The N-terminal Met residue was omitted due to the lack of electron density. The final *R* factor and R_{free} are 0.153 and 0.193, respectively.

Mb V68A/I107Y-H_2O

Ten initial cycles of restrained refinement were run with *Refmac*, and the *R* factor decreased from 0.371 to 0.240. Ligands and water were added to the model depending on the F_o-F_c electron density map in the subsequent refinement cycles. Three sulfate anions and one glycerol molecule were added to the model. The C-terminal residues Gln152 and Gly153 were omitted due to the lack of electron density. The final *R* factor and R_{free} are 0.160 and 0.199, respectively.

Mb V68A/I107Y deoxy form

Ten initial cycles of restrained refinement were run with *Refmac*, and the *R* factor decreased from 0.384 to 0.244. Ligands and water were added to the model depending on the F_o-F_c electron density map in the subsequent refinement cycles. Two sulfate anions and two glycerol molecules were added to the model. The N-terminal Met residue and the C-terminal residue Gln152

and Gly153 were omitted due to the lack of electron density. The final *R* factor and R_{free} are 0.186 and 0.250, respectively.

Mb V68A/I107Y-NO_2

Ten initial cycles of restrained refinement were run with *Refmac*, and the *R* factor decreased from 0.455 to 0.276. Ligands and water were added to the model depending on the F_o-F_c electron density map in the subsequent refinement cycles. One sulfate anion and two nitrite anions were added to the model. The N-terminal Met residue and the C-terminal residues Gln152 and Gly153 were omitted due to the lack of electron density. The final *R* factor and R_{free} are 0.175 and 0.247, respectively.

Mb V68A/I107Y-NO

Ten initial cycles of restrained refinement were run with *Refmac*, and the *R* factor decreased from 0.433 to 0.282. Ligands and water were added to the model depending on the F_o-F_c electron density map in the subsequent refinement cycles. One sulfate anion, one nitrite anion and one nitric oxide were added to the model. The N-terminal Met residue was omitted due to the lack of electron density. The final *R* factor and R_{free} are 0.157 and 0.205, respectively.

2.3 Results

2.3.1 Expression and purification of wt and mutant sw Mbs

The four proteins were expressed in *E. coli*. The mutant H64A and H64Q proteins have higher and more stable expression levels (~100 mg/L) compared with those of the wt and the double-mutant V68A/I107Y proteins (~10 mg/L). In order to get purer proteins, the H64A and V68A/I107Y mutants were passed through a CM cation exchange column rather than a DEAE anion exchange column to obtain pure samples.

2.3.2 UV-vis spectroscopy of sw Mb-NO_2 and -NO derivatives

2.3.2.1 The UV-vis characterization of wt sw Mb-NO_2 and -NO derivatives

In a manner similar to that reported for the reaction of ferric sw Mb with nitrite [33, 34], the reaction of wt sw Mb with sodium nitrite caused a slight red-shift at the Soret band from 408 nm to 409 nm (Fig. 2-6A). This red-shift was also observed in the Q region (450-600 nm) with a decrease at the band at 500 nm [33]. The addition of dithionite to *met* wt Mb caused a quick disappearance of the 408 nm band and the 500 nm band, and the appearance of new bands at 433 nm and 556 nm, representing the formation of deoxy wt Mb (Fig. 2-6B and C) [19, 35]. The subsequent addition of nitrite to deoxy Mb resulted in a gradual shift of the Soret band from 433 nm to 421 nm (Fig. 2-6B), with formation of two bands at 549 nm and 582 nm, which agrees with the previously-reported UV-vis data for the wt sw Mb-NO complex in solution [36]. The changes between the maximum absorbance of wt Mb-NO at 421 nm and the isobestic point 457 nm are plotted in the inset in Fig. 2-6B. According to the data obtained, the formation of the Mb-NO complex reached completion after ~6.5 mins.

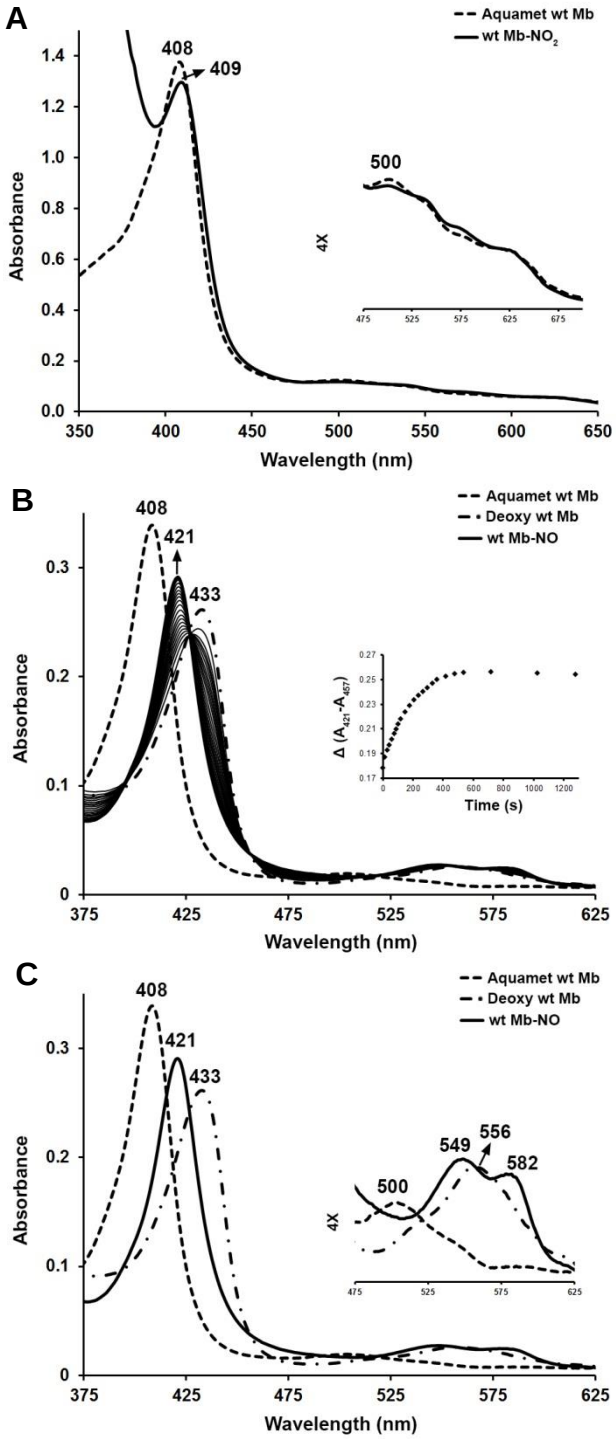

Fig. 2-6. UV-vis spectral monitoring of the reactions of wt sw Mb with nitrite and nitric oxide. A) changes after addition of nitrite; B) changes after addition of dithionite to ferric sw Mb followed by addition of nitrite as well as the plot of ΔAbs(421-457) against time; C) UV-vis spectra of the three forms of wt sw Mb (*aquamet*, deoxy and NO) with the enlarged Q region. Conditions: 0.1 M phosphate buffer, pH 7.4, [protein] = 1.8-7.4 μM, [nitrite] in A) = 40 mM, [dithionite] = 5 mM, [Nitrite] in B) and C) = 4 mM.

2.3.2.2 The UV-vis characterization of wt sw Mb H64A-NO_2 and -NO derivatives

The addition of nitrite to *aquamet* H64A did not result in a significant change of the UV-vis spectrum. The maximum absorbance of H64A-NO_2 is still located at 408 nm in the Soret region, but we do still observe peak profile changes in the Soret and Q regions (Fig. 2-7A). In the inset of Fig. 2-7A, the *aquamet* form of H64A has an absorbance of 505 nm in the Q band which is different from the *aquamet* form of wt which has absorbance at 500 nm. The reaction of H64A and nitrite results in a small decrease of the band at 505 nm (see the solid line of the inset in Fig. 2-7A).

Dithionite reduced the *aquamet* H64A to the deoxy form resulting in a shift of the Soret band to 433 nm (Fig. 2-7B and C), and a Q band at 556 nm (inset in Fig. 2-7C). This reduction by dithionite was followed by the addition of nitrite, resulting in the formation of the NO-complex where NO coordinates with heme iron. The reaction reached completion after ~17 mins (see the inset in Fig. 2-7B). The spectrum of H64A-NO displayed a similar spectrum as the wt-NO derivative, with an absorbance at 421 nm in the Soret region, and 547 nm and 582 nm in the Q region (Fig. 2-7C).

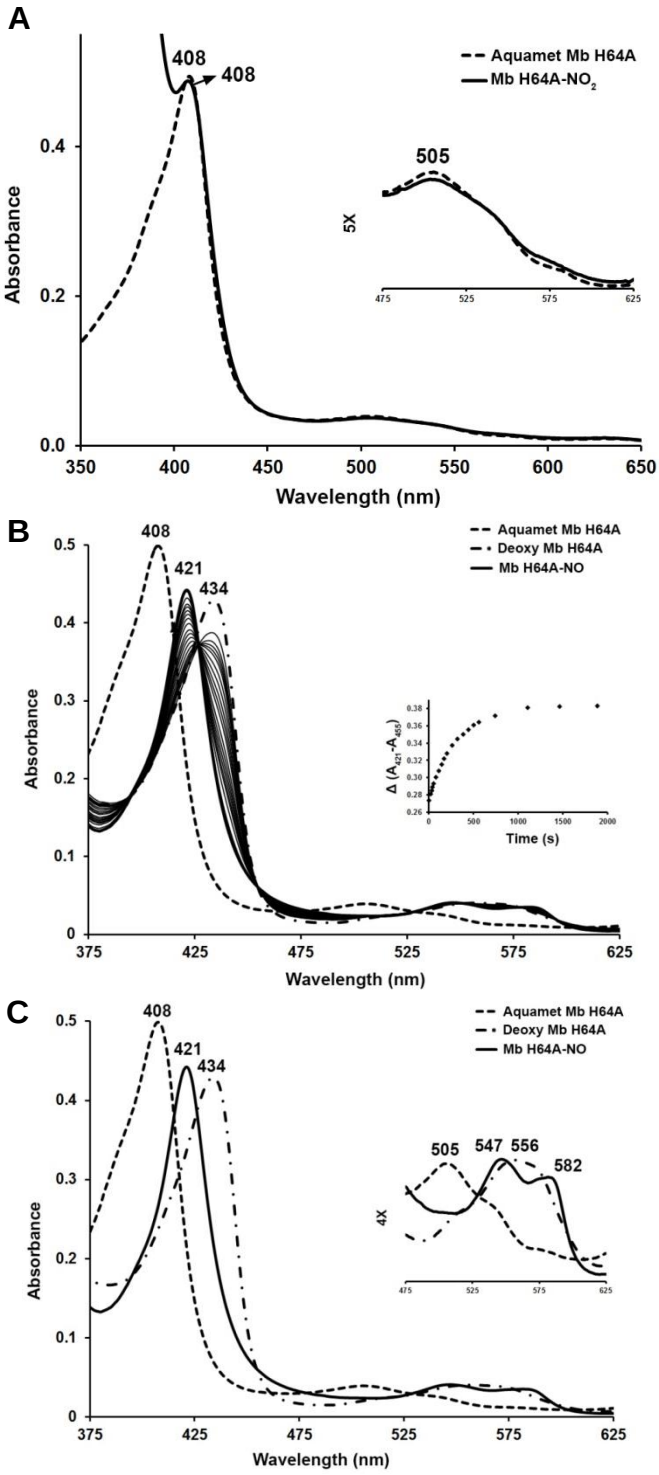

Fig. 2-7. UV-vis spectral monitoring of the reactions of sw Mb H64A with nitrite and nitric oxide. A) changes after addition of nitrite; B) changes after addition of dithionite to ferric sw Mb followed by addition of nitrite as well as the plot of ΔAbs(421-455) against time; C) UV-vis spectra of the three forms of sw Mb H64A (*aquamet*, deoxy and NO) with the enlarged Q region. Conditions: 0.1 M phosphate buffer, pH 7.4, [protein] = 2.7 μM, [nitrite] in A) = 40 mM, [dithionite] = 5 mM, [Nitrite] in B) and C) = 4 mM.

2.3.2.3 The UV-vis characterization of wt sw Mb H64Q-NO_2 and -NO derivatives

We were intrigued that the Soret band of ferric H64Q shifted from 408 nm to 412 nm when the protein was reacted with nitrite, because this shift is much larger than that observed for the other three proteins (Fig. 2-8A). Similar to that seen for H64A, the ferric H64Q protein also has an absorbance at 505 nm in the Q region which flattens upon addition of nitrite (inset in Fig. 2-8A).

There are no large differences for the spectra obtained for the H64Q deoxy and H64Q-NO complex when compared with those obtained for the wt and H64A derivatives. The deoxy form of H64Q (from the reduction of *aquamet* H64Q by dithionite) absorbs at 434 nm in the Soret region (Fig. 2-8B and C), and 558 nm in the Q region (inset in Fig. 2-8C). The reaction of deoxy H64Q with nitrite yields H64Q-NO which absorbs at 421 nm, 548 nm, and 581 nm (Fig. 2-8C). The formation of the H64Q-NO derivative reached completion after ~30 mins (inset in Fig. 2-8B).

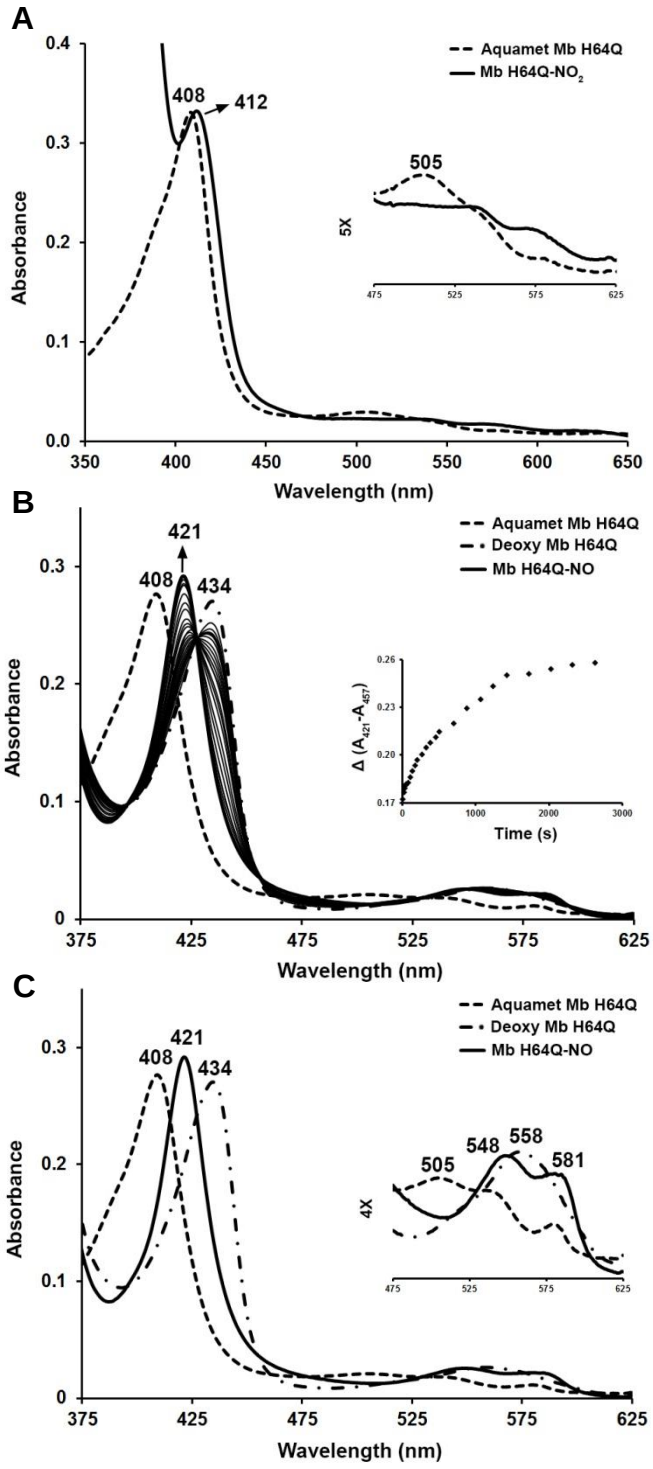

Fig. 2-8. UV-vis spectral monitoring of the reactions of sw Mb H64Q with nitrite and nitric oxide. A) changes after addition of nitrite; B) changes after addition of dithionite to ferric sw Mb followed by addition of nitrite as well as the plot of ΔAbs(421-457) against time; C) UV-vis spectra of the three forms of sw Mb H64Q (*aquamet*, deoxy and NO) with the enlarged Q region. Conditions: 0.1 M phosphate buffer, pH 7.4, [protein] = 1.5 μM, [nitrite] in A) = 40 mM, [dithionite] = 5 mM, [Nitrite] in B) and C) = 4 mM.

2.3.2.4 The UV-vis characterization of wt sw Mb V68A/I107Y-NO_2 and -NO derivatives

A slight red-shift was observed in the UV-vis spectrum after addition of nitrite to the *aquamet* ferric double mutant V68A/I107Y (Fig. 2-9A). The maximum absorbance at 407 nm did not change, but a decrease of the 494 nm in the Q region was observed (inset in Fig. 2-9A). Reduction of ferric V68A/I107Y by dithionite results in a rapid shift of the Soret band from 407 nm to 432 nm which is due to the formation of ferrous deoxy V68A/I107Y (Fig. 2-9B and C). Subsequent addition of nitrite caused the new band to gradually shift from 432 nm to 420 nm, which represents formation of the complex V68A/I107Y-NO (Fig. 2-9B). During the formation of this NO complex, an isosbestic point at 474 nm was observed compared to its position at 457 nm in the wt protein, 455 nm in the H64A protein, and 457 nm in the H64Q protein.

For the spectra of V68A/I107Y-NO shown in Fig. 2-9B and C, the spectrum of deoxy form was obtained from adding 5 mM dithionite to reduce the *met*Mb precursor. Followed by this, nitrite in phosphate buffer was added to reach a final 4 mM concentration, and the spectra were recorded at different time points.

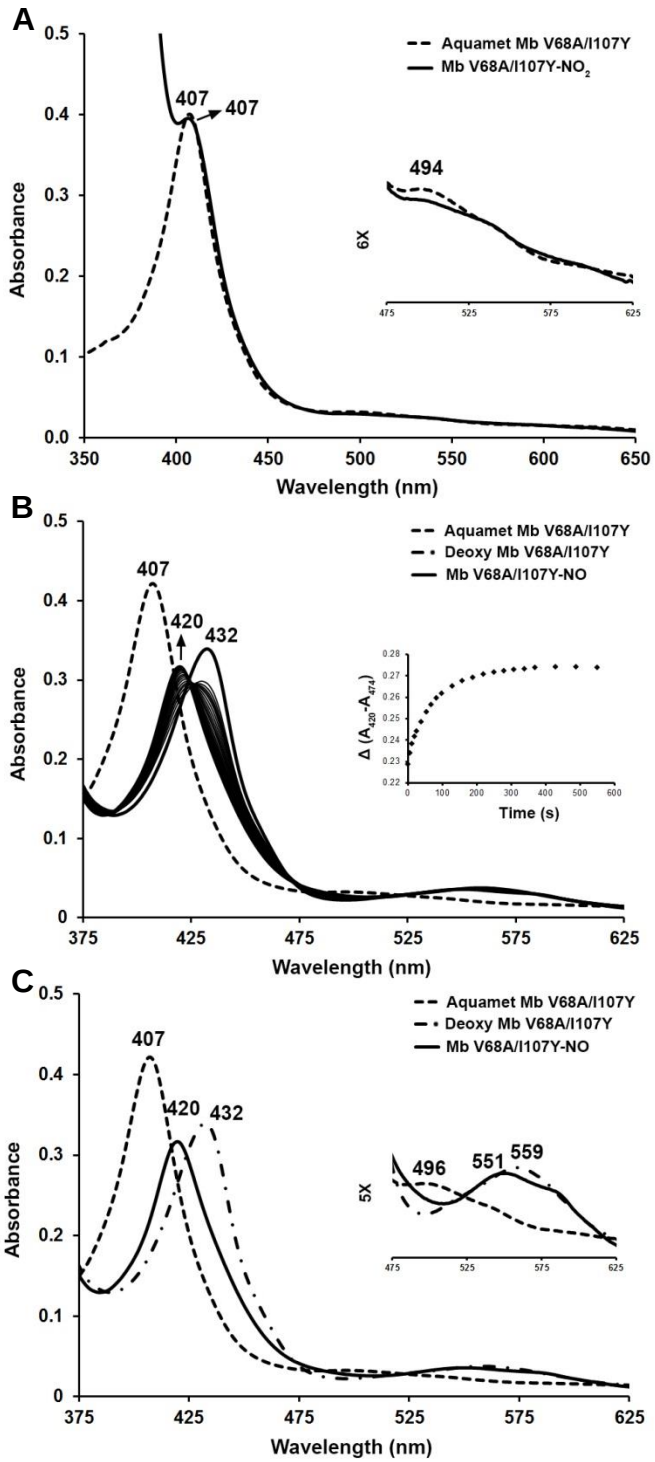

Fig. 2-9. UV-vis spectral monitoring of the reactions of sw Mb V68A/I107Y with nitrite and nitric oxide. A) changes after addition of nitrite; B) changes after addition of dithionite to ferric sw Mb followed by addition of nitrite as well as the plot of ΔAbs(420-474) against time; C) UV-vis spectra of the three forms of sw Mb V68A/I107Y (*aquamet*, deoxy and NO) with the enlarged Q region. Conditions: 0.1 M phosphate buffer, pH 7.4, [protein] = 2.2 μM, [nitrite] in A) = 40 mM, [dithionite] = 5 mM, [Nitrite] in B) and C) = 4 mM.

2.3.3 Crystallization of wt and mutant sw Mbs

The wt and V68A/I107Y Mbs were crystallized from hanging drops containing 2.56 M AS, 100 mM Tris•HCl, 1mM EDTA at pH 7.4. Although crystals of these proteins were also obtained at pH 9.0, the crystal at pH 7.4 had better morphologies. For the H64Q mutant, suitable crystals were obtained from a broad concentration range of AS (2.56 to 3.2 M) either at pH 7.4 or pH 9.0. The fourth protein, namely H64A Mb, was crystallized using the (overnight) batch method. Photos of crystals of the four proteins are shown below (Fig. 2-10).

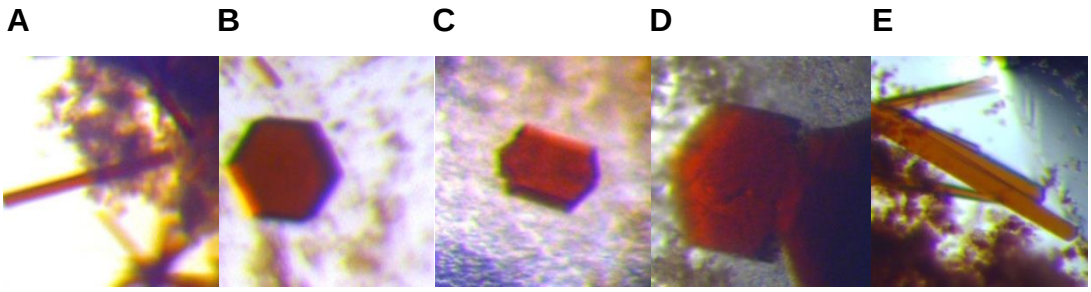

Fig. 2-10. Crystals of the sw Mbs. A) wt sw Mb at pH 7.4; B) sw Mb H64A at pH 9.0; C) sw Mb H64Q at pH 7.4; D) sw Mb H64Q at pH 9.0; E) sw Mb V68A/I107Y at pH 9.0.

2.3.4 The sw Mb-NO_2 derivatives from the nitrite soaking method

Following our group's earlier process at obtaining horse heart Mb-NO_2 derivatives, the ferric sw Mb protein crystals were soaked with nitrite. No cracks in the crystals were observed. The droplets containing the crystals remained clear throughout the entire reaction, and no bubbles (e.g., due to generated NO) or precipitates over the course of the soaking process were observed.

Care was taken to keep the pH of soaking solutions the same as the pH of the pre-formed ferric Mb crystals; namely, pH 7.4 for wt and V68A/I107Y, pH 9.0 for H64A and H64Q.

2.3.5 The sw Mb-NO derivatives from the reactions with sodium nitrite and dithionite

Following the introduction of nitrite to the ferric sw Mbs as described earlier, dithionite was added into the droplet to generate the complexes sw Mb-NO. The crystals changed color from brown to pink during the 10 min reaction of sw Mb-NO_2 with dithionite.

2.3.6 Crystallographic results of sw Mb with nitrite and nitric oxide

The data collection, data processing, and refinement statistics of 16 structures, including the *met* (ferric), deoxy, nitrite, and NO derivatives are shown in Table 2-3. Of these structures, six structures have been previously published or deposited in the PDB database by others: *aquamet* wt (native protein [37], PDB ID 2MBW for the recombinant protein [38]) , deoxy wt, wt-NO (PDB ID 1HJT and 1JDO) [39], *aquamet* H64A (PDB ID 102M) [21], *aquamet* H64Q (PDB ID 2MGH) [18], and deoxy H64Q (2MGG) [18]. The structural comparisons in this chapter will use our own data for these structures. Each of the complexes will be described in detail below.

Table 2-3. X-ray data collection and refinement statistics

	wt-H_2O	wt deoxy form	wt-NO_2	wt-NO	H64A-H_2O	H64A deoxy form	H64A-NO_2	H64A-NO
PDB code								
Data collection[a]								
Space group	*P2₁*	*P2₁*	*P6*	*P2₁*	*P6*	*P6*	*P6*	*P6*
λ (Å)	1.54178	1.54178	1.54178	1.54178	1.54178	1.54178	1.54178	1.54178
Cell dimensions	34.30 30.57 63.77 90.00 105.60 90.00	34.37 30.69 63.81 90.00 105.51 90.00	90.32 90.32 45.25 90.00 90.00 120.00	34.80 29.26 63.95 90.00 105.79 90.00	90.39 90.39 45.27 90.00 90.00 120.00	90.40 90.40 45.27 90.00 90.00 120.00	90.23 90.23 45.22 90.00 90.00 120.00	90.22 90.22 45.31 90.00 90.00 120.00
Resolution range (Å)	30.71 - 1.81	33.12 -1.84	39.11 -1.85	26.42 -1.70	26.09 -1.85	31.99 -1.78	39.14 -1.85	29.59 -1.78
Mean $I/\sigma(I)$	35.4 (17.7)	37.36 (21.85)	46.50 (26.20)	30.10 (8.30)	32.70 (15.10)	65.74 (30.58)	41.70 (19.50)	54.95 (18.28)
No. of reflections								
Observed	23383	26690	98218	27315	99102	141990	392262	119191
Unique	11334 (518)	11131 (509)	18181 (2632)	11177 (581)	18221 (2650)	20332 (954)	18133 (1113)	20265 (966)
Multiplicity	2.1 (1.5)	2.4 (2.0)	5.4 (5.1)	2.4 (2.2)	5.4 (5.2)	7.0 (4.4)	21.6 (21.2)	5.9 (3.6)
Completeness (%)	95.4 (91.0)	97.7 (92.0)	100 (100)	100 (100)	100 (100)	99.5 (91.9)	100 (100)	99.5 (93.5)
R_{merge}[b]	0.029 (0.047)	0.044 (0.072)	0.024 (0.048)	0.030 (0.099)	0.030 (0.084)	0.052 (0.077)	0.072 (0.113)	0.054 (0.091)
Refinement statistics								
No. of protein atoms	1212	1231	1237	1506	1230	1212	1217	1236
R factor (%)[c]	0.144	0.149	0.148	0.138	0.138	0.148	0.148	0.149
R_{free} (%)[d]	0.193	0.201	0.187	0.191	0.167	0.171	0.187	0.186
rmsd bond distances	0.018	0.018	0.027	0.020	0.022	0.024	0.021	0.022
rmsd angles	1.937	1.827	2.330	2.001	2.340	2.390	2.168	2.187
B factor	14.9	15.03	10.97	13.53	12.80	15.22	16.61	16.28
Ramachandran plot (%)[e]								
Residues in most favored	98.00	98.04	98.05	99.33	98.68	98.01	98.01	98.68
Outliers	0.00	0.00	0.00	0.00	0.00	0.00	0.00	0.00

[a] Values in parentheses correspond to the highest resolution shells.

[b] $R_{merge}=\Sigma|I-\langle I\rangle|/\Sigma(I)$, where I is the individual intensity observation and $\langle I\rangle$ is the mean of all measurements of I.

[c] $R=\Sigma||F_o|-|F_c||/\Sigma|F_o|$, where F_o and F_c are the observed and calculated structural factors, respectively.

[d] R_{free} was calculated by using 5% of the randomly selected diffraction data which were excluded from the refinement.

[e] As calculated using *MOLPROBITY*.

Table 2-3. X-ray data collection and refinement statistics (Cont'd)

	H64Q-H_2O	H64Q deoxy form	H64Q-NO_2	H64Q-NO	V68A/I107Y-H_2O	V68A/107Y deoxy form	V68A/I107Y-NO_2	V68A/I107Y-NO
PDB code								
Data collection[a]								
Space group	*P6*	*P6*	*P6*	*P6*	*$P2_1$*	*$P2_1$*	*$P2_1$*	*$P2_1$*
λ (Å)	1.54178	1.54178	1.54178	1.54178	1.54178	1.54178	1.54178	1.54178
Cell dimensions	90.27 90.27 45.26 90.00 90.00 120.00	90.38 90.38 45.22 90.00 90.00 120.00	90.39 90.39 45.24 90.00 90.00 120.00	90.13 90.13 45.25 90.00 90.00 120.00	34.44 30.78 64.04 90.00 105.47 90.00	34.45 30.57 63.81 90.00 105.58 90.00	34.84 29.26 64.06 90.00 105.76 90.00	34.81 29.32 63.92 90.00 105.74 90.00
Resolution range (Å)	29.58 - 1.78	31.97 -1.78	31.98 -1.81	31.93-1.78	33.19 -1.78	26.35-1.80	26.58-1.57	26.53-1.79
Mean $I/\sigma(I)$	61.75 (33.63)	54.25 (22.78)	108.34 (52.62)	68.24 (25.39)	68.34 (33.31)	46.65 (20.74)	14.70 (5.80)	49.27 (29.75)
No. of reflections								
Observed	108186	99766	326132	140393	75872	35492	23849	35049
Unique	20137 (925)	20226 (891)	19390 (932)	20200 (903)	12651 (564)	12004 (548)	10695 (1618)	11655 (570)
Multiplicity	5.4 (3.6)	4.9 (3.3)	16.8 (12.6)	7.0 (4.3)	6.0 (3.6)	3.0 (2.1)	2.2 (2.0)	3.0 (2.0)
Completeness (%)	98.8 (89.0)	99.1 (86.8)	99.9 (100)	99.3 (86.9)	99.5 (92.2)	99.0 (94.3)	87.4 (91.7)	97.0 (91.9)
R_{merge}[b]	0.043 (0.052)	0.054 (0.080)	0.068 (0.116)	0.054 (0.084)	0.051 (0.067)	0.046 (0.070)	0.032 (0.123)	0.027 (0.042)
Refinement statistics	1228	1228	1230	1221	1213	1214	1205	1218
No. of protein atoms	0.139	0.147	0.160	0.153	0.160	0.186	0.175	0.157
R factor (%)[c]	0.168	0.183	0.201	0.193	0.199	0.250	0.247	0.205
R_{free} (%)[d]	0.026	0.022	0.021	0.023	0.018	0.018	0.020	0.019
rmsd bond distances	2.579	2.444	2.135	2.443	1.907	1.875	2.032	1.999
rmsd angles	15.59	16.62	22.99	18.93	20.97	23.63	15.11	14.84
B factor								
Ramachandran plot (%)[e]								
Residues in most favored	98.04	98.04	97.40	97.37	98.00	98.00	98.66	98.01
Outliers	0.00	0.00	0.00	0.00	0.00	0.00	0.00	0.00

[a] Values in parentheses correspond to the highest resolution shells.

[b] $R_{merge}=\Sigma|I-\langle I\rangle|/\Sigma(I)$, where I is the individual intensity observation and $\langle I\rangle$ is the mean of all measurements of I.

[c] $R=\Sigma||F_o|-|F_c||/\Sigma|F_o|$, where F_o and F_c are the observed and calculated structural factors, respectively.

[d] R_{free} was calculated by using 5% of the randomly selected diffraction data which were excluded from the refinement.

[e] As calculated using *MOLPROBITY*.

2.3.6.1 The structural characterization of wt sw Mb with nitrite and nitric oxide

X-ray diffraction data for the wt sw Mb-NO_2 was collected at the OU MCL, and the structure was solved to 1.85 Å resolution. Nitrite was soaked into crystals of the *met* form of wt Mb as described in the methods section. As shown in Fig. 2-11A, C and E, the nitrite ligand is coordinated to the Fe atom of heme in the distal pocket, and interacts with heme iron via the *O*-binding mode as observed by us previously in mammalian Mb or Hb [12-14]. The nitrite sits vertically in the distal pocket with a distance of 2.0 Å between the heme iron atom and oxygen atom (O1) of nitrite (named as Fe-ONO in Table 2-4). The *trans* axial distance between Fe and N_ε of His93 is also 2.0 Å (named as Fe-N_ε (His93) in Table 2-4). The O1 atom is aligned along Fe-N_ε(His93) bond with an angle of 171°. The bent nitrite linkage is oriented towards the hydrophobic side of the heme pocket with an angle of 107° (∠O1-N-O2 in Table 2-4, O2 is the terminal oxygen atom). The nitrite ∠N-O1-Fe angle is 105°.

The nitrite ligand was modeled in the distal pocket with 100% occupancy. The His64 residue helps to stabilize the nitrite ligand in the distal pocket via a H-bonding interaction. The distance between the N_ε atom of His64 and the nitrite O2 atom (not bound to Fe) of nitrite is 3.2 Å, whereas the distance between the N_ε atom and O1 atom (bound to Fe) is 2.8 Å (Fig. 2-11A). The nitrite ligand is in close van der Waals contact with Val68: both nitrite N and O1 atoms have distances of ~3.3 Å to $C_{\gamma 2}$ of Val68, but O2 is slightly farther away

from $C_{\gamma 2}$ with a distance of 3.4 Å. Selected structural data are listed in Table 2-4.

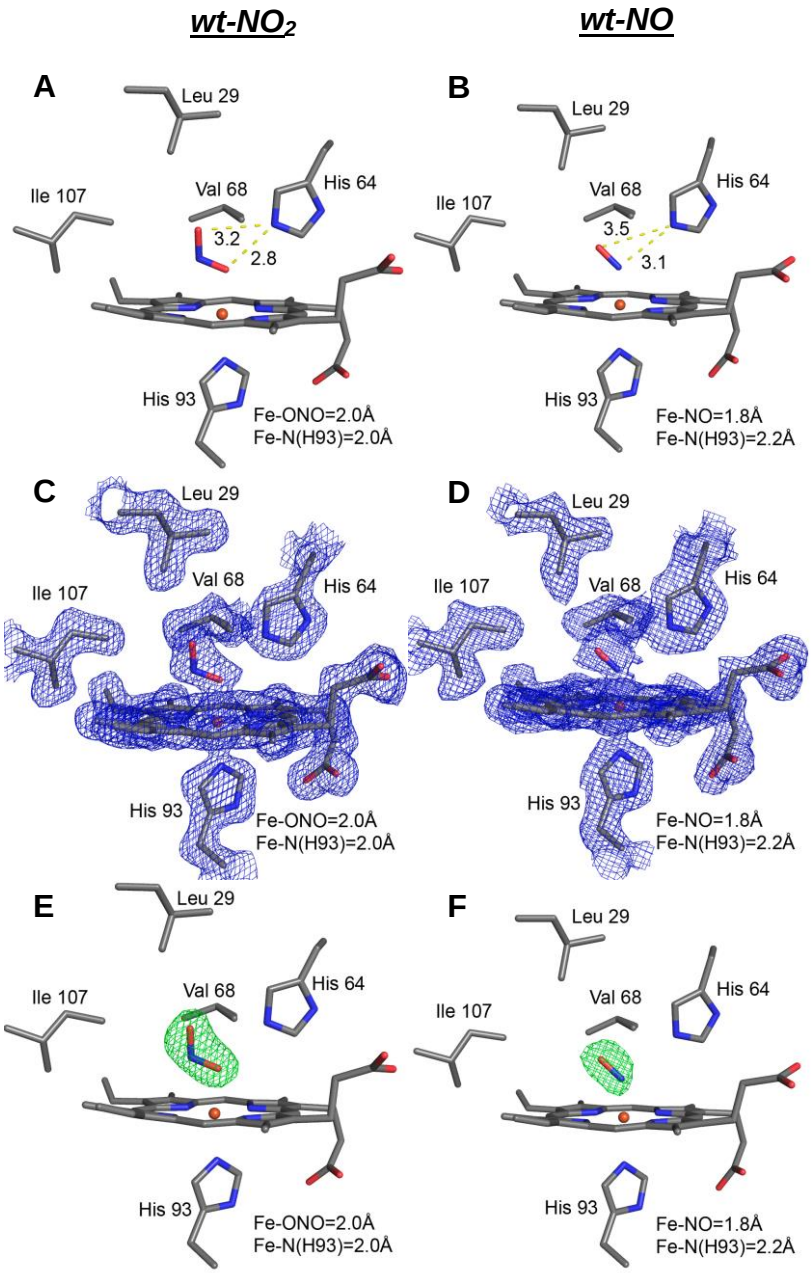

Fig. 2-11. Crystal structures of wt sw Mb-NO_2 and -NO. A-B) final models of the heme pockets of wt-NO_2 and -NO; C-D) $2F_o$-F_c electron density maps (contoured at 1 σ) of the heme pockets in wt-NO_2 and -NO; E-F) the F_o-F_c omit electron density maps showing the nitrite (contoured at 3 σ) and NO ligands (contoured at 3 σ) in the complexes.

The wt-NO complex structure was obtained from the nitrite/dithionite method. Specifically, nitrite was soaked into the crystals of the *met* form followed by dithionite addition that reduced both nitrite to NO and Fe^{III} to Fe^{II}. As seen in Fig. 2-11B, D and F, the NO coordinates to Fe in a direction towards the hydrophobic side of porphyrin and the interior of the protein. The nitrosyl N-atom is situated along the Fe-N_ε(His93) axis (174°). The N atom of the bound NO is closer to the N_ε of His64 (3.1 Å) than the O atom is (3.5 Å). The NO ligand stays in close van der Waals contact with Val68. The O atom of NO is 3.2 Å away from $C_{\gamma 2}$(Val68), whereas the nitrosyl N atom is 3.3 Å away from $C_{\gamma 2}$(Val68).

2.3.6.2 The structural characterization of sw Mb H64A with nitrite and nitric oxide

Both complexes, H64A-NO_2 and H64A-NO, were crystallized and their structures solved (Fig. 2-12). We previously noted the importance of the His64 residue for directing the *O*-binding mode of nitrite in the distal pocket of Mb [40]. For example, the crystal structure of horse heart Mb H64V-NO_2 displayed a weak *N*-binding mode due to the replacement of the H-bonding His64 residue by valine [14]. Surprisingly, our sperm whale H64A-NO_2 complex has a similar structure as wt-NO_2, where nitrite binds to heme iron with an *O*-binding mode rather than switching to *N*-binding as observed in the horse heart Mb H64V derivative (Fig. 2-12A, C, and E). Further description is provided in the discussion section.

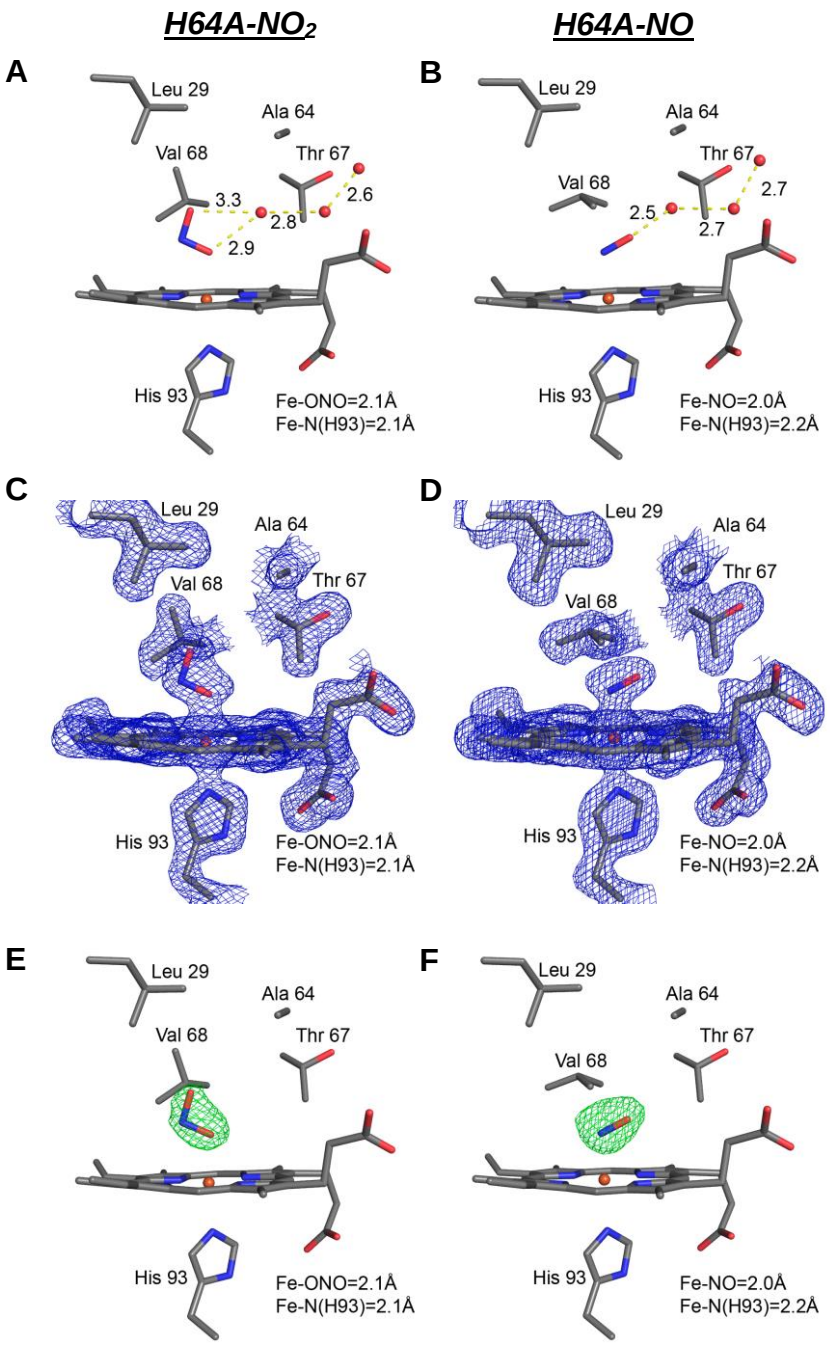

Fig. 2-12. Crystal structures of sw Mb H64A-NO_2 and -NO. A-B) final models of the heme pockets of H64A-NO_2 and -NO; C-D) $2F_o$-F_c electron density maps (contoured at 1 σ) of the heme pockets in H64A-NO_2 and -NO; E-F) the F_o-F_c omit electron density maps showing the nitrite (contoured at 3 σ) and NO ligands (contoured at 3 σ) in the complexes.

Similar to that seen in wt-NO_2, the nitrite ligand in the H64A-nitrite derivative also bends towards the hydrophobic side of the heme, but surprisingly, it is more bent with an angle of 99° (c.f., 107° in wt-NO_2). Other structure data are listed in Table 2-4. The O1 atom of nitrite is almost aligned on the Fe-N_ε(His93) axis with an O1-Fe-N_ε(H93) angle of 174°. Interestingly, since His64 was replaced by Ala, and in order to stabilize the nitrite ligand, the protein recruited water molecules to build a H-bond 'bridge' to stabilize the ligand in the distal pocket (Fig. 2-12A). The distance between the first water (O-atom) molecule, closest to nitrite, and the O1 and O2 atoms of nitrite are 2.9 Å and 3.3 Å, respectively. The nitrite maintain a close van der Waals contact with Phe43 (instead of Val68) with a distance of 3.5 Å between the O2 atom of nitrite and the C_ζ of Phe43, since Val68 has now flipped from the horizontal to a vertical orientation.

The NO ligand in H64A-NO has an orientation that is clearly different from the wt-NO structure, in that it now points to the hydrophilic side of porphyrin rather than the hydrophobic side (Fig. 2-12B, D, and F). The N-atom of NO is on the Fe-N_ε(His93) axis (173°, see Table 2-4). The H64A-NO derivative also recruits three water molecules to build up a H-bond bridge which further stabilizes the NO ligand (Fig. 2-12B). The O atom of NO ligand forms a strong H-bond with the closest water molecule with a distance of 2.5 Å. In contrast to the H64A-NO_2 derivative, the sidechain of Val68 did not flip orientation, thus the NO ligand still keeps a close van der Waals contact with Val68. The N and O atoms of the NO ligand are 3.0 Å and 3.2 Å, respectively, from the $C_{\gamma 2}$ atom of Val68.

Table 2-4. Selected structural parameters for the Mb-NO_2 and –NO derivatives

	Fe-ONO (Å)	Fe- N_ε(H93) (Å)	O1-N (Å)	N-O2 (Å)	∠Fe-O1-N (°)	∠O1-N-O2 (°)	∠O1-Fe-N_ε(H93) (°)	d1* (Å)	d2* (Å)
wt-NO_2	2.0	2.0	1.2	1.3	105	107	171	2.8	3.2
H64A-NO_2	2.1	2.1	1.3	1.3	112	99	174	2.9	3.3
H64Q-NO_2	2.0	2.1	1.3	1.2	123	105	176	2.9	3.3
V68A/I107Y-NO_2	2.0	2.1	1.2	1.4	117	118	173	2.8	3.1
	Fe-NO (Å)	Fe- N_ε(H93) (Å)	N-O (Å)	—	∠Fe-N-O (°)	—	∠N-Fe-N_ε(H93) (°)	d3* (Å)	d4* (Å)
wt-NO	1.8	2.2	1.3	—	138	—	174	3.1	3.5
H64A-NO	2.0	2.2	1.2	—	115	—	173	—	2.5
H64Q-NO	2.0	2.3	1.2	—	122	—	175	—	2.5
V68A/I107Y-NO	2.0	2.1	1.3	—	142	—	179	2.9	3.1

* d1, d2, d3 and d4 are shown in the scheme below.

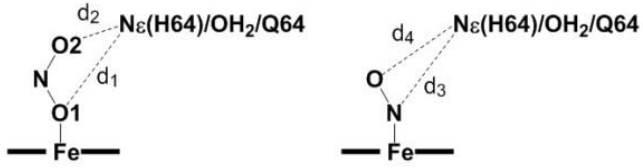

2.3.6.3 The structural characterization of sw Mb H64Q with nitrite and nitric oxide

The nitrite sits in the Mb H64Q distal pocket in a similar conformation as that seen of the above two proteins (Fig. 2-13A, C, and E). The distances between the O1 and O2 atoms of nitrite and the N_ε atom of Gln64 are 2.9 Å and 3.3 Å, respectively, with a H-bond between the nitrite O1 atom and N_ε(Gln64). In general, the nitrite remains vertical to the heme plane, but forms a wider Fe-O1-N angle of 123° compared with the related angle in the wt (105°) and H64A (112°) proteins (Table 2-4). The O1 atom is almost co-linear with the Fe-N_ε(His93) axis with an angle of 176° (Table 2-4). Two alternative conformations of the sidechain of Val68, horizontal and vertical, were modeled and this disorder is most likely due to the close van der Waals contact with the nitrite ligand.

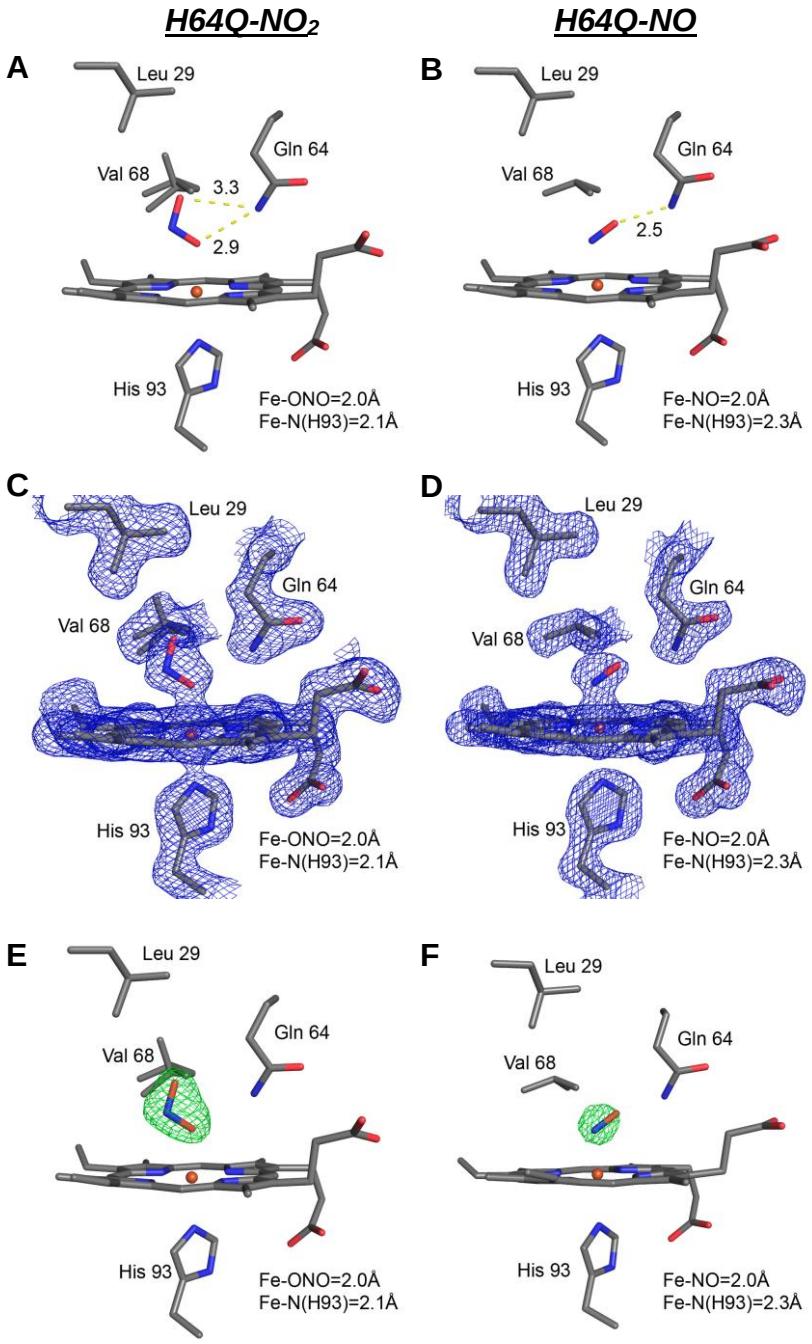

Fig. 2-13. Crystal structures of sw Mb H64Q-NO_2 and -NO. A-B) final models of the heme pockets of H64Q-NO_2 and -NO; C-D) $2F_o$-F_c electron density maps (contoured at 1 σ) of the heme pockets in H64Q-NO_2 and -NO; E-F) the F_o-F_c omit electron density maps showing the nitrite (contoured at 3 σ) and NO ligands (contoured at 3 σ) in the complexes.

In the H64Q-NO derivative, the Gln64 residue plays a similar role as His64 in the wt protein. As expected, just as in the nitrite complex, it participates in a H-bond with the NO ligand. However, Gln64 forms a H-bond with the nitrosyl O atom of NO rather than the N atom, which is unusual in hemeprotein-NO structures. In this H64Q-NO complex, NO points towards the hydrophilic side of the porphyrin rather than the hydrophobic side, probably due to the strong H-bond (2.5 Å) with Gln64 (Fig. 2-13C and D). Other structural data are listed in Table 2-4. The N atom from NO formed an angle of 175° with the Fe-N_{ε}(His93) bond. The NO ligand keeps a close van der Waals contact with Val68, and both atoms of NO (N and O atoms) have equal distances with the the $C_{\gamma 2}$ atom of Val68.

2.3.6.4 The structural characterization of sw Mb V68A/I107Y with NOx

Surprisingly and contrary to our expectation, the mutation of Ile107 to Tyr in the distal pocket did not change the nitrite binding mode; it remained *O*-bound to Fe. The $\angle$O1-N-O2 angle of 118° is wider than those seen in the other three proteins (Table 2-3). The nitrite ligand keeps in close van der Waals contact with the nearby Phe43 and Ala68 residues. The closest atom distances between nitrite and these two residues are all 3.4 Å. It is unlikely that Tyr107 participates in a H-bond with the nitrite ligand since the closest distance (O1 of nitrite and O_{η} of Tyr107) is 3.5 Å. The O1 and O2 atom of nitrite are 2.8 Å and 3.1 Å, respectively, from the N_{ε}(His64) atom.

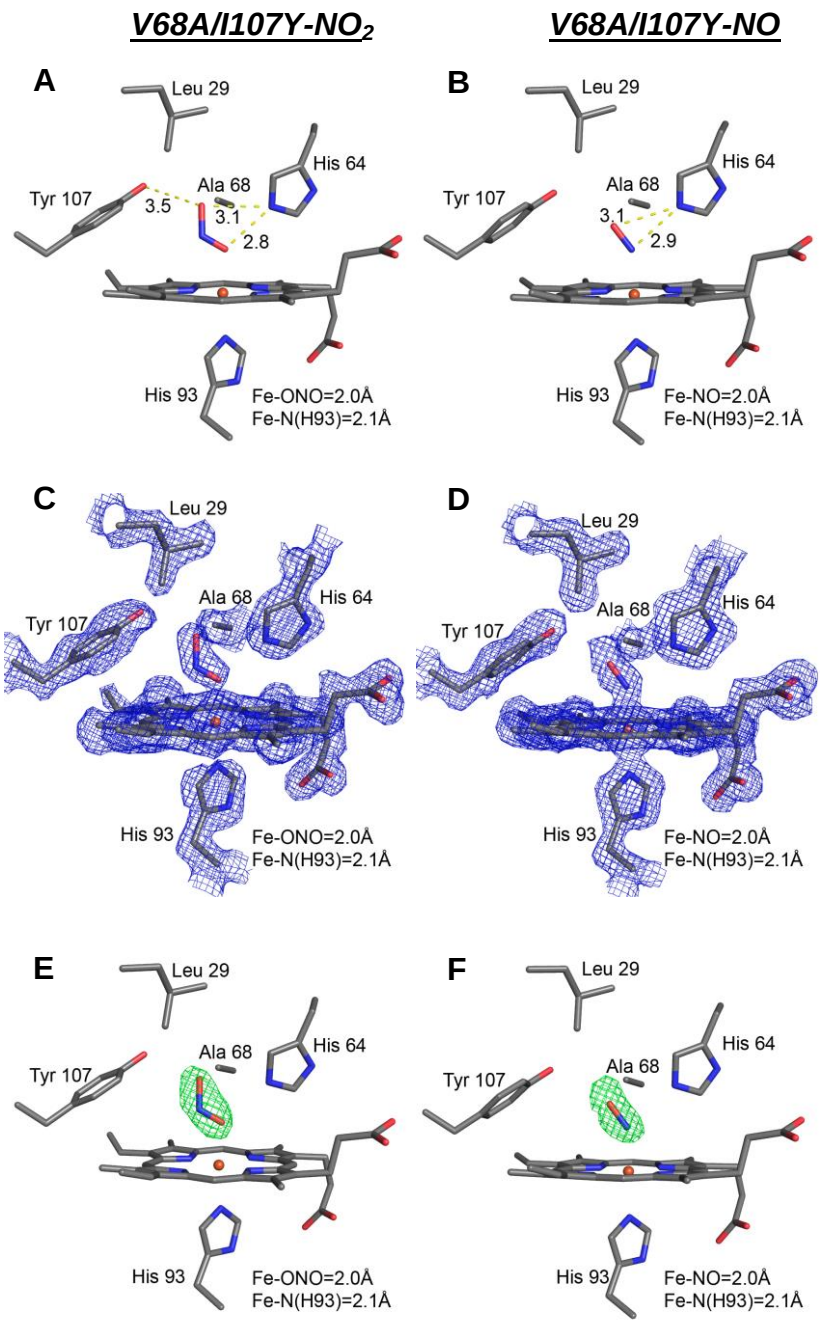

Fig. 2-14. Crystal structures of sw Mb V68A/I107Y-NO_2 and -NO. A-B) final models of the heme pockets of V68A/I107Y-NO_2 and -NO; C-D) $2F_o$-F_c electron density maps (contoured at 1 σ) of the heme pockets in V68A/I107Y-NO_2 and -NO; E-F) the F_o-F_c omit electron density maps showing the nitrite (contoured at 3 σ) and NO ligands (contoured at 3 σ) in the complexes.

The nitrosyl complex of this double mutant V68A/I107Y was also obtained. The resulting FeNO moiety is more like that of the wt, with NO pointing towards the hydrophobic side of the porphyrin. The distance between the O atom of NO and the N_{ε}(His64) atom is 2.9 Å, which is farther than the distance between the N atom of NO and the N_{ε}(His64). Tyr107 is not involved in a H-bond with the NO ligand since the distance between the O atom of NO and the Oη of Tyr107 is too long (4.2 Å). Except for His64, the closest contact with other distal residues is 3.6 Å, namely between the O atom of NO and the C_{β}(Ala68) atom.

2.4 Discussion

2.4.1 The *O*-binding mode of nitrite holds up surprisingly well in sw Mb and its mutants.

The preferred but unusual *O*-binding of nitrite to Mb is more definite than we thought. The *O*-binding mode holds up surprisingly well even in the V68A/I107Y double mutant which was predicted by us to display the *N*-binding mode due to two possible H-bonds at opposite sides of nitrite (compare with Fig. 2-1). The H64A mutant lacking a distal pocket H-bond from His64 holds the nitrite ligand with an *O*-binding mode as well, which is surprisingly different from what we observed previously with hh Mb-NO_2 H64V [14].

Val68 may play an important role in the binding of nitrite and Mb.

When necessary, the sidechain of Val68 can change its conformation to accommodate the nitrite ligand. In most of the complex structures, the nitrite and NO ligands keep in close van der Waals contact with Val68, except for the double mutant V68A/I107Y where the Val68 was mutated to Ala. In the structure of H64A-NO_2, the sidechain of Val68 flipped from a horizontal to a vertical conformation due to the interaction between the nitrite and Val68 (Fig. 2-12A, C, and E). Another example is H64Q-NO_2 in which the sidechain of Val68 was partially pushed from its original horizontal position to a vertical position (Fig. 2-13A, C, and E). The conformational change of Val68 is not observed in the NO complexes, since NO is smaller and has less steric effect than nitrite. Val68 can accordingly adjust its conformation when the nitrite interacts with Mb, and may affect the binding of nitrite to Mb.

Water molecules can replace the distal pocket H-bonds lost in Mb.

The H64A mutant, with no H-bond from the distal pocket residues, recruits three water molecules in the distal pocket to form a "water bridge" which contribute to a "replacement" H-bond bridge with the nitrite ligand (Fig. 2-12A, C, and E). This is probably the reason why the nitrite still keeps *O*-binding mode in the H64A-nitrite derivative. Even with an omitted H-bond from His64, water molecules can remedy the H-bonds lost to stabilize the ligand.

In fact, this "water bridge" also helps to stabilize the coordinated water molecule with heme iron in the *aquamet* H64A, which was also seen in previously published ferric mutant sw Mb H64G-H_2O, but not in the H64V and H64L mutants [18]. The stable coordinated water with iron in *aquamet* H64A-H_2O may also account for the similar absorbance of 408 nm of the Soret band between wt and H64A.

2.4.2 The 64th residue may affect the orientation of the ligand.

There are two different orientations of NO ligands in the four proteins (Fig. 2-15). The NO in the wt and V68A/I107Y derivatives points to the hydrophobic side of porphyrin (red and yellow in Fig. 2-15) which is the dominant conformation in both sw Mb or hh Mb [13, 15, 39, 41], but it switches to the hydrophilic side of porphyrin in sw H64A and sw H64Q (blue and purple in Fig. 2-15). The significant difference is the 64th residue for these two groups of proteins. The wt and V68A/I107Y proteins have a His reside in the 64th position, whereas the H64A and H64Q mutants do not. We thus clearly

observe, for the first time, that the 64th residue affects the *orientation* of the NO ligand, in large part due to the fact that the 64th residue usually keeps in close contact to the NO ligand via H-bond interactions.

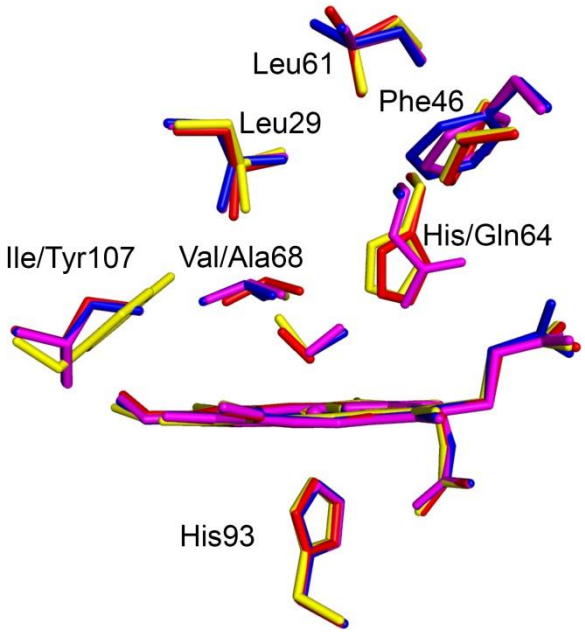

Fig. 2-15. Comparison of the heme pockets from the four Mb-NO complexes: wt-NO (red), H64A-NO (blue), H64Q-NO (purple), and V68A/I107Y-NO (yellow).

This is the first reported observation of the hydrophilic orientation of NO ligand in hemeprotein-NO derivatives. Selected structural data of the nitrosyl his-liganded hemeproteins are listed in Table 2-5. The bound NOs form a broad range of ∠Fe-N-O angles from 112° to 180°, with the Fe-N(O) distances ranging from 1.5-2.1 Å. The significant range of FeNO conformation suggests the influence on the NO ligand by the distal residues through the combination of factors including steric and electrostatic effects [13].

Table 2-5. X-ray structural data for the nitrosylated His-liganded heme proteins[a]

Hemeprotein-NO complexes	PDB	Res (Å)	O.S.[b]	Fe-N(O) (Å)	N-O (Å)	∠Fe-N-O (°)	Fe-(L_{Prox}) (Å)	ref
sw Mb	1HJT	1.7	II	1.89	1.15	112	2.18	[39]
L29F/D122N sw Mb	1JDO	1.9	II	1.86	1.14	127	2.31	[39]
sw Mb wt		1.7	II	1.8	1.3	138	2.2	[c]
H64A		1.78	II	2.0	1.2	115	2.2	
H64Q		1.78	II	2.0	1.2	122	2.3	
V68A/I107Y		1.79	II	2.0	1.3	142	2.1	
hh Mb (MS xafs)			II	1.75	1.12(2)	150(2)	2.05	[42]
			III	1.68(2)	1.13(2)	180(4)	2.04	[42]
hh Mb	1NPF	1.9	II	2.0	1.1	147	2.1	[41]
hh Mb (nitrite/dithionite)	2FRJ	1.3	II	1.9	1.2	144	2.1	[13]
hh Mb (NO gas)	2FRK	1.3	II	2.1	1.2	121	2.1	
Tuna Mb	2NX0	0.95	II	1.7	1.2	134	2.1	[43]
NP1 from *Rhodnius prolixus*	4NP1	2.3	II	2.06	1.34	120	2.10	[44]
			III	2.02	1.32	145	2.0	
NP2 from *Rhodnius prolixus*	1T68	1.45		1.93	1.38	134	2.10	[45]
NP4 from *Rhodnius proxilus*								
WT (5.6)	1KOI	1.08	III	1.7	1.1	155	1.0	[46]
WT (pH 7.4)	1X8N	1.08	II	1.74(2)	1.20(2)	143.8(1.6)	2.06(1)	[47]
WT (pH 5.6)	1X8O	1.01	III	1.69(1)	1.09(1)	159.1(1.1)	1.994(7)	[47]
D129A/L130A	1SXX	1.0	III	1.60(2)	1.35	155(2)	2.05	[48]
T121V	1SY1	1.0	III	1.62(2)	1.29	158(2)	2.03	[48]
D30N	1SY3	1.0	II	1.78(2)	1.38	132(2)	2.06	[48]
D30A	1SXW	1.05	II	1.71(3)	1.35	139(2)	2.09	[48]
WT (pH 5.6)	1YWB	0.9	II	1.7	1.1	141	2.1	[49]
L133V (pH 5.6)	2AT0	1.00		1.7	1.1	153	2.1	[50]
V36A/D129A/L130A	2OFR	1.00		1.7	1.3	136	2.0	[51]
D30N/E32Q/D35N	4GRJ	1.15		1.8 (A)	1.2 (A)	142 (A)	2.1 (A)	[52]
				1.8 (B)	1.2 (B)	138 (B)	2.1 (B)	
NP7 from *Rhodnius prolixus*	4XME	1.29		1.8	1.4	124	2.2	[53]
HO from *N. meningitides*	1P3U	1.75	II	1.58	1.17	147	2.13	[54]
HO-1 from rat	1JO2	1.7	II	2.10	1.14	125	2.17	[55]
Human HO-1								
WT	1OZW	1.55	II	1.64	1.14	138	2.12	[56]
D140A	1OZL	2.59	II	1.49	1.16	148	2.12	[56]
Verdoheme	1TWR	2.10		1.83	1.15	151	2.54	[57]
				1.98	1.16	150	2.37	
G139A/R183E	1XK0	2.18	II	2.0	1.2	142	2.1	[58]
R183E	1XK3	2.08	II	2.2	1.2	155	2.1	[59]
HO-2 from Synechocystis sp. PCC 6803	1WOX	2.10	II	2.1	1.1	126	2.1	[60]
			II	2.1	1.1	119	2.1	
Lupin legHb	1GDL	1.8	II	1.97	1.35	145	2.19	[61]

Table 2-5. X-ray structural data for the nitrosylated His-liganded heme proteins[a] (cont'd)

Hemeprotein-NO complexes	PDB	Res (Å)	O.S.[b]	Fe-N(O) (Å)	N-O (Å)	∠FeNO (°)	Fe-(L_{Prox}) (Å)	ref
Soybean legHb (MS XAFS)			II	1.77	1.12	147	1.98	[42]
			III	1.68	1.12	173	1.89	[42]
FixL from *B. japonicum*	1DP8	2.5	II	1.76	1.14	154	2.10	[62]
Cyt c from *Alcaligenes xylosoxidans*	1E85	1.35	II	2.03	1.16	125	5-Coord.	[63]
				1.92		132		
Cyt cd1 NiR from *P. pantotropha*	1AOM	1.8	II	2.0	1.37	128	1.98	[64]
Cyt cd1 NiR from *P. aeruginosa*	1NNO	2.65	II	1.8	1.15	140	1.98	[65]
Cyt c from *Rhodobacter sphaeroides*	1DW2	2.20	II	1.75	1.42	113	2.23	[66]
			II	1.82	1.37	112	2.16	
Horse Hb		2.8		1.74	1.1	145		[67]
Hb (βcysSNOH) α heme	1BUW	1.8	II	1.75	1.13	131	2.28	[68]
β heme			II	1.74	1.11	123	2.28	[68]
T-state human Hb α heme	1RPS	2.15	II	1.72	1.13	138	5-coord.	[69]
β heme			II	1.75	1.15	128	2.25	
T-state human Hb (βcysSNOH)	1RQ4	2.11						
α heme				1.72	1.15	138	5-coord.	[69]
β heme				1.76	1.17	138	2.19	
T-state human Hb βW37E	1RQA	2.11						
α heme				1.71	1.16	135	2.24	[69]
β heme				1.76	1.18	126	2.19	[69]
R-state human Hb	4N8T	1.90	II					
α heme				1.8	1.2	138	2.0	[70]
β heme				2.1	1.2	125	2.0	
Human Hb with NO from prodrug	5E29	1.85	II					
α heme				1.6	1.1	143	3.4	[71]
β heme				-	-	-	-	
Hb from *Trematomus bernacchii*	4G51	2.5		1.8	1.2	173	2.1	
				1.8	1.2	176	2.1	[72]
				1.8	1.1	171	2.1	
				1.8	1.2	178	2.1	
Peroxidase from *Arthromyces ramosus*	2E3A	1.3		2.0	1.2	125	2.1	[73]
Peroxidase from *Glycine max*								
WT	2GHH	2.01		1.7	1.4	145	2.1	
W41A	2GHC	1.25		1.8	1.4	129 (alt. 1)	2.1	[74]
				1.8	1.4	117 (alt. 2)	2.1	
H-NOX domain of sGC from	2O0C	2.6		1.8 (A)	1.1 (A)	143 (A)	2.2 (A)	[75]
				1.8 (B)	1.2 (B)	157 (B)	2.2 (B)	

[a] Most nitrosylated sites are hexacoordinate of the form (por)Fe(NO)(His), except noted as "5-coord" which stands for the pentacoordinate sites.
[b] Formal oxidation state of iron if known.
[c] This work.

The hydrophilic orientation of NO ligand in the distal pocket of Mb H64A and H64Q mutants were stabilized by the H-bonds between the terminal O atom of NO and the water bridge in H64A mutant or the Gln64 in H64Q mutant. The H-bonds pull NO towards the heme plane, which resulted to more acute ∠Fe-N-O angles (115° in H64A and 122° in H64Q) than that seen in the wt (138°) and V68A/I107Y (142°) proteins (Table 2-4), and also than that in most nitrosyl hemeproteins (Table 2-5). Surprisingly, there is no published data to show the significant orientation change of NO ligand caused by the distal residues.

The orientational disorder of an NO ligand in an iron porphyrin model is known. Silvernail et al. [76] showed that there is no significant difference on the potential energy between two (opposite) NO orientations in a series of six-coordinate iron porphyrinates using computational methods. However, the O atoms of NO that rotate from the original position (O1) to the second position (O1b) in these iron porphyrinates did experience an energy barrier for rotation. Results from their calculations on Mb-NO derivatives (1NPF and 1HJT) were used to conclude that the distal pocket locks the NO ligand in only one orientation. Further DFT calculation on model [Fe(porphine)(NO)(1-MeIm)] systems, however, displayed a low-energy transition with a very small ~1.5 kJ/mol energy barrier when the O atom of NO ligand rotated from 0°, the initial configuration which is coplanar with 1-MeIm (0°) and pointing to a meso carbon atom, to 180°. These two positions are “equivalent” to the hydrophobic (0°) and hydrophilic (180°) position of NO in our Mb-NO derivatives.

These calculated data draw our attention to find other possible factors that control the NO orientation in Mb-NO derivatives. All our Mb-NO derivatives result from the reduction of Mb-NO_2 derivatives. Before the reduction of nitrite to nitric oxide, the nitrite ligands in our four Mb proteins are all accommodated in the hydrophobic side of distal pocket with O atom bound to Fe. We are interesting how the distal pocket controls the setting of the NO ligand into two different orientations (H64A and H64Q vs. wt and V68A/I107Y) after the reduction of nitrite. Further calculations regarding the formation mechanism of different NO orientations are ongoing with our computational collaborator.

2.4.3 The NO ligand was differentiated from HNO by protein IR spectroscopy.

The unique NO orientation in H64A and H64Q resembles that expected for HNO bonding with heme iron [77]. If the O atom of NO formed an H-bond with the water bridge in H64A or with Gln64 at the hydrophilic side of the porphyrin, the N atom of NO has more available space to form the possible Fe-HNO derivative (see the diagram below).

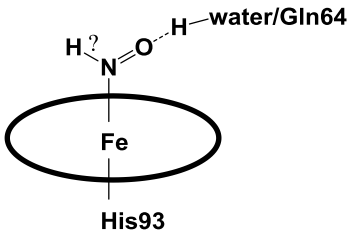

In order to more clearly characterize the NO complexes and differentiate them from HNO, IR spectroscopy was applied to distinguish these Mb-NO and Mb-HNO possibilities by obtaining the vibrational frequency of NO (ν_{NO}). For example, the ν_{NO} of wt Mb-HNO is 1385 cm^{-1} which is far from the ν_{NO} in ferrous Mb-NO at 1613 cm^{-1} [78, 79]. From the difference spectra in Fig. 2-16, the NO vibrational frequencies for the four Mb-NO derivatives are 1650 cm^{-1} in wt, 1642 cm^{-1} in H64A, 1646 cm^{-1} in H64Q and 1646 cm^{-1} in V68A/I107Y. Based on these results, we confirm that the nitrosyl ferrous Mb (Mb-NO) derivatives rather than the Mb-HNO derivatives were formed, since the NO stretching frequencies are all within the ν_{NO} range of ferrous Mb-NO [78, 79].

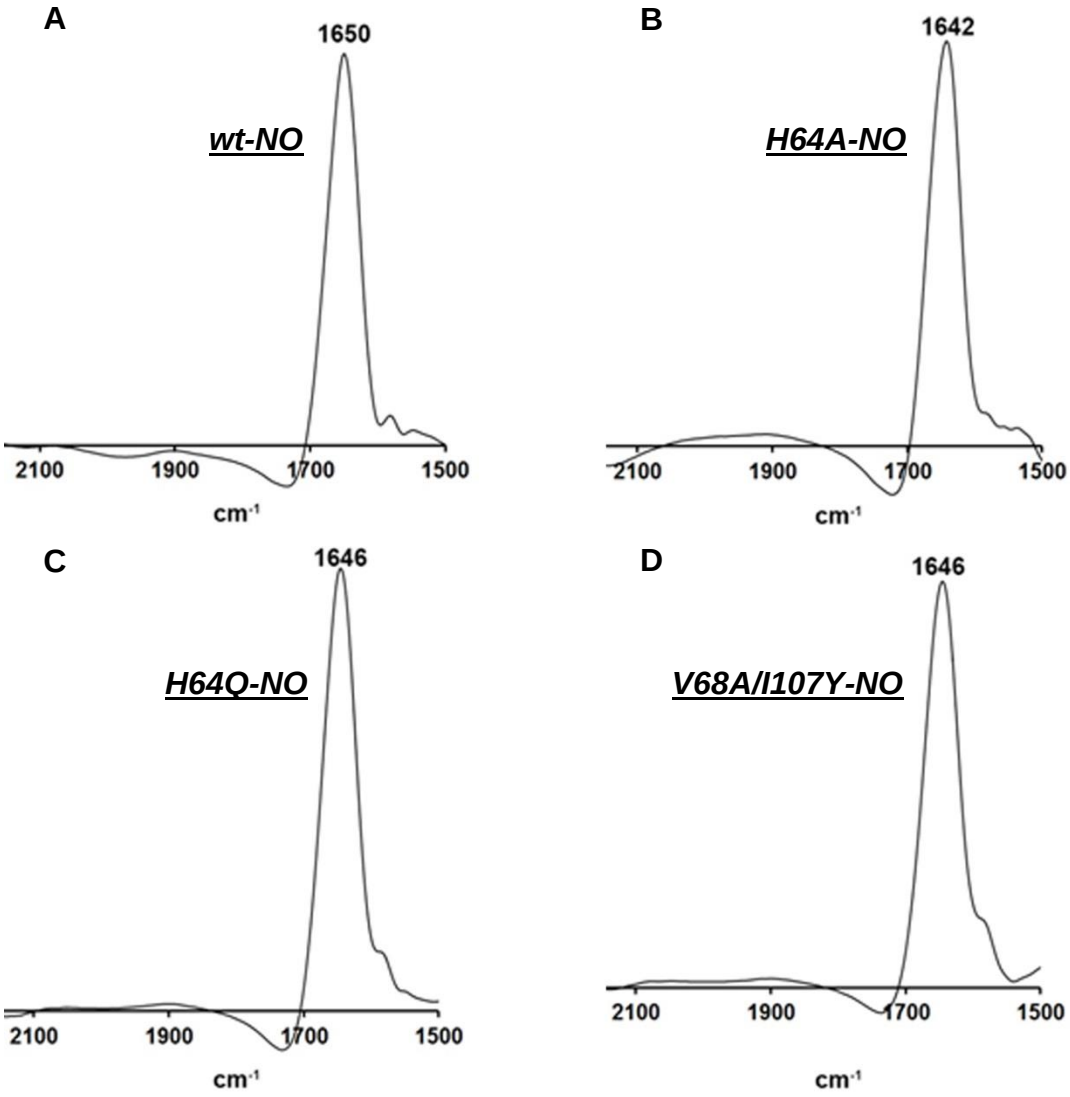

Fig. 2-16. Infrared difference spectra showing the NO bands in the four sw Mb-NO derivatives: wt (A); H64A (B); H64Q (C); V68A/I107Y (D). The difference spectrum upon the formation of Mb-NO complex was obtained from the subtracted spectrum of the *aquamet* Mb and the complex Mb-NO prepared by the nitrite/dithionite method. Phosphate buffer (0.1 M, pH 7.4) is the only solvent used throughout the entire experiments. The spectra of *aquamet* Mbs were abtained from 10 µl of 0.4-0.7 mM protein solution plus 7 µl of buffer. The spectra of Mb-NO complexes were obtained from 10 µl of the same protein with addition of 1 µl 10 M sodium nitrite for 5 min and the followed addition of 6 µl 1.7 M dithionite. The complex spectra were recorded within 1 min at 22 °C.

2.4.4 Ferric H64Q Mb shows a significant red-shift when reacted with nitrite.

The spectra of the four *aquamet* forms of sw Mb show no significant differences. The wt absorbs at 408 nm in the Soret region and 500 nm in the Q region. H64A and H64Q also have maximum absorbances at 408 nm (Soret band) and 505 nm (Q band). The V68A/I107Y showed slightly different absorbance at 407 nm (Soret band) and at 494 nm (Q band). No significant differences in the spectra were observed when these four sw Mbs were reduced to their deoxy form or when they formed the NO derivatives. When reacted with nitrite, the precursor ferric Mbs experienced red-shifts. However, H64Q showed a much larger red-shift. Further exploration for H64Q-NO_2 is needed to ascertain the reaction for this observation.

Other than the nitrite ligand coordinated with heme iron, the X-ray crystal structure of the H64Q-nitrite complex contains additional nitrite ions in the Xenon pockets $Xe_{1\text{-}3}$. We note that Xe cavities are also connected to each other to form an interior channel (see Fig. 2-17), which agrees with the previous reported data [80]. The Xe_4 position does not hold a nitrite probably due to the quick transfer to Xe_2 position [81]. We do also observe two nitrite ions on the surface of Mb around the area of Xe_3. We propose that the H64Q mutant crystal adopts this ligand entry pathway: $Xe_4 \rightarrow Xe_2 \rightarrow Xe_1 \rightarrow Xe_3$. Interestingly, this is the only mutant that we observe with nitrite ions in the Xe positions. The relatively large red-shift in the reaction of H64Q and nitrite may relate to this special interaction mode with nitrite.

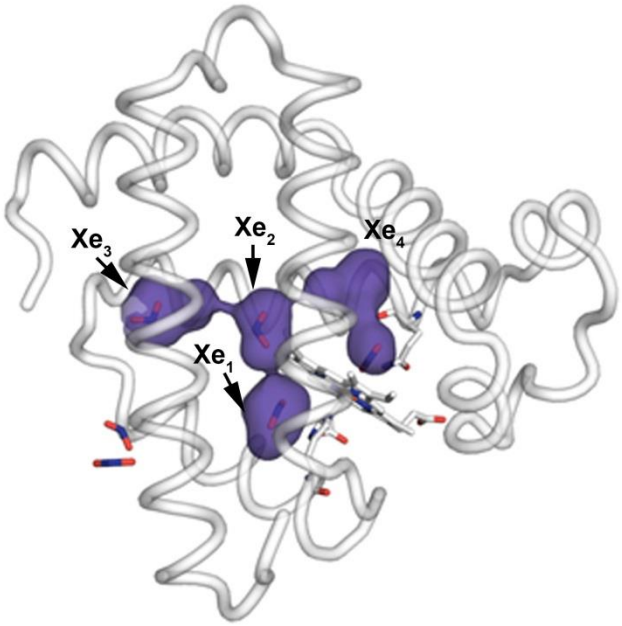

Fig. 2-17. Overview of the possible nitrite channel (magenta) in sw Mb H64Q-NO_2. The interior surface, calculated by the program *HOLLOW* and presented by *Pymol*, describes the contour of the nitrite channel. Other than the heme binding nitrite, there are other three nitrites trapped in the Xe_2, Xe_1 and Xe_3 positions.

2.5 References

1. Brooks, J., The action of nitrite on haemoglobin in the absence of oxygen. *P. Roy. Soc. B-Bio. Sci.* **1937**, *123*, 368-382.
2. Doyle, M.P., et al., Kinetics and Mechanism of the Oxidation of Human Deoxyhemoglobin by Nitrites. *J. Biol. Chem.* **1981**, *256*, 2393-2398.
3. Cosby, K., et al., Nitrite reduction to nitric oxide by deoxyhemoglobin vasodilates the human circulation. *Nat. Med.* **2003**, 9, 1498-1505.
4. Nagababu, E., et al., Active nitric oxide produced in the red cell under hypoxic conditions by deoxyhemoglobin-mediated nitrite reduction. *J. Biol. Chem.* **2003**, *278*, 46349-46356.
5. Shiva, S., et al., Deoxymyoglobin is a nitrite reductase that generates nitric oxide and regulates mitochondrial respiration. *Circ. Res.* **2007**, *100*, 654-661.
6. Rassaf, T., et al., Nitrite reductase function of deoxymyoglobin - Oxygen sensor and regulator of cardiac energetics and function. *Circ. Res.* **2007**, *100*, 1749-1754.
7. Ormerod, J.O.M., et al., The role of vascular myoglobin in nitrite-mediated blood vessel relaxation. *Cardiovasc. Res.* **2011**, *89*, 560-565.
8. Williams, P.A., et al., Haem-ligand switching during catalysis in crystals of a nitrogen-cycle enzyme. *Nature* **1997**, *389*, 406-12.
9. Crane, B.R., L.M. Siegel, and E.D. Getzoff, Probing the catalytic mechanism of sulfite reductase by X-ray crystallography: structures of the Escherichia coli hemoprotein in complex with substrates, inhibitors, intermediates, and products. *Biochemistry* **1997**, *36*, 12120-37.
10. Einsle, O., et al., Mechanism of the six-electron reduction of nitrite to ammonia by cytochrome c nitrite reductase. *J. Am. Chem. Soc.* **2002**, *124*, 11737-45.
11. Lukat, P., et al., Binding and reduction of sulfite by cytochrome c nitrite reductase. *Biochemistry* **2008**, *47*, 2080-6.
12. Yi, J., M.K. Safo, and G.B. Richter-Addo, The nitrite anion binds to human hemoglobin via the uncommon O-nitrito mode. *Biochemistry* **2008**, *47*, 8247-9.
13. Copeland, D.M., et al., Crystal structures of the nitrite and nitric oxide complexes of horse heart myoglobin. *J. Inorg. Biochem.* **2006**, *100*, 1413-25.
14. Yi, J., et al., The distal pocket histidine residue in horse heart myoglobin directs the O-binding mode of nitrite to the heme iron. *J. Am, Chem. Soc.* **2009**, *131,* 18119-28.
15. Zahran, Z.N., et al., Crystal structures of manganese- and cobalt-substituted myoglobin in complex with NO and nitrite reveal unusual ligand conformations. *J. Inorg. Biochem.* **2008**, *102*, 216-33.
16. Yi, J., et al., Synchrotron X-ray-induced photoreduction of ferric myoglobin nitrite crystals gives the ferrous derivative with retention of the O-bonded nitrite ligand. *Biochemistry* **2010**, *49*, 5969-71.

17. Yi, J., L.M. Thomas, and G.B. Richter-Addo, Distal pocket control of nitrite binding in myoglobin. *Angew. Chem. Int. Edit.* **2012**, *51*, 3625-7.
18. Quillin, M.L., et al., High-resolution crystal structures of distal histidine mutants of sperm whale myoglobin. *J. Mol. Biol.* **1993**, *234*, 140-55.
19. Springer, B.A. and S.G. Sligar, High-level expression of sperm whale myoglobin in Escherichia coli. *Proc. Natl. Acad. Sci.* **1987**, *84,* 8961-5.
20. Phillips, G.N., Jr., et al., Crystal structure of myoglobin from a synthetic gene. *Proteins* **1990**, *7*, 358-65.
21. Smith, R.D., Correlations between bound n-alkyl isocyanide orientations and pathways for ligand binding in recombinant myoglobins. Rice University (Doctoral dissertation) **1999**.
22. Leslie, A.G. and H.R. Powell, Processing diffraction data with MOSFLM, in Evolving methods for macromolecular crystallography. *Springer netherlands* **2007**, 41-51.
23. Otwinowski, Z. and W. Minor, Processing of X-ray diffraction data collected in oscillation mode. *Method. Enzymol.* **1997**, *276*, 307-326.
24. Evans, P.R. and G.N. Murshudov, How good are my data and what is the resolution? *Acta Crystallogr. D* **2013**, *69*, 1204-1214.
25. Winn, M.D., et al., Overview of the CCP4 suite and current developments. *Acta Crystallogr. D* **2011**, *67*, 235-242.
26. McCoy, A.J., et al., Phaser crystallographic software. *J. Appl. Crystallogr.* **2007**, *40*, 658-674.
27. Murshudov, G.N., A.A. Vagin, and E.J. Dodson, Refinement of macromolecular structures by the maximum-likelihood method. *Acta Crystallogr. D* **1997**, *53*, 240-55.
28. Afonine, P.V., et al., Towards automated crystallographic structure refinement with phenix.refine. *Acta Crystallogr. D* **2012**, *68*, 352-67.
29. Emsley, P. and K. Cowtan, Coot: model-building tools for molecular graphics. *Acta Crystallogr. D* **2004**, *60*, 2126-32.
30. Chen, V.B., et al., MolProbity: all-atom structure validation for macromolecular crystallography. *Acta Crystallogr. D* **2010**, *66*, 12-21.
31. Schrodinger, LLC, The PyMOL Molecular Graphics System, Version 1.3r1. **2010**.
32. Read, R.J. and A.J. Schierbeek, A Phased Translation Function. *J. Appl. Crystallogr.* **1988**, *21*, 490-495.
33. Wanat, A., et al., Nitrite binding to metmyoglobin and methemoglobin in comparison to nitric oxide binding. *J. Biol. Inorg. Chem.* **2002**, *7*, 165-76.
34. Lambrou, A. and E. Pinakoulaki, Resonance Raman detection of the myoglobin nitrito heme Fe-O-N=O/2-nitrovinyl species: implications for helix E-helix F interactions. *Phys. Chem. Chem. Phys.* **2015**, *17*, 3841-9.
35. Mansuy, D., J.C. Chottard, and G. Chottard, Nitrosoalkanes as Fe(II) ligands in the hemoglobin and myoglobin complexes formed from nitroalkanes in reducing conditions. *Eur. J. Biochem.* **1977**, *76*, 617-23.
36. Duprat, A.F., et al., Myoglobin No at Low Ph - Free 4-Coordinated Heme in the Protein Pocket. *Biochemistry* **1995**, *34*, 2634-2644.

37. Kendrew, J.C., et al., A three-dimensional model of the myoglobin molecule obtained by x-ray analysis. *Nature* **1958**, *181*, 662-6.
38. Brucker, E.A., et al., High resolution crystal structures of the deoxy, oxy, and aquomet forms of cobalt myoglobin. *J. Biol. Chem.* **1996**, *271*, 25419-22.
39. Brucker, E.A., et al., Nitric oxide myoglobin: crystal structure and analysis of ligand geometry. *Proteins* **1998**, *30*, 352-6.
40. Sundararajan, M. and F. Neese, Distal Histidine Modulates the Unusual O-Binding of Nitrite to Myoglobin: Evidence from the Quantum Chemical Analysis of EPR Parameters. *Inorg. Chem.* **2015**, *54*, 7209-7217.
41. Copeland, D.M., A.H. West, and G.B. Richter-Addo, Crystal structures of ferrous horse heart myoglobin complexed with nitric oxide and nitrosoethane. *Proteins* **2003**, *53*, 182-92.
42. Rich, A.M., et al., Determination of Fe-ligand bond lengths and the Fe-N-O bond angles in soybean ferrous and ferric nitrosylleghemoglobin a using multiple-scattering XAFS analyses. *Biochemistry* **1999**, *38*, 16491-9.
43. Schreiter, E.R., et al., S-nitrosylation-induced conformational change in blackfin tuna myoglobin. *J. Biol. Chem.* **2007**, *282*, 19773-80.
44. Ding, X.D., et al., Nitric oxide binding to the ferri- and ferroheme states of nitrophorin 1, a reversible NO-binding heme protein from the saliva of the blood-sucking insect, Rhodnius prolixus. *J. Am. Chem. Soc.* **1999**, *121*, 128-138.
45. A. Weichsel, W.R.M., deposited with the PDB (PDB access code 1T68).
46. Roberts, S.A., et al., Ligand-induced heme ruffling and bent NO geometry in ultra-high-resolution structures of nitrophorin 4. *Biochemistry* **2001**, *40*, 11327-11337.
47. Kondrashov, D.A., et al., Protein functional cycle viewed at atomic resolution: Conformational change and mobility in nitrophorin 4 as a function of pH and NO binding. *Biochemistry* **2004**, *43*, 13637-13647.
48. Maes, E.M., et al., Role of binding site loops in controlling nitric oxide release: Structure and kinetics of mutant forms of nitrophorin. *Biochemistry* **2004**, *43*, 6679-6690.
49. Maes, E.M., et al., Ultrahigh resolution structures of nitrophorin 4: heme distortion in ferrous CO and NO complexes. *Biochemistry* **2005**, *44*, 12690-9.
50. A.M. Amoia, W.R.M., deposited with the PDB (PDB access code 2AT0).
51. A.M. Amoia, W.R.M., deposited with the PDB (PDB access code 2OFR).
52. V.A. Issaian, A.W., W.R. Montfort, deposited with the PDB (PDB access code 4GRJ).
53. Knipp, M., et al., Structure and dynamics of the membrane attaching nitric oxide transporter nitrophorin 7*. F1000Res*. **2015**, *4*, 45.
54. Friedman, J., et al., Crystal structures of the NO- and CO-bound heme oxygenase from Neisseriae meningitidis - Implications for O-2 activation. *J. Bio. Chem.* **2003**, *278*, 34654-34659.

55. Sugishima, M., et al., Crystal structures of ferrous and CO-, CN--, and NO-bound forms of rat heme oxygenase-1 (HO-1) in complex with heme: Structural implications for discrimination between CO and O-2 in HO-1. *Biochemistry* **2003**, *42*, 9898-9905.
56. Lad, L., et al., Crystal structures of the ferric, ferrous, and ferrous-NO forms of the Asp140Ala mutant of human heme oxygenase-1: Catalytic implications. *J. Mol. Bio.* **2003**, *330*, 527-538.
57. Lad, L., P.R. Ortiz de Montellano, and T.L. Poulos, Crystal structures of ferrous and ferrous-NO forms of verdoheme in a complex with human heme oxygenase-1: catalytic implications for heme cleavage. *J. Inorg. Biochem.* **2004**, *98*, 1686-1695.
58. Lad, L., et al., Crystal structures of the G139A, G139A-NO and G143H mutants of human heme oxygenase-1. A finely tuned hydrogen-bonding network controls oxygenase versus peroxidase activity. *J. Biol. Inorg. Chem.* **2005**, *10*, 138-46.
59. Wang, J., et al., Regiospecificity determinants of human heme oxygenase: differential NADPH- and ascorbate-dependent heme cleavage by the R183E mutant. *J. Biol. Chem.* **2005**, *280*, 2797-806.
60. Sugishima, M., et al., Crystal structure of dimeric heme oxygenase-2 from Synechocystis sp PCC 6803 in complex with heme. *Biochemistry* **2005**, *44*, 4257-4266.
61. Harutyunyan, E.H., et al., The binding of carbon monoxide and nitric oxide to leghaemoglobin in comparison with other haemoglobins. *J. Mol. Biol.* **1996**, *264*, 152-161.
62. Gong, W.M., B. Hao, and M.K. Chan, New mechanistic insights from structural studies of the oxygen-sensing domain of Bradyrhizobium japonicum FixL. *Biochemistry* **2000**, *39*, 3955-3962.
63. Lawson, D.M., et al., Unprecedented proximal binding of nitric oxide to heme: implications for guanylate cyclase. *Embo J.* **2000**, *19*, 5661-5671.
64. Williams, P.A., et al., Haem-ligand switching during catalysis in crystals of a nitrogen-cycle enzyme. *Nature* **1997**, *389*, 406-412.
65. Nurizzo, D., et al., Conformational changes occurring upon reduction and NO binding in nitrite reductase from Pseudomonas aeruginosa. *Biochemistry* **1998**, *37*, 13987-13996.
66. Leys, D., et al., Crystal structures of an oxygen-binding cytochrome c from Rhodobacter sphaeroides. *J. Biol. Chem.* **2000**, *275*, 16050-16056.
67. Deatherage, J.F. and K. Moffat, Structure of Nitric-Oxide Hemoglobin. *J. Mol. Biol.* **1979**, ***134***, 401-417.
68. Chan, N.L., P.H. Rogers, and A. Arnone, Crystal structure of the S-nitroso form of liganded human hemoglobin. *Biochemistry* **1998**, *37*, 16459-16464.
69. Chan, N.L., et al., Crystallographic analysis of the interaction of nitric oxide with quaternary-T human hemoglobin. *Biochemistry* **2004**, *43*, 118-132.

70. Yi, J., A.S. Soares, and G.B. Richter-Addo, Crystallographic characterization of the nitric oxide derivative of R-state human hemoglobin. *Nitric Oxide-Biol. Ch.* **2014**, *39*, 46-50.
71. Xu, G.G., et al., *Design,* Synthesis, and Investigation of Novel Nitric Oxide (NO)-Releasing Prodrugs as Drug Candidates for the Treatment of Ischemic Disorders: Insights into NO-Releasing Prodrug Biotransformation and Hemoglobin-NO Biochemistry. *Biochemistry* **2015**, *54*, 7178-92.
72. Merlino, A., et al., Selective X-ray-induced NO photodissociation in haemoglobin crystals: evidence from a Raman-assisted crystallographic study. *Acta Crystallogr. D* **2013**, *69*, 137-140.
73. Fukuyama, K. and T. Okada, Structures of cyanide, nitric oxide and hydroxylamine complexes of Arthromyces ramosusperoxidase at 100 K refined to 1.3 A resolution: coordination geometries of the ligands to the haem iron. *Acta Crystallogr. D* **2007**, ***63***, 472-7.
74. Badyal, S.K., et al., Conformational mobility in the active site of a heme peroxidase. *J. Biol. Chem.* **2006**, *281*, 24512-20.
75. Ma, X.L., et al., NO and CO differentially activate soluble guanylyl cyclase via a heme pivot-bend mechanism. *Embo. J.* **2007**, *26*, 578-588.
76. Silvernail, N.J., et al., Mapping NO Movements in Crystalline [Fe(Porph)(NO)(1-MeIm)]. *J. Am. Chem. Soc.* **2009**, *131*, 2131-2140.
77. Lin, R. and P.J. Farmer, The HNO adduct of myoglobin: Synthesis and characterization. *J. Am. Chem. Soc.* **2000**, *122*, 2393-2394.
78. Immoos, C.E., et al., Bonding in HNO-myoglobin as characterized by X-ray absorption and resonance Raman spectroscopies. *J. Am. Chem. Soc.* **2005**, *127*, 814-815.
79. Ling, Y., et al., NMR, IR/Raman, and structural properties in HNO and RNO (R = alkyl and aryl) metalloporphyrins with implication for the HNO-myoglobin complex. *J. Am. Chem. Soc.* **2010**, *132*, 1583-91.
80. Tilton, R.F., Jr., I.D. Kuntz, Jr., and G.A. Petsko, Cavities in proteins: structure of a metmyoglobin-xenon complex solved to 1.9 A. *Biochemistry* **1984**, *23*, 2849-57.
81. Nishihara, Y., et al., The escape process of carbon monoxide from myoglobin to solution at physiological temperature. *J. Am. Chem. Soc*. **2004**, *126*, 11877-88.

Chapter 3 Organometallic myoglobins: Formation of Fe-carbon bonds and distal pocket effects on aryl ligand conformations

3.1 Introduction

Arylhydrazines ($ArNHNH_2$; Ar = aryl) occur in nature and are important chemical species in both the agrochemical and pharmaceutical industries [1]. Synthetic hydrazines are also prevalent in the general environment [2]. In some cases, hydrazines are beneficial components of pharmaceutical drugs such as the antidepressant drugs isoniazid and phenelzine, but are also toxic and can act as cancer causative agents [1, 2]. For example, the newly FDA-approved drug DUOPA® for Parkinson's disease contains the substituted hydrazine carbidopa with a known hemolytic anemia side effect. The parent hydrazine (NH_2NH_2) is found in tobacco and tobacco smoke [3]. Hydrazines are also present in certain foods. For example, 4-hydroxymethylphenylhydrazine is generated as a metabolite from agaritine, a food component from the edible commercial mushroom *Agaris bisporus* [4].

Phenylhydrazine is toxic to red blood cells [5], and the hemoglobin-phenylhydrazine reaction has been used to model hemolytic anemia. Interactions of substituted hydrazines with human hemoglobin (Hb) may also result in hemolysis, Heinz-body formation, and degradation of the protein [6]. Related interactions of substituted hydrazines and diazenes (RN=NH) with other heme proteins such as myoglobin (Mb) [7-9], cyt P450 [10-12], and

catalase [13] have been reported [14]. The generated products often contain heme σ-aryl bonds with direct Fe–C(aryl) linkages (Scheme 1) as determined by UV-vis and NMR spectroscopy. In some cases, an Fe–to–N(porphyrin) migration of the aryl ligand (Scheme 1; right) occurs upon extraction of the heme from the protein, or occurs within the heme protein active site (for P450) [14].

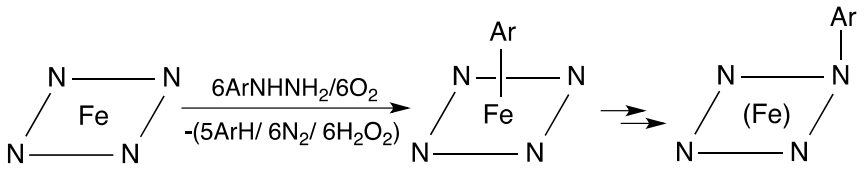

Scheme 1. Formation of σ-aryl (middle) and *N*-aryl (right) products from the reaction of arylhydrazines with heme proteins. The heme is designated by the N_4Fe plane.

Only two X-ray crystal structures have been reported to date for such heme protein σ-aryl species. The crystal structure of the prototypical wild-type sperm whale Mb–phenyl complex, obtained from the reaction of Mb with phenylhydrazine, was published by Ringe and Ortiz de Montellano and coworkers in 1984 [7]. The crystal structure of the P450cam–phenyl complex obtained from the reaction with phenyldiazene, was reported by Poulos and Ortiz de Montellano and coworkers in 1990 [12].

The potential of arylhydrazines to serve as steric probes for heme protein active sites has been evaluated [14]. It is well established that the arylhydrazine reactions with heme proteins proceed via carbon-based radicals [15, 16] formed during aerobic reaction with the protein en route to Fe–C bond formation [17]. New X-ray structural data that clarify which aryl C atoms bind to the Fe centers, and information regarding preferred aryl ligand orientations from reactions

involving substituted arylhydrazines as a function of active site structure are thus desirable.

I have prepared a representative set of derivatives from the reactions of arylhydrazines with wild-type and mutant Mbs (see Chapter 2) to determine the mode of attachment of the substituted aryl groups to the iron centers [18], and the effect of mutating the distal pocket H64 residue on the orientation of the aryl ligands. I chose the H64A mutant to remove distal sidechain H-bonding, and the H64Q mutant to provide an alternate H-bonding capacity in the heme pocket.

3.2 Materials and methods

3.2.1 Cloning, expression, purification, and crystallization of swMb

The methodology employed has been described previously in Chapter 2.

3.2.2 UV-vis spectroscopy of sw Mb-aryl derivatives

In order to clarify which carbon atom of the aryl group will coordinate with heme iron, three reaction precursors, phenylhydrazine and two derivatives (3-methylphenylhydrazine and 4-chlorophenylhydrazine) were used. The arylhydrazines were purchased from Sigma and used without further purification (see below).

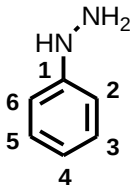

Phenylhydrazine

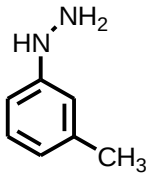

3-methylphenylhydrazine

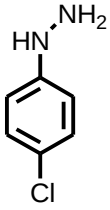

4-chlorophenylhydrazine

Protein solutions were mixed with the arylhydrazines and the reactions were monitored using a Hewlett Packard 8453 spectrophotometer. The *met*Mb protein samples in 20 mM Tris buffer, 1mM EDTA, pH 7.4 were purified as described in Chapter 2. For all the reactions, 10-15 µl of the protein samples (at 10-20 mg/ml concentration) were added into 2.5 ml of 0.1 M phosphate buffer at pH 7.4 in a cuvette to obtain the precursor spectrum. 5 µl aliquots of 0.5 M arylhydrazine solutions in phosphate buffer were added and the spectra were recorded at different time points.

3.2.3 Preparation of sw Mb-aryl derivatives for X-ray crystallography

Prior to reactions with the arylhydrazine, a representative and suitably-sized crystal of the *met*Mb-H_2O precursor was harvested for X-ray diffraction data collection and its crystal structure solved. The remaining crystals in the hanging drop were transferred into a new droplet (4 µl) on a separate cover slide that contained a solution of the arylhydrazine (0.0125 M arylhydrazine dissolved in 100 mM Tris•HCl, 1 mM EDTA, pH 7.4 or 9.0, and 3.0 M ammonium sulfate). In a manner similar to that used for cystallization employing the hanging drop vapor diffusion method, the new cover slide containing the drop was flipped over and placed on top of a well (in a 24-well format) and sealed with grease; the well contained 100 mM Tris•HCl, 1 mM EDTA, pH 7.4 or 9.0, and 3.0 M ammonium sulfate. This allowed the *met*Mb crystals in the drop to react with the arylhydrazines for a longer period (1-14 days at room temperature) without drying out. During this process, the cover slides were opened every two or three days, and the reaction solutions were exchanged with fresh aerated arylhydrazine solutions (and fresh air introduced into the well volume) in order to ensure completion of the reactions. The product crystals were harvested by cryo-loops daily or weekly, washed by cryosolution (100 mM Tris•HCl, 1 mM EDTA, pH 7.4 or 9.0, 3 M ammonium sulfate, 10% glycerol) and stored in liquid nitrogen until X-ray diffraction data collection. The vast majority of the product crystals were unusable due to loss in crystallinity as a result of the reactions. Indeed, several (patient) attempts were made, >40 per sample, until good quality X-ray diffraction data were obtained whose solution revealed

the presence of the aryl-liganded swMb-phenyl or swMb-tolyl or swMb-chlorophenyl products.

3.2.4 X-ray data collection

The diffraction data was collected at home source using a Rigaku MicroMax 007HF microfocus X-ray generator coupled to a R-AXIS IV++ detector or a PILATUS 200K detector. The data was collected at 100 K with the Cu Kα radiation (λ=1.54178 Å) from the generator operated at the working condition 40 kV/30 mA. The parameters during data collection were set up as shown in Table 3-1.

Table 3-1. Parameters of data collection

	Detector	Detector distance (mm)	Oscillation angles (º)	Range (º)	Exposure time (s)
wt-phenyl	R-AXIS IV	120	1	180	180
H64A-phenyl	PILATUS	35	0.75	118	30
H64A-tolyl	PILATUS	35	1	180	30
H64A-chlorophenyl	PILATUS	30	1	180	30
H64Q-phenyl (*$P2_1$*)	PILATUS	35	1.25	180	30
H64Q-tolyl (*$P2_1$*)	PILATUS	35	1.5	180	60
H64Q-chlorophenyl (*$P2_1$*)	PILATUS	35	1.25	180	30
H64Q-phenyl (*P6*)	PILATUS	30	0.5	60	30
H64Q-tolyl (*P6*)	PILATUS	30	1	142	30
V68A/I107Y-phenyl	PILATUS	35	1.5	230	30
V68A/I107Y-tolyl	PILATUS	35	1	180	30

3.2.5 Data processing, structure solution and refinement

The data was processed using HKL3000 [19]. The structure factors were calculated using the CCP4 program suite [20]. Initial phases were obtained by molecular replacement using *PHASER* (CCP4) [21]. The starting model used was wt swMb (*met*Mb-H2O) at 1.5 Å resolution (PDB accession code 2MBW) with the heme, water molecules, and ligands removed from the structure. All refinements were performed using either *Refmac5* (CCP4) or *Phenix.refine*

(PHENIX) [22, 23]. Models were rebuilt using *COOT* [24]. *MolProbity* was used for structure validation to check for unusual residue conformations contacts; details are described below [25].

The figures were generated using *Pymol* [26]. $2F_o$-F_c electron density maps were initially calculated by Fast Fourier Transform (FFT) in the CCP4 software package [27]. The resulting map files were converted to CCP4 files and displayed in *Pymol.* In general, each F_o-F_c electron density map was generated as follows: (i) a new PDB file in which ligands were removed from the pocket was initially refined for 5 cycles in Refmac5; (ii) the new mtz file that was generated from the first step was input into FFT to generate the map that was then displayed in *Pymol*. This procedure was followed in the following structures except where noted.

wt Mb-phenyl

Ten initial cycles of restrained refinement were run with *Refmac*, and the *R* factor decreased from 0.398 to 0.258. Ligands and water were added to the model based on the F_o-F_c electron density maps in the subsequent refinement cycles. Phenylheme (heme with a phenyl group attached to Fe) was drawn in *Jligand* (CCP4) to generate the heme-ligand model and the restraint file. One phenylheme, one sulfate anion and one glycerol molecule were added to the model. 66 water molecules were added iteratively using *COOT*. The N-terminal Met residue, and the residues Gln152 and Gly153 in the C-terminus were omitted due to lack of electron density. The final *R* factor and R_{free} were 0.213 and 0.278, respectively.

Mb H64A-phenyl

Ten initial cycles of restrained refinement were run with *Refmac*, and the *R* factor decreased from 0.351 to 0.260. Ligands and water were added to the model based on the F_o-F_c electron density maps in the subsequent refinement cycles. One phenylheme, six sulfate anions, and two glycerol molecules were added to the model. 202 water molecules were added iteratively using *COOT*. The anisotropic *B* values of the Fe atom and tolyl group were refined based on the difference peaks around them. Two conformations for each of the sidechains of His12, Lys78, Glu109, Asn122, Lys133 and Glu136 were modeled with 50% occupancy each. The N-terminal residue Met was omitted because of the lack of electron density. The final *R* factor and R_{free} were 0.149 and 0.187, respectively.

Mb H64A-tolyl

Ten initial cycles of restrained refinement were run with *Refmac*, and the *R* factor decreased from 0.377 to 0.266. Ligands and water were added to the model based on the F_o-F_c electron density maps in the subsequent refinement cycles. Tolylheme (heme with a tolyl group attached to Fe) was drawn in *Jligand* to generate the ligand model and the restraint file. One tolylheme and six sulfate anions were added to the model. 184 water molecules were added iteratively using *COOT*. The anisotropic *B* values of the Fe atom and tolyl group were refined based on the difference peaks around them. Two conformations for each of the sidechains of His12, Asn122 and Lys133 were modeled with

50% occupancy each. The final *R* factor and R_{free} were 0.153 and 0.179, respectively.

Mb H64A-*chlorophenyl*

Ten initial cycles of restrained refinement were run with *Refmac*, and the *R* factor decreased from 0.358 to 0.277. Ligands and water were added to the model based on the F_o-F_c electron density maps in the subsequent refinement cycles. Chlorophenylheme (heme with a chlorophenyl group attached to Fe) was drawn in *Jligand* to generate the ligand model and the restraint file. One chlorophenylheme, five sulfate anions, and two glycerol molecules were added the model. 225 water molecules were added iteratively using *COOT*. The anisotropic *B* values of the Fe atom and chlorophenyl group were refined based on the difference peaks around them. Two conformations for each of the sidechains of His12, Glu59, Leu61, Glu109, Arg118 and GLu136 were modeled with 50% occupancy each. The N-terminal Met residue was omitted because of the lack of electron density. The final *R* factor and R_{free} were 0.152 and 0.192, respectively.

Mb H64Q-phenyl in $P2_1$ space group

Ten initial cycles of restrained refinement were run with *Refmac*, and the *R* factor decreased from 0.393 to 0.241. Ligands and water were added to the model based on the F_o-F_c electron density maps in the subsequent refinement cycles. One phenylheme, two sulfate anions, and two glycerol molecules were added the model. 88 water molecules were added iteratively using *COOT*. Two conformations for each of the sidechains of Glu4 were modeled with 50%

occupancy each. The N-terminal residue Met and the C-terminal residues Gln152 and Gly153 were omitted because of the lack of electron density. The final *R* factor and R_{free} were 0.188 and 0.234, respectively.

Mb H64Q-tolyl in $P2_1$ space group

Ten initial cycles of restrained refinement were run with *Refmac*, and the *R* factor decreased from 0.406 to 0.261. Ligands and water were added to the model based on the F_o-F_c electron density map in the subsequent refinement cycles. One tolylheme, three sulfate anions and one glycerol molecule were added to the model. 119 water molecules were added iteratively using *COOT*. The anisotropic *B* values of the Fe atom and tolyl group were refined depending on the difference peaks around them. Two conformations for each of the sidechains of Glu4, Leu29 and Asn132 were modeled with 50% occupancy each. The N-terminal Met residue and the C-terminal residues Gln152 and Gly153 were omitted because of the lack of electron density. The final *R* factor and R_{free} are 0.150 and 0.199, respectively.

Mb H64Q-chlorophenyl in $P2_1$ space group

Ten initial cycles of restrained refinement were run with *Refmac*, and the *R* factor decreased from 0.413 to 0.268. Ligands and water were added to the model based on the F_o-F_c electron density map in the subsequent refinement cycles. One chlorophenylheme, three sulfate anions and one glycerol molecule were added to the model. 104 water molecules were added iteratively using *COOT*. The anisotropic *B* value of the Fe atom was refined based on the difference peaks around this central metal atom. Two conformations for each of

the sidechains of Glu4, Gln26, Gln64 and Asn132 were modeled with 50% occupancy each. The N-terminal Met residue and the C-terminal residues Gln152 and Gly153 were omitted because of the lack of electron density. The final *R* factor and R_{free} are 0.163 and 0.214, respectively.

Mb H64Q-phenyl in P6 space group

Ten initial cycles of restrained refinement were run with *Refmac*, and the *R* factor decreased from 0.343 to 0.267. Ligands and water were added to the model based on the F_o-F_c electron density map in the subsequent refinement cycles. One phenylheme, six sulfate anions, and two glycerol molecule were added to the model. 192 water molecules were added iteratively using *COOT*. The anisotropic *B* value of the Fe atom was refined based on the difference peaks around this central metal atom. Two conformations for each of the sidechains of Gln64, Val68, Lys133 and Glu136 were modeled with 50% occupancy each. The N-terminal residue Met was omitted because of the lack of electron density. The final *R* factor and R_{free} are 0.171 and 0.210, respectively.

Mb H64Q-tolyl in P6 space group

Three initial cycles of restrained refinement were run with *Phenix.refine*, and the *R* factor decreased from 0.339 to 0.214. Ligands and water were added to the model based on the F_o-F_c electron density map in the subsequent refinement cycles. One tolylheme, six sulfate anions, and one glycerol molecule were added to the model. 235 water molecules were added iteratively using *COOT*. The anisotropic *B* value of the Fe atom was refined based on the

difference peaks around this central metal atom. Two conformations for each of the sidechains of His12, Leu29, Gln64, Val68, Glu109, Lys133 and Glu136 were modeled with 50% occupancy each. The N-terminal residue Met was omitted because of the lack of electron density. The final *R* factor and R_{free} are 0.177 and 0.206, respectively.

Mb V68A*/I107Y-phenyl*

Ten initial cycles of restrained refinement were run with *Refmac*, and the *R* factor decreased from 0.387 to 0.275. Ligands and water were added to the model based on the F_o-F_c electron density map in the subsequent refinement cycles. One phenylheme, two sulfate anions and one glycerol molecule were added to the model. 62 water molecules were added iteratively using *COOT*. The N-terminal Met residue was omitted because of the lack of electron density. The final *R* factor and R_{free} are 0.202 and 0.252, respectively.

Mb V68A/I107Y-tolyl

Ten initial cycles of restrained refinement were run with *Refmac*, and the *R* factor decreased from 0.403 to 0.276. Ligands and water were added to the model based on the F_o-F_c electron density map in the subsequent refinement cycles. One tolylheme and two sulfate anions were added to the model. 81 water molecules were added iteratively using *COOT*. The anisotropic *B* value of the Fe atom was refined based on the difference peaks around this central metal atom. The N-terminal residue Met and the C-terminal residues Gln152 and Gly153 were omitted because of the lack of electron density. The final *R* factor and R_{free} are 0.205 and 0.292, respectively.

3.3 Results

3.3.1 Expression, purification and crystallization of sw Mb

The four proteins were expressed and purified as described in Chapter 2. As mentioned in Chapter 2, the H64Q mutant can be crystallized from a broad concentration range (2.56 to 3.2 M) of ammonium sulfate (AS) either at pH 7.4 or pH 9.0. When I was working on this project, I found that the H64Q crystals from pH 7.4 and pH 9.0 were actually in different space groups, $P2_1$ or *P6*, respectively.

3.3.2 UV-vis spectroscopy of sw Mb-aryl derivatives

3.3.2.1 The UV-vis characterization of wt sw Mb-aryls

The reaction of wt sw Mb with phenylhydrazine ($PhNHNH_2$) resulted in a decrease of the bands at 408 nm and 500 nm, and the appearance of new bands at 433 nm and 540 nm, consistent with that reported previously by Ortiz de Montellano for the wt sw Mb-phenyl complex in solution [28, 29] (Fig. 3-1A). Apparent isosbestic points were observed at ~425 nm and 486 nm. The changes between the new absorbance at 433 nm and the isosbestic point at 486 nm were plotted (Fig. 3-1B). Based on this figure, the reaction was essentially complete after ~10 mins.

Similar reaction behaviors were observed during the reactions of wt sw Mb with 3-methylphenylhydrazine (Fig. 3-1C-D) and 4-chlorophenylhydrazine (Fig. 3-1E-F). The generally accepted chemical equation for the reaction is:

$$4PhNHNH_2 + 5O_2 + 2[Fe] \longrightarrow 2[Fe\text{-}Ph] + 2PhH + 4N_2 + 5H_2O_2$$

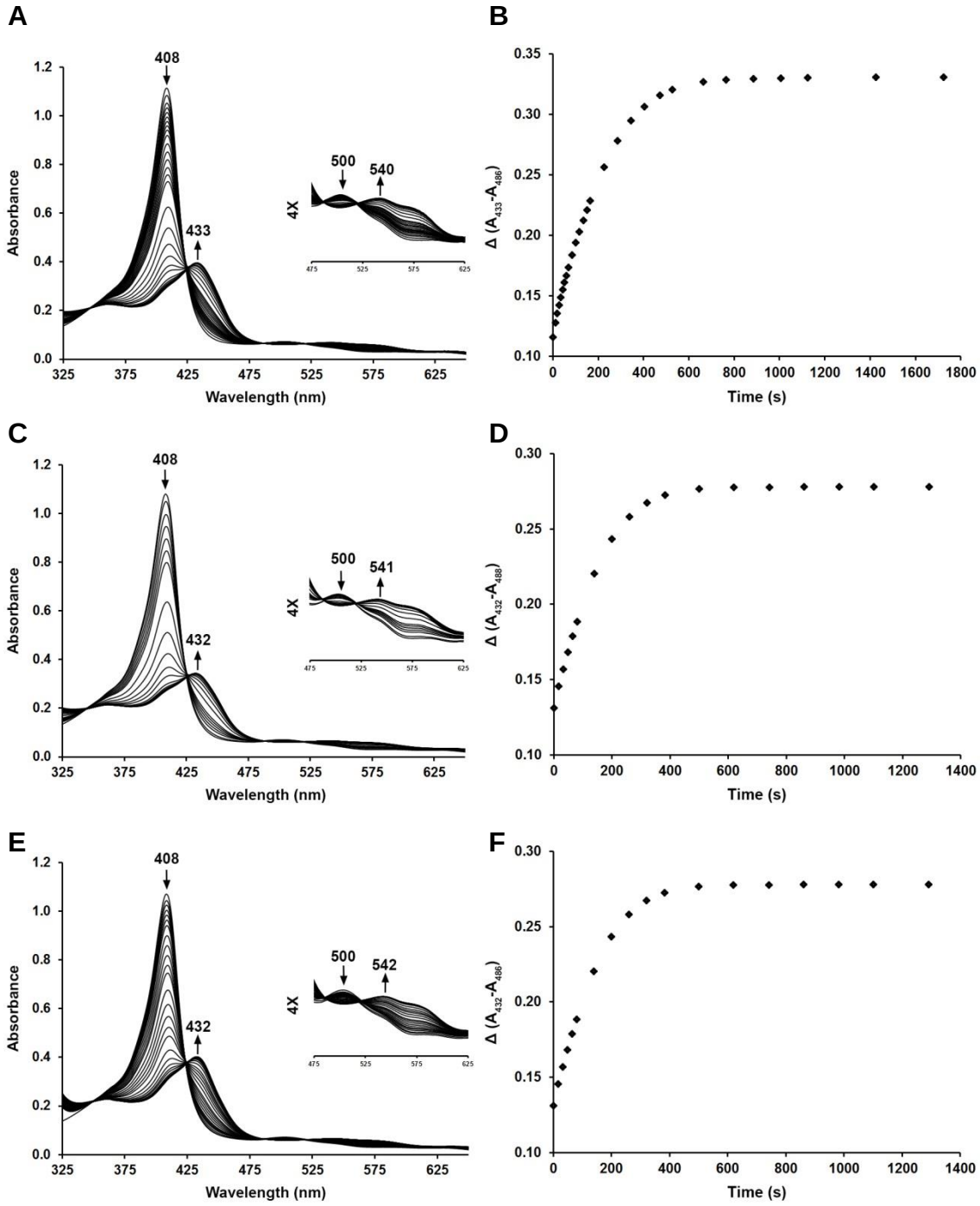

Fig. 3-1. UV-vis changes during the reactions of wt sw Mb with phenylhydrazine (A-B), 3-methylphenylhydrazine (C-D), and 4-chlorophenylhydrazine (E-F). Conditions: 0.1 M phosphate buffer, pH 7.4, [protein] = 6 µM, final [reagent] = 1 mM.

3.3.2.2 The UV-vis characterization of sw Mb H64A-aryls

The reactions of ferric sw Mb H64A and the arylhydrazines resulted in the decrease of the initial absorbances at 408 nm and 505 nm and the appearance of new bands at 436 nm and 544 nm, with an apparent isosbestic point at 479 nm (Fig. 3-2A, C, E). The reactions quickly reached completion within 1.5 mins (Fig. 3-2B, D, F).

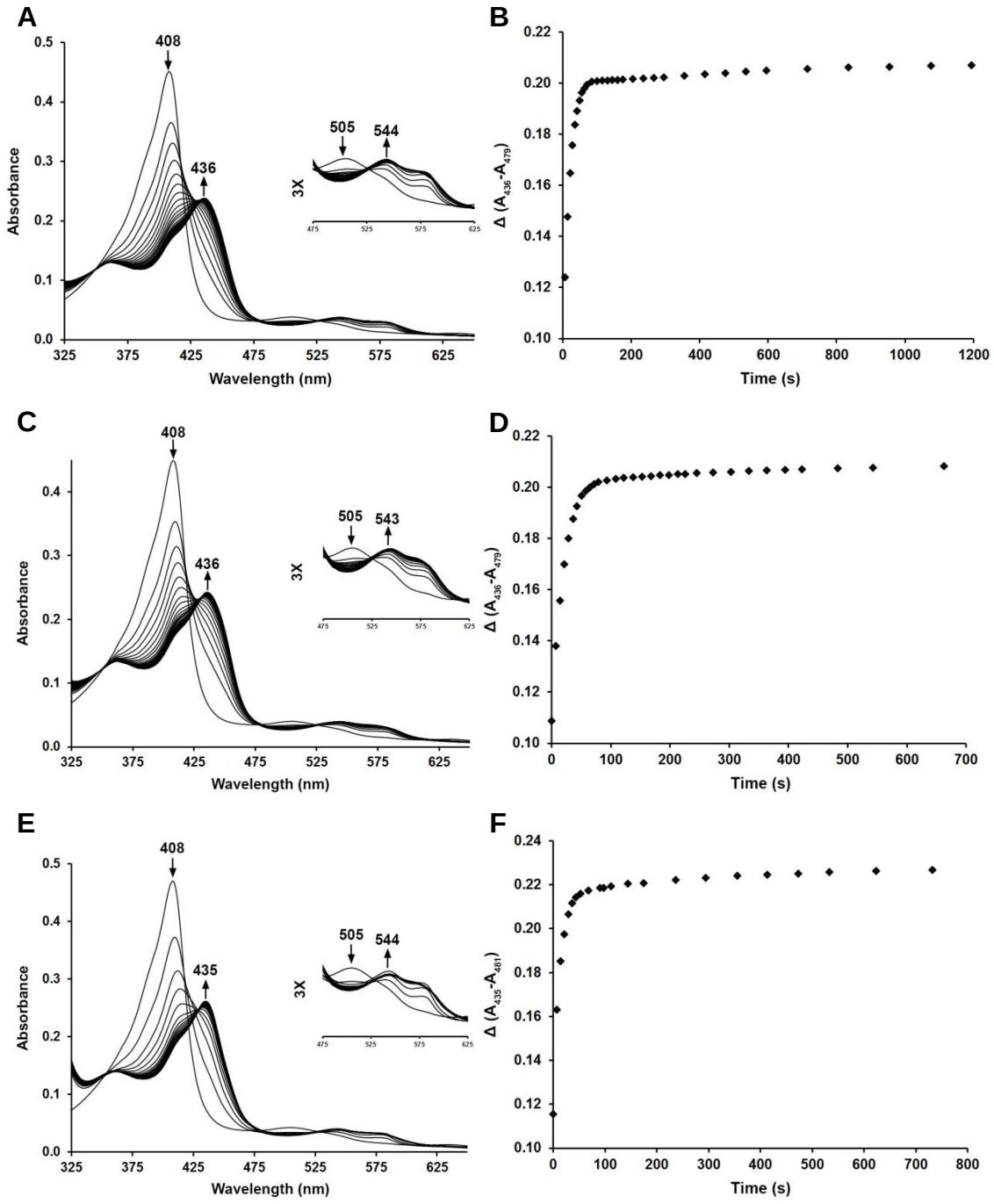

Fig. 3-2. UV-vis changes during the reactions of sw Mb H64A with phenylhydrazine (A-B), 3-methylphenylhydrazine (C-D), and 4-chlorophenylhydrazine (E-F). Conditions: 0.1 M phosphate buffer, pH 7.4 [protein] = 2 μM, final [reagent] = 1 mM.

3.3.2.3 The UV-vis characterization of sw Mb H64Q-aryls

The reaction completion times of sw Mb H64Q with the arylhydrazines are somewhat similar to those of the wt sw Mb reactions (Fig. 3-3). The reactions of H64Q with arylhydrazines in solution were essentially complete within 7 mins, slower than H64A but slightly faster than wt (Fig. 3-3B, D, F).

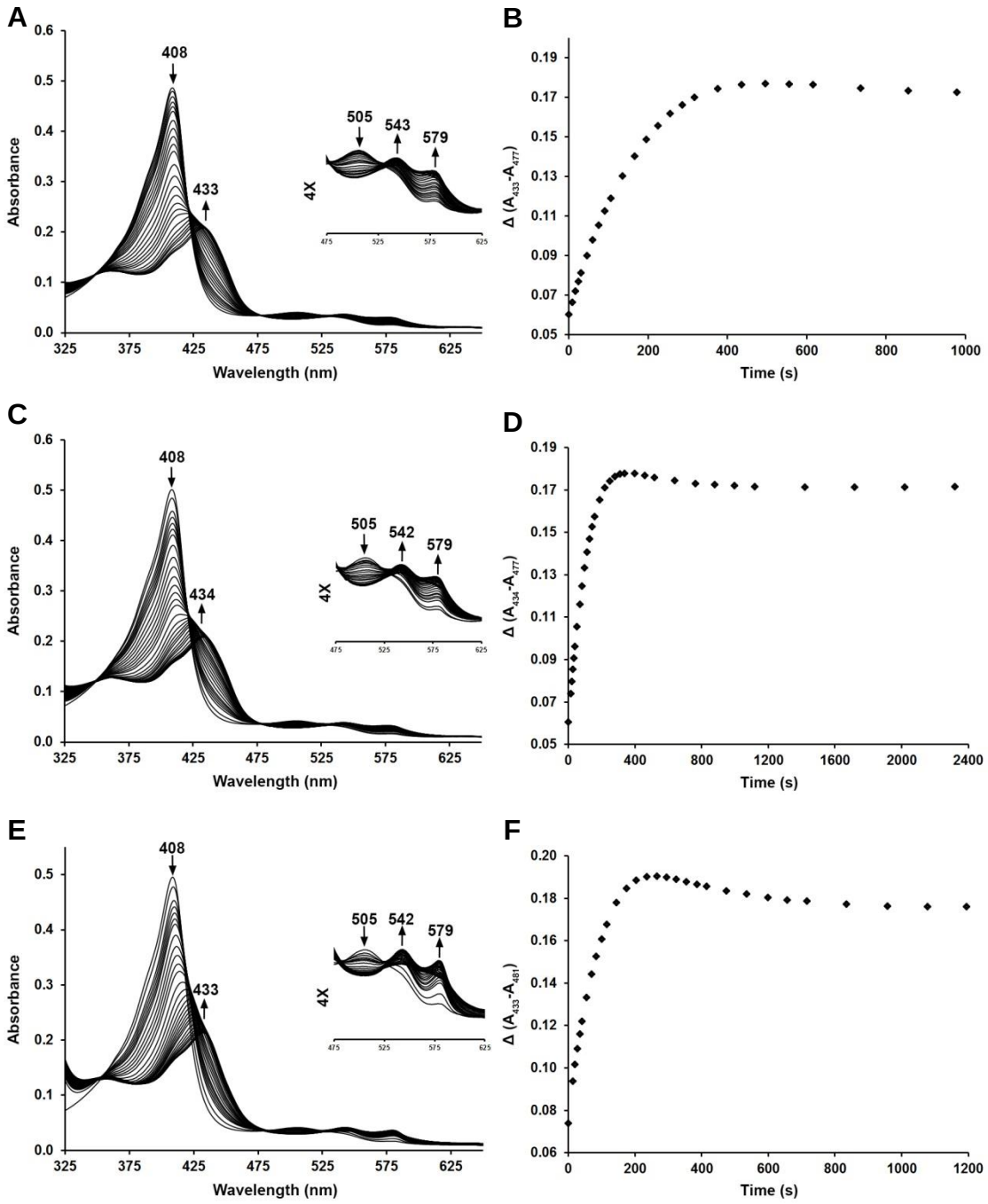

Fig. 3-3. UV-vis changes during the reactions of sw Mb H64Q with phenylhydrazine (A-B), 3-methylphenylhydrazine (C-D), and 4-chlorophenylhydrazine (E-F). Conditions: 0.1 M phosphate buffer, pH 7.4 [protein] = 3 μM, final [reagent] = 1 mM.

3.3.2.4 The UV-vis characterization of sw Mb V68A/I107Y-aryls

The reactions of the Mb double mutant V68A/I107Y with arylhydrazines took much longer to obtain the product complexes. As seen in Fig. 3-4A, after an overnight reaction with phenylhydrazine, the 407 nm Soret band slowly and only partially switched from 407 nm to 430 nm. The reaction stabilized after ~80 mins (Fig. 3-4B). The reactions with the substituted phenylhydrazine needed to proceed for at least 24 hours to partially form complexes as compared to the reaction between V68A/I107Y and phenylhydrazine (Fig. 3-4C, E). The decreases of the Soret bands at 407 nm for these reactions are plotted as shown in Fig. 3-4B, D, F.

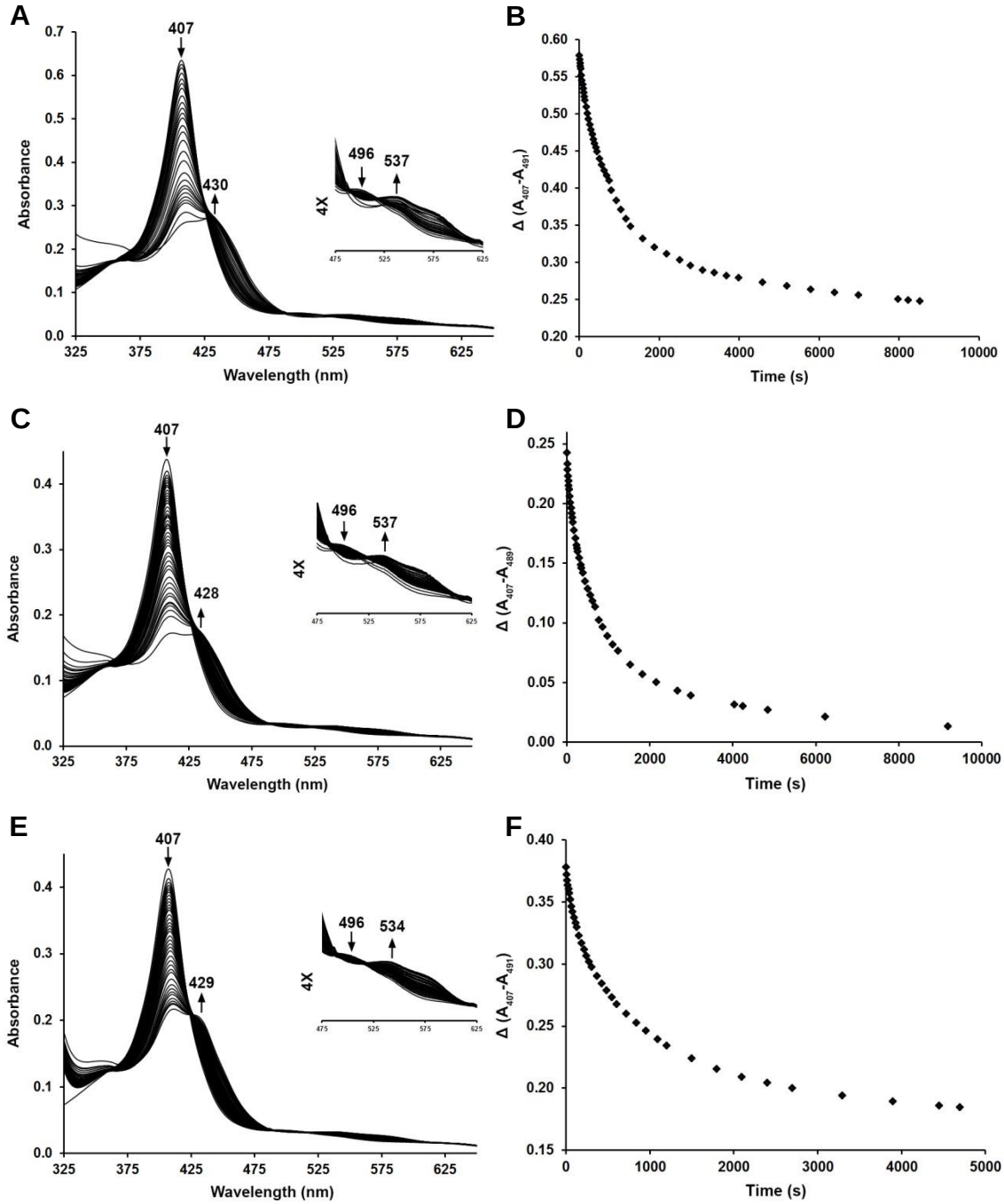

Fig. 3-4. UV-vis changes during the reactions of sw Mb V68A/I107Y with phenylhydrazine (A-B), 3-methylphenylhydrazine (C-D), and 4-chlorophenylhydrazine (E-F). Conditions: 0.1 M phosphate buffer, pH 7.4 [protein] = 2 μM, final [reagent] = 1 mM.

3.3.3 The sw Mb-aryls from the crystal soaking method with arylhydrazines

Appropriately sized *met*Mb (wt and mutants) crystals were selected and soaked with one of the three arylhydrazine solutions (phenylhydrazine or one of the two derivatives). I observed that cracking of the crystals increased the longer they were soaked with the organic precursors. Small crystals without any visible cracks were separated and selected. An important factor was thus the soaking time. If the soaking time was short, the reaction did not go to completion, and the final electron density maps in the X-ray structures were "messy". Alternatively, if the soaking time was longer ("too long"), the diffraction data was poor; likely due to crystal damage resulting from additional introduction of the large organic reagent into other pockets or interfaces of the crystal, reducing diffraction quality. Consequently It was important to harvest the crystal products at "the correct times" to ensure good X-ray diffraction data (see Table 3-2). In order to get good X-ray diffraction, the crystals needed to be large enough to diffract at a high resolution, and needed to withstand longer periods of time in arylhydrazine solutions. Each protein derivative was different. In the cases where the soaking time was longer than three days, the crystals were frequently washed with fresh arylhydrazine solutions to introduce fresh reagent to achieve complete reaction and to help remove any organic byproducts. I found that these are all very important factors in obtaining a good crystal structure of the Mb-aryl derivatives, and may explain why there aren't many of these such crystal structures reported in the literature [30, 31]. I note

that for each Mb-aryl structure reported in this chapter, I had to optimize the reaction conditions using >40 different trials.

Table 3-2. Soaking time (days) of different crystals with phenylhydrazine and derivatives

	Phenylhydrazine	3-methylphenylhydrazine	4-chlorophenylhydrazine
wt	3	-	-
H64A	2	2	14
H64Q (*P2$_1$*)	3	2	3
H64Q (*P6*)	10	11	-
V68A/I107Y	1	2	-

The dash lines indicate structures not obtained.

The pH values of each of the reaction solutions were the same as those used to crystallize their *met*Mb precursor crystals. For example, the H64Q crystals with the *P2$_1$* space group (obtained at pH 7.4) were soaked with the reaction solutions at pH 7.4. However, reactions of the H64Q crystals (*P6* space group) obtained at pH 9.0 were performed at this pH.

3.3.4 Crystallographic results of sw Mb-aryls

The X-ray diffraction data collection, data processing, and refinement statistics of 11 complex structures obtained are presented in (Table 3-3). Each of the complexes will be described in detail in the following sections.

Table 3-3. X-ray data collection and refinement statistics

	wt-phenyl	H64A-phenyl	H64A-tolyl	H64A -chlorolphenyl	H64Q-phenyl	H64Q-tolyl	H64Q -chlorophenyl
PDB code	5IKS		5ILE	5ILM		5ILP	5ILR
Data collection[a]							
Space group	$P2_1$	*P6*	*P6*	*P6*	$P2_1$	$P2_1$	$P2_1$
λ (Å)	1.54178	1.54178	1.54178	1.54178	1.54178	1.54178	1.54178
Cell dimensions	34.48 30.15 64.46 90.00 105.16 90.00	90.72 90.72 45.32 90.00 90.00 120.00	90.79 90.79 45.32 90.00 90.00 120.00	90.60 90.60 45.12 90.00 90.00 120.00	34.37 30.26 64.41 90.00 105.15 90.00	34.26 30.33 64.37 90.00 105.27 90.00	34.36 30.32 64.37 90.00 105.21 90.00
Resolution range (Å)	33.28 - 1.87	32.06 -1.76	39.26-1.77	39.11 -1.70	33.17 -1.76	33.00 -1.88	33.16 -1.87
Mean $I/\sigma(I)$	37.23 (3.68)	41.82 (6.28)	35.27 (4.58)	34.88 (3.72)	33.3 (3.31)	31.0 (8.00)	28.41 (3.00)
No. of reflections							
Observed	38144	126549	180821	213215	45203	39773	40428
Unique	10468 (473)	21272 (1058)	20927 (1024)	23456 (1160)	12946 (610)	10620 (536)	10786 (537)
Multiplicity	3.6 (3.0)	5.9 (3.5)	8.6 (5.1)	8.7 (4.8)	3.5 (2.0)	3.7 (3.1)	3.7 (3.0)
Completeness (%)	97.1 (92.2)	100 (100)	99.9 (98.9)	100 (100)	99.4 (92.6)	99.8 (99.1)	99.1 (98.2)
R_{merge}[b]	0.038 (0.313)	0.065 (0.221)	0.075 (0.489)	0.069 (0.486)	0.057 (0.257)	0.043 (0.128)	0.050 (0.218)
Refinement statistics							
No. of protein atoms	1203	1248	1238	1250	1208	1224	1225
R factor (%)[c]	0.213	0.149	0.153	0.152	0.188	0.150	0.163
R_{free} (%)[d]	0.278	0.187	0.179	0.192	0.234	0.199	0.214
rmsd bond distances	0.011	0.024	0.025	0.025	0.020	0.019	0.020
rmsd angles	1.631	2.170	2.196	2.418	2.016	2.036	2.031
B factor	20.19	22.28	21.59	17.41	28.64	20.62	20.38
Ramachandran plot (%)[e]							
Residues in most favored	97.32	98.09	98.06	98.09	96.67	98.03	97.39
Outliers	0.00	0.00	0.00	0.00	0.00	0.00	0.00

[a] Values in parentheses correspond to the highest resolution shells.

[b] $R_{merge}=\Sigma|I-\langle I\rangle|/\Sigma(I)$, where I is the individual intensity observation and $\langle I\rangle$ is the mean of all measurements of I.

[c] $R=\Sigma||F_o|-|F_c||/\Sigma|F_o|$, where F_o and F_c are the observed and calculated structural factors, respectively.

[d] R_{free} was calculated by using 5% of the randomly selected diffraction data which were excluded from the refinement.

[e] As calculated using *MOLPROBITY*.

Table 3-3. X-ray data collection and refinement statistics (Cont'd)

	H64Q-phenyl	H64Q-tolyl	V68A/I107Y -phenyl	V68A/I107Y -tolyl
PDB code				
Data collection[a]				
Space group	*P6*	*P6*	$P2_1$	$P2_1$
λ (Å)	1.54178	1.54178	1.54178	1.54178
Cell dimensions	90.64 90.64 45.29 90.00 90.00 120.00	90.69 90.69 45.27 90.00 90.00 120.00	34.59 30.15 64.37 90.00 105.45 90.00	34.64 30.17 64.49 90.00 105.23 90.00
Resolution range (Å)	26.16 -1.74	32.04 -1.77	31.02 -1.90	33.42 - 1.98
Mean $I/\sigma(I)$	19.5 (1.97)	35.64 (4.75)	14.58 (2.13)	22.93 (2.57)
No. of reflections				
Observed	141883	148423	27921	29630
Unique	21994 (1104)	20931 (1035)	10254 (492)	9077 (433)
Multiplicity	6.5 (5.9)	7.1 (6.4)	2.7 (2.4)	3.3 (3.2)
Completeness (%)	99.8 (100.0)	99.9 (100.0)	99.0 (96.3)	98.3 (93.5)
R_{merge}[b]	0.107 (0.903)	0.064 (0.427)	0.076 (0.435)	0.055 (0.456)
Refinement statistics				
No. of protein atoms	1238	1256	1219	1206
R factor (%)[c]	0.171	0.177	0.202	0.205
R_{free} (%)[d]	0.210	0.206	0.252	0.292
rmsd bond distances	0.022	0.018	0.018	0.010
rmsd angles	2.101	2.622	1.901	1.474
B factor	23.04	20.40	24.96	28.86
Ramachandran plot (%)[e]				
Residues in most favored	98.10	97.50	95.36	97.99
Outliers	0.00	0.00	0.00	0.00

[a] Values in parentheses correspond to the highest resolution shells.

[b] $R_{merge}=\Sigma|I-\langle I\rangle|/\Sigma(I)$, where I is the individual intensity observation and $\langle I\rangle$ is the mean of all measurements of I.

[c] $R=\Sigma||F_o|-|F_c||/\Sigma|F_o|$, where F_o and F_c are the observed and calculated structural factors, respectively.

[d] R_{free} was calculated by using 5% of the randomly selected diffraction data which were excluded from the refinement.

[e] As calculated using *MOLPROBITY*.

3.3.4.1 The structural characterization of wt sw Mb-phenyl derivative

The identity of the wt sw Mb-phenyl complex was confirmed by X-ray crystallography data at 1.87 Å resolution. To obtain the product, thin needle-like crystals of wt sw Mb were soaked with phenylhydrazine solution. As seen in Fig. 3-5A and Fig. 3-5B, the phenylhydrazine reagent has lost its “hydrazine” functional group, leaving the phenyl group to coordinate with the Fe center of heme in the distal pocket to form the Fe-carbon organometallic bond. The distance between Fe and the phenyl group (Fe-C bond) is 1.9 Å. On the opposite side of the Fe-C bond, the distance between the Fe and the proximal His93 (Fe-N) is 2.3 Å.

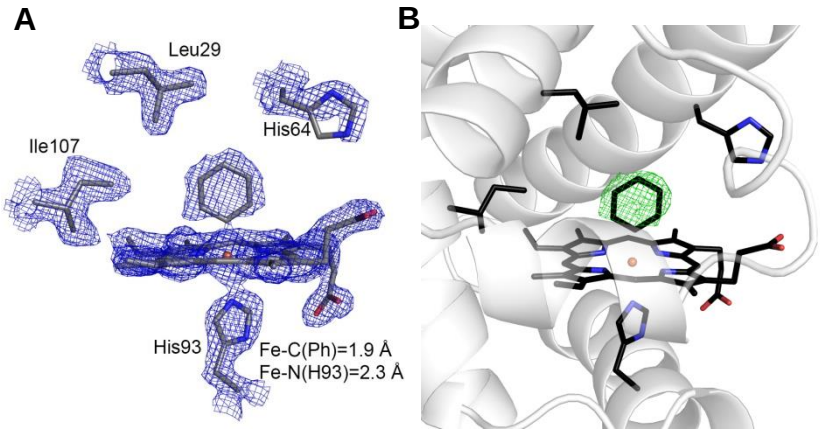

Fig. 3-5. Active site structures of the wt sw Mb-phenyl complex. A) the $2F_o$-F_c electron density map of the heme pocket in wt sw Mb-phenyl (contoured at 1 σ); B) the F_o-F_c omit electron density map and final model of an expanded heme site showing the new electron density of phenyl group (contoured at 3 σ).

In order to more clearly detail the active-site structures, the axial ligand tilts were defined as follows. “α” and “γ” define the angles between the normal of the heme 4N-plane and the Fe-C_{phenyl} or Fe-N_{His93} axis. “β” and ”θ” indicate how far the phenyl plane and the imidazole plane of His93 tilt from the Fe-C_{phenyl}

or Fe-N_{His93} axis. "ϕ" stands for the angle between the porphyrin (por)N_{22}-Fe-N_{24}(por) and the imidazole plane of His93 (or ∠N_p-Fe-N_{his}-C_{his}). "ω" represents the dihedral angle between the *trans* phenyl and imidazole planes.

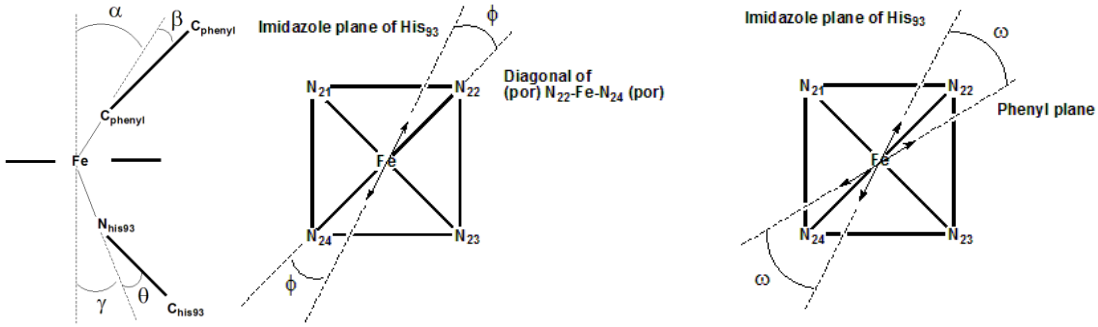

In the wt sw Mb-Ph structure, the (por)N_{22}-Fe-N_{24}(por) diagonal is essentially along the plane of the proximal His93 imidazole (ϕ=0.8º). The phenyl plane makes a 35º angle with the *trans* imidazole plane (Fig. 3-6A). Note that the phenyl group is tilted ~6º from the normal to the heme 4N-plane (Fig. 3-6B). Structural details for this complex and the other derivatives are listed in Table 3-4.

The phenyl group was modeled in the distal pocket at 100% occupancy. No hydrogen bonding interactions around the ligand were found.

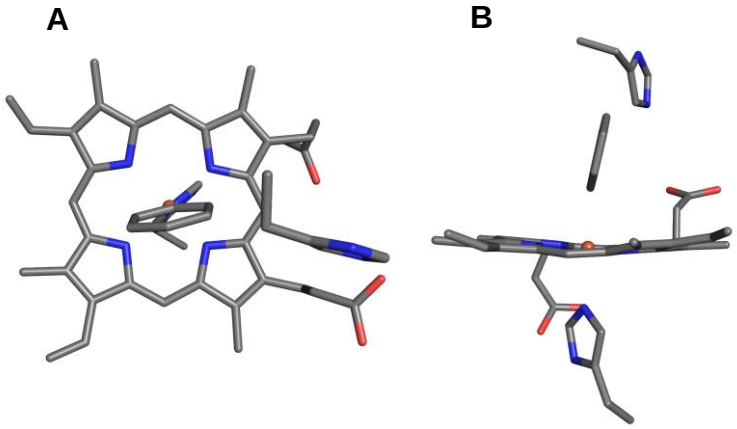

Fig. 3-6. Top (A) and side view (B) of the heme site in wt sw Mb-phenyl.

3.3.4.2 The structural characterization of sw Mb H64A-aryl derivatives

In order to obtain structural information of the product complexes, hexagonal prism-shaped crystals were soaked with the arylhydrazines: phenylhydrazine, 3-methylphenylhydrazine, and 4-chlorophenylhydrazine. All three crystal structures were obtained after numerous (>40 each) trials: H64A-phenyl, H64A-tolyl, and H64A-cholophenyl (Fig. 3-7). The crystal structures of the complexes are shown in Fig. 3-7, and the selected structural data including axial ligand tilts are shown in Table 3-4. Similar to that seen in the wt sw Mb-phenyl structure, the reaction of phenylhydrazine with ferric sw Mb H64A caused the removal of the hydrazine functional group, leaving the phenyl group to attach to Fe in the heme pocket (Fig. 3-7A, D). The substitution of the H64 by Ala did not alter the identity of the Fe-Ph reaction product. 3-methylphenylhydrazine and 4-chlorophenylhydrazine reacted with H64A similarly (Fig. 3-7B, C, E, F). These two reactions also resulted in the cleavage of the hydrazine groups.

The methyl moiety of the tolyl group in the H64A-tolyl structure is oriented towards the hydrophobic interior of the protein. The chloride atom of the chlorophenyl group in the H64A-chlorophenyl structure still points up in this 4-position, which is almost perpendicular to the heme plane. The arrangement of the tolyl and cholophenyl groups in our structures confirms that it is the carbon atom which was previously bound to the hydrazine functional group coordinates with Fe to form the Fe-C bond. No hydrogen bonds around the aryl ligands in these three complexes were found.

It is interesting to point out that H64A-chlorophenyl has relatively bigger α and β angles due to the “distorted” orientation of the chlorophenyl ligand in the pocket (see Discussion section).

Two of the structures, namely H64A-phenyl and H64A-tolyl, were obtained after two-days of soaking. The ligands in these two structures were modeled very well with full occupancy (Fig. 3-7A, B, D, E). Some issues were encountered, however, when pursuing the structure of the sw Mb H64A-chlorophenyl complex. Many of the “successful” crystal structures obtained during the soaking trials had the chlorophenyl ligands sitting in the pocket nicely. However, if the ligand soaking time was insufficient, then the resulting chlorophenyl ligand displayed disconnection in the election density between the chloride atom and the phenyl group. The final structure with 80% occupancy of the chlorophenyl ligand was obtained after soaking for 14 days, making sure to expose the reaction crystals to the fresh 4-chlorophenylhydrazine solution every 2-3 days.

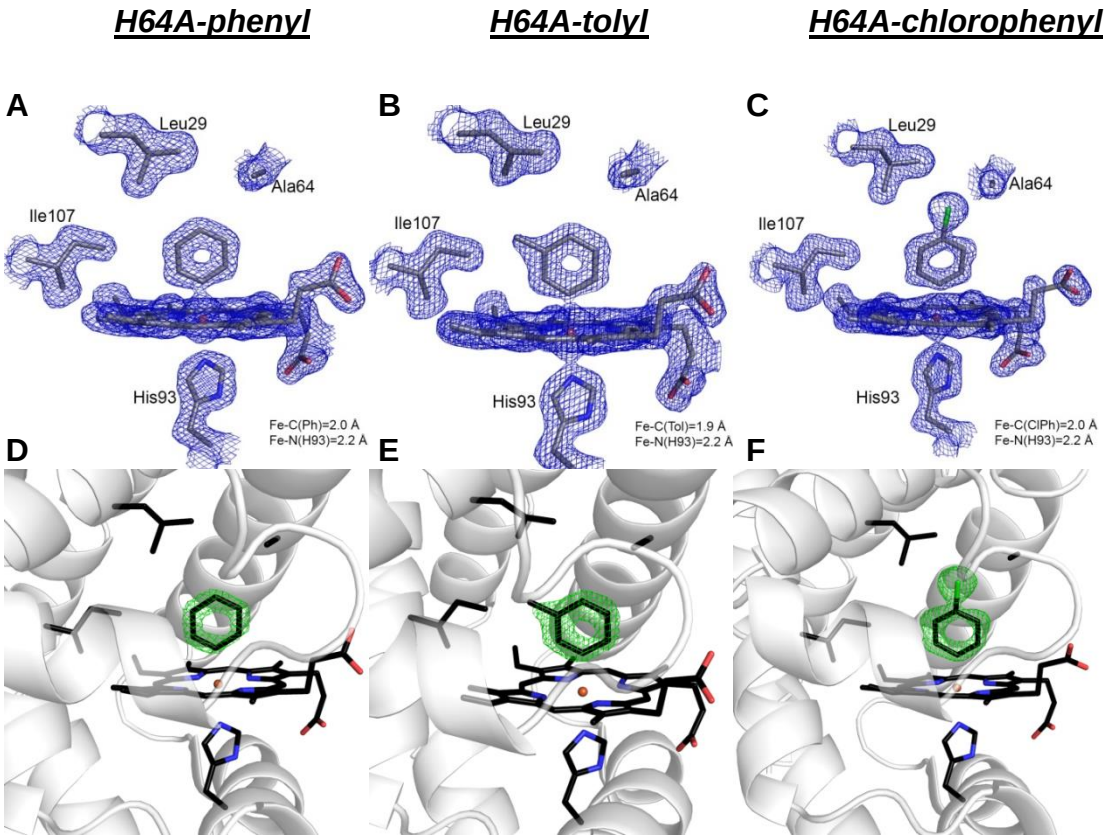

Fig. 3-7. Active site structures of the sw Mb H64A-aryl complexes. A-C) the $2F_o$-F_c electron density map of the heme pocket in sw Mb H64A-aryls (contoured at 1 σ); D-F) the F_o-F_c omit electron density map and final model of an expanded heme site showing the new electron density of phenyl group (contoured at 3, 2.5, and 2.5 σ, respectively).

Table 3-4. Selected structural parameters of the Mb-aryl derivatives

	Occupancy of aryl	Fe-C (Å)	Fe-N(H93) (Å)	α (º)	β (º)	γ (º)	θ (º)	ϕ (º)	ω (º)
wt-phenyl (*P2$_1$*)	1	1.9	2.3	6.4	0.1	3.5	2.3	0.8	34.7
H64A-phenyl (*P6*)	1	2.0	2.2	4.0	2.6	1.5	1.6	3.6	26.4
H64A-tolyl (*P6*)	1	1.9	2.2	2.0	4.1	1.4	4.1	2.0	26.4
H64A-chlorophenyl (*P6*)	0.8	2.0	2.2	9.4	8.5	2.8	4.2	0.7	43.5
H64Q-phenyl (*P2$_1$*)	1	2.0	2.3	4.9	1.4	1.4	4.0	1.7	35.3
H64Q-tolyl (*P2$_1$*)	1	1.9	2.3	4.9	3.9	4.2	0.4	2.0	28.8
H64Q-chlorophenyl (*P2$_1$*)	1	2.0	2.3	5.2	2.0	0.4	4.6	2.1	40.1
H64Q-phenyl (*P6*)	0.8	2.1	2.2	6.1	0.0	3.1	0.6	3.2	23.9
H64Q-tolyl (*P6*)	0.6	2.0	2.3	7.6	1.8	8.9	14.0	8.5	15.5
V68A/I107Y-phenyl (*P2$_1$*)	1	2.1	2.2	2.3	1.3	3.1	0.3	4.2	44.7
V68A/I107Y-tolyl (*P2$_1$*)	1	2.0	2.3	3.3	0.1	3.9	10.2	2.1	46.3

3.3.4.3 The structural characterization of sw Mb H64Q-aryl derivatives

As noted earlier, ferric sw Mb H64Q can be crystallized either at pH 7.4 or pH 9.0 (2.56-3.2 M of AS, 100 mM Tris•HCl, 1mM EDTA) with two different space groups, $P2_1$ (relatively longer hexagonal prisms) or *P6* (the hexagonal prism) respectively. Three crystalline derivatives were obtained from $P2_1$ space group (H64Q-phenyl ($P2_1$), -tolyl ($P2_1$) and -chlorophenyl ($P2_1$)) and two complexes from the *P6* space group (H64Q-phenyl (*P6*), -tolyl (*P6*)). I found that the crystals belonging to the *P6* space group were relatively more difficult to react with arylhydrazines, and needed longer soaking times to generate the product complexes.

sw Mb H64Q-aryl derivatives in the $P2_1$ space group

With a mutation from His to Glu at the 64th residue position, the products that result from the reaction between ferric H64Q and the three arylhydrazines (phenylhydrazine, 3-methylphenylhydrazine, and 4-chlorophenylhydrazine) contain similar Fe-aryl linkages as observed with the wt and H64A mutant (Fig. 3-8). The three resulting complexes are H64Q-phenyl ($P2_1$), H64Q-tolyl ($P2_1$) and H64Q-chlorophenyl ($P2_1$), and the carbon initially connected with the hydrazine groups in the arylhydrazines remains the carbon that is coordinated with Fe in the Mb-aryl products. The three distal pockets from the complexes show no hydrogen bonds around the ligands. The ligands in the three complex structures were modeled with full occupancy (Fig. 3-8).

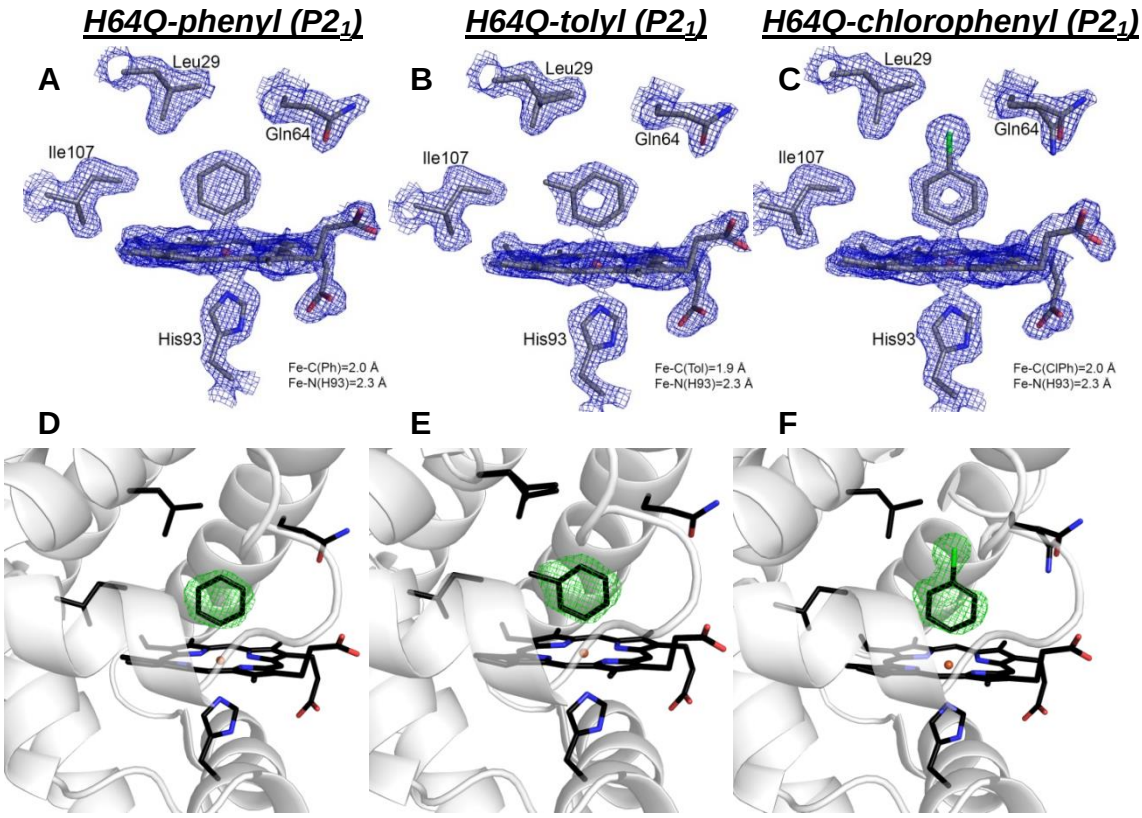

Fig. 3-8. Active site structures of the sw Mb H64Q-aryl complexes in $P2_1$ space group. A-C) the $2F_o$-F_c electron density map of the heme pocket in sw Mb H64Q-aryls (contoured at 1 σ); D-F) the F_o-F_c omit electron density map and final model of an expanded heme site showing the new electron density of phenyl group (contoured at 3 σ).

sw Mb H64Q-aryl derivatives in the P6 space group

The active site structures of the H64Q Mb products in the *P6* space group are similar to those in the $P2_1$ space group (Fig. 3-9). The reactions between the Mb H64Q *met* crystals and the arylhydrazines took longer than most of the other reactions. Two products were obtained, H64Q-phenyl (*P6*) and H64Q-tolyl (*P6*), after soaking the *met*Mb crystals with the arylhydrazine reagents for 10 days and 11 days respectively (Table 3-2). Even after this extended soaking time, the phenyl and tolyl groups still could not be modeled

with full occupancy, but were modeled with 80% and 60% occupancies, respectively (Fig. 3-9A-B).

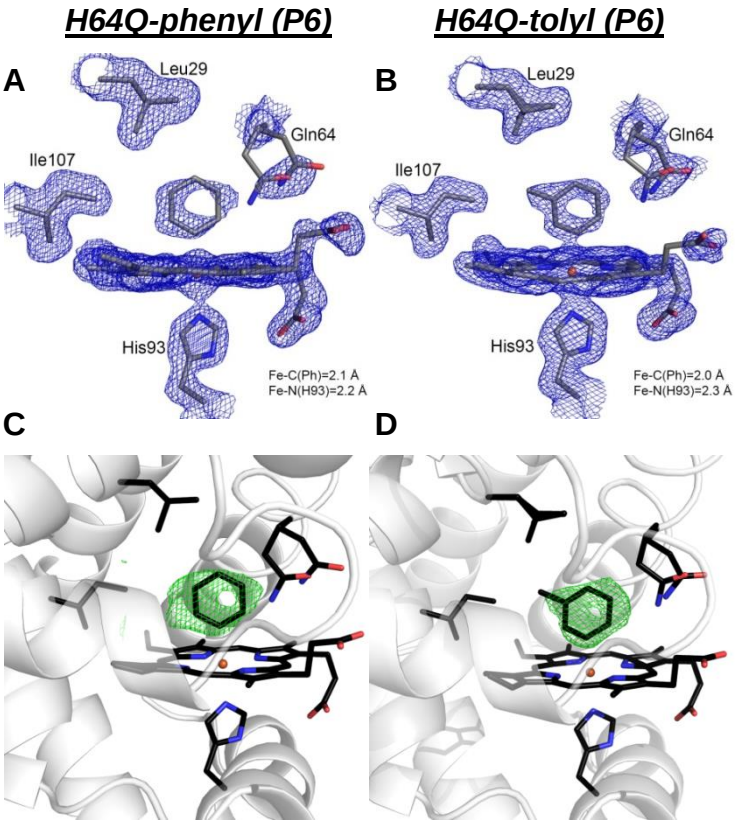

Fig. 3-9. Active site structures of the sw Mb H64Q-aryl complex in the *P6* space group. A-B) the $2F_o$-F_c electron density map of the heme pocket in sw Mb H64Q-aryl (contoured at 1 and 0.8 σ respectively); C-D) the F_o-F_c omit electron density map and final model of an expanded heme site showing the new electron density of phenyl group (contoured at 2.6 and 3 σ respectively).

Attempts to model the Gln64 residue in only one orientation yielded positive/negative density in the F_o-F_c map. In the H64Q-phenyl (*P6*) structure, Gln64 was modeled with two alternative conformations (20% and 80% occupancy). The Gln64 sidechain with 20% occupancy superimposed nicely with Gln64 in the *met* form of H64Q (Fig. 3-15D). Gln64 in H64Q-tolyl (*P6*) was modeled in two alternative conformations as well, but with 50% occupancy each.

3.3.4.4 The structural characterization of sw Mb V68A/I107Y-aryl derivatives

To obtain the X-ray crystal structures of the products, the thin crystals of V68A/I107Y were soaked with arylhydrazine solutions. I observed that the crystals could only withstand up to two days in the arylhydrazine solutions before the resulting crystals would no longer diffract. Eventually, two product structures were obtained, V68A/I107Y-phenyl and V68A/I107Y-tolyl (Fig. 3-10). The phenyl and tolyl groups were modeled at full occupancy. The electron density around the phenyl and tolyl groups was not as prominent, so both of the F_o-F_c omit maps were contoured at 2.5 σ (Fig. 3-10C and D).

In the case of the V68A/I107Y-tolyl structure, and as a result of the steric effect from Tyr107, the orientation of the tolyl group points to the hydrophilic solvent exterior rather than the hydrophobic interior (see Discussion section).

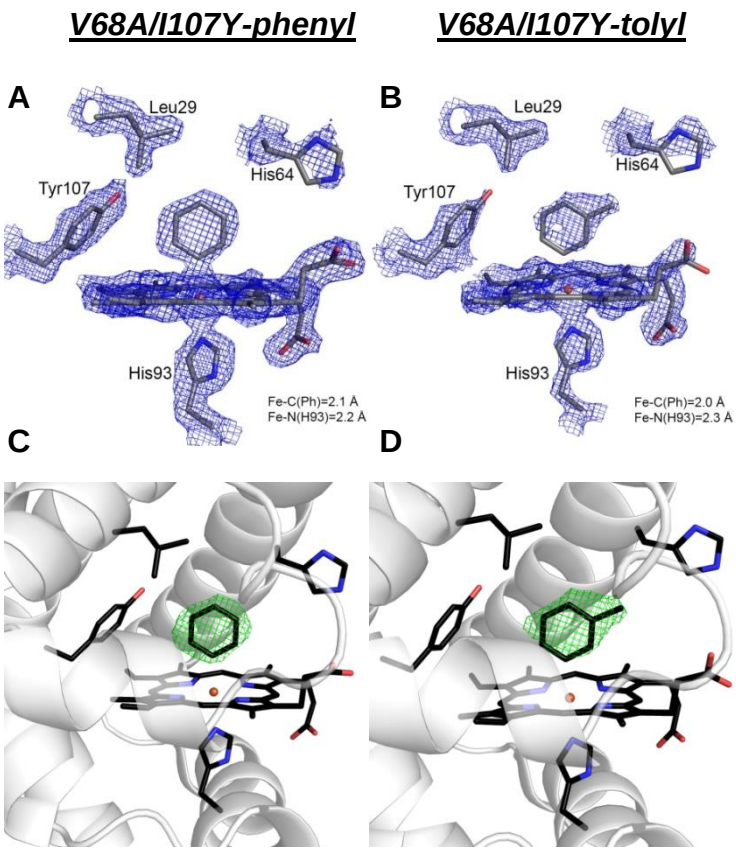

Fig. 3-10. Active site structures of the sw Mb V68A/I107Y-aryl complexes. A-B) the $2F_o$-F_c electron density map of the heme pocket in sw Mb V68A/I107Y-aryls (contoured at 1 σ); C-D) the F_o-F_c omit electron density map and final model of an expanded heme site showing the new electron density of phenyl group (contoured at 2.5 σ).

3.4 Discussion

3.4.1 Formation of sw Mb-aryl complexes as monitored by UV-vis spectroscopy

The appearance of a new band at ~433 nm in the UV-vis spectra during the reactions of sw Mb and arylhydrazines matches that previously reported for the MbFe(III)-phenyl complex [28, 29]. We do notice that the absorbance intensity at 430 nm for the Mb-aryl derivatives is much lower than the absorbance intensity of the starting *met* form at ~408 nm. The reduction in intensity is probably caused by likely change in extinction coefficient of the products and the destruction of the heme due to the formation of free radicals and H_2O_2 from these reactions. This reduction in absorbance intensity was also observed in the reactions of another heme containing protein, prostaglandin H synthase (PGHS), with hydrazines [32].

I found that after completion of the reaction, the Mb-aryl products are stable in air for at least four days. For example, as shown in Fig. 3-11A, the wt-phenyl product in solution still retained its λ_{max} at 433 nm after four days. This result also matches the UV-vis spectral data using dissolved crystals of sw Mb wt-phenyl (Fig. 3-11B). The crystals of wt Mb-phenyl complex (confirmed by X-ray crystallography) were left in reaction solution for 5 days, and then the product crystals were dissolved in phosphate buffer to obtain the UV-vis spectrum. A clear absorbance at 434 nm was still observed (Fig. 3-11).

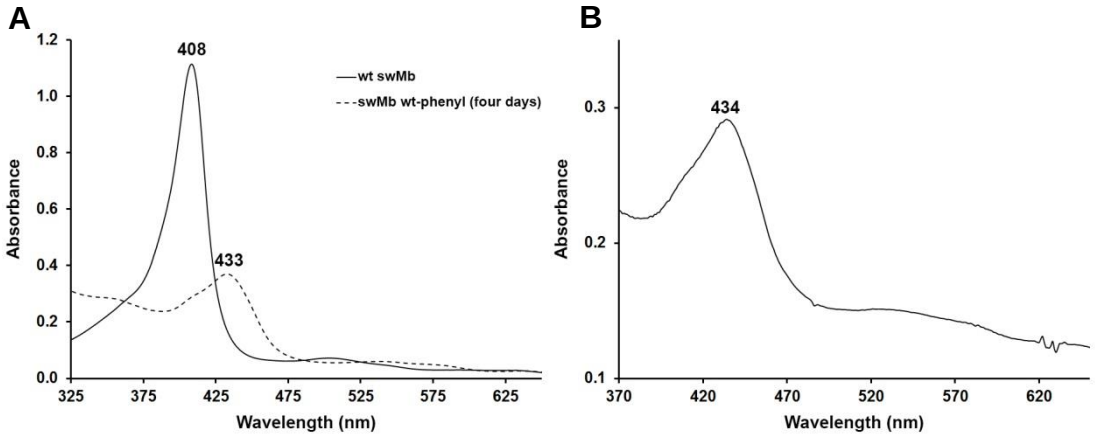

Fig. 3-11. Stability of sw Mb wt-phenyl from the reaction solution (A) and using dissolved crystals of the product (B). The band at ~433 nm does not change in intensity even after 4 days.

3.4.2 Heme is the determining factor in the reaction of sw Mb with arylhydrazines

Phenylhydrazine and its derivatives react with wt Mb and the three mutants to form similar products in these three proteins. The reactions cause the cleavage of hydrazine moieties, and the subsequent coordination between the heme Fe and the carbon atom that was originally connected with the hydrazine moiety (middle of Fig. 3-12). Consequently, the reactions of the hydrazine compounds with sw Mb result in the formation of the sw Mb-phenyl, sw Mb-tolyl and sw Mb-chlorophenyl complexes. The identities of the Fe-aryl reaction products did not change with mutation of the residues in the distal pocket and the different crystal packing forms. This indicates that the heme (and not the distal pocket residues) is most likely the determining factor in these reactions.

It has been reported that isolation of the heme-phenyl moiety from the protein, using strong acid and air, caused the formation of four N-phenylprotoporphyrin IX regioisomers characterized by an identical Soret band at 412 nm in $CHCl_3$ [28]. The zinc complexed N-phenylprotoporphyrin IX isomers in $CHCl_3$ displayed similar spectra with non-identical Soret bands: 440 nm for isomer I and II; 442 nm for isomer III; 444 nm for isomer IV [28, 33].

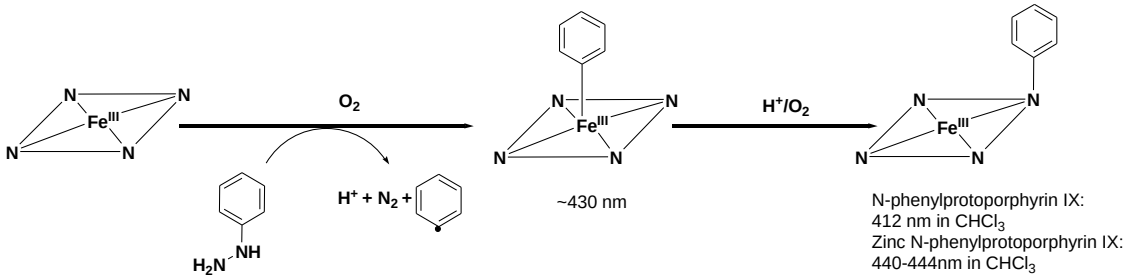

Fig. 3-12. Proposed reaction mechanism of sw Mb and arylhydrazines [28, 33-35]. Only the heme site is shown.

3.4.3 Conformational changes occur for residues in the distal pocket

The exact identity of the residues in the heme distal pocket does not appear to alter the product formation, but they can alter other factors involved in these reactions such as the reaction rate. As compared to the respective met precursors, the structures of the Mb-aryl products have a similar overall structure with RMSD of ~0.2 Å, and the only significant changes occured in the active site. In order to accommodate the aryl ligands bound with heme iron, some distal pocket residues need to change their conformations considerably. This was observed through comparisons between the sw Mb *met* form structures [36, 37] (some of them were reproduced in this work and used as

controls) and the product structures obtained after the ligands were introduced (Fig. 3-13).

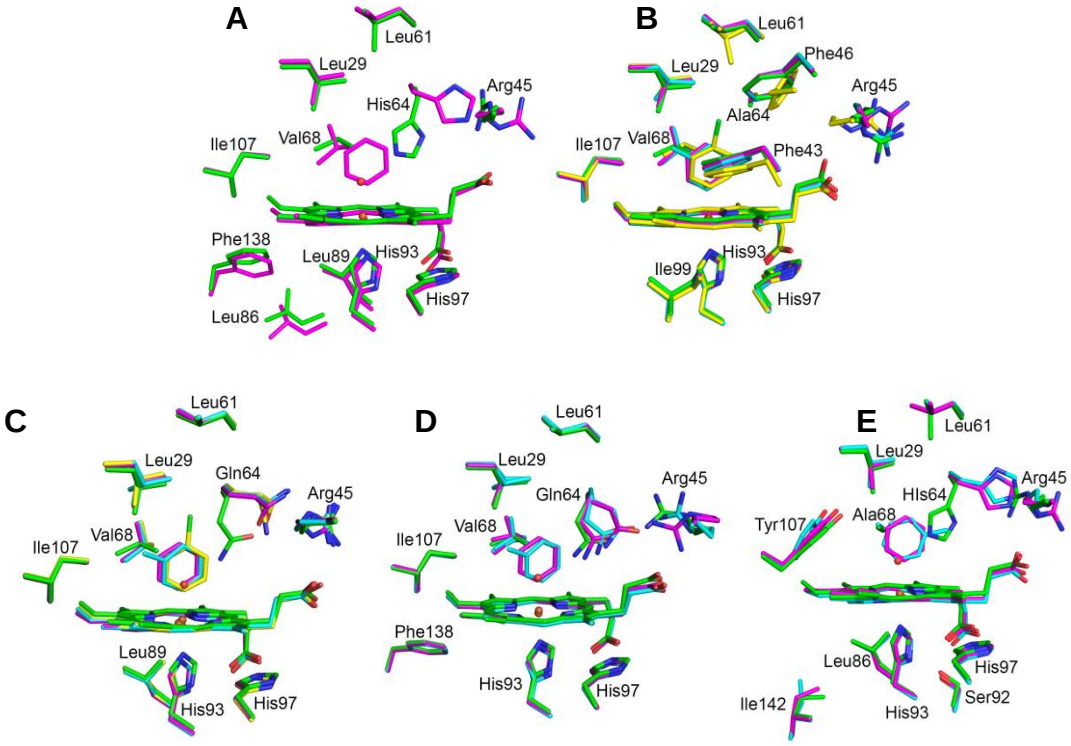

Fig. 3-13. Comparisons of the heme pockets from each sw Mb derivatives. A) alignment of wt-H_2O (*met* form) and wt-phenyl; B) alignment of H64A-H_2O, H64A-phenyl, H64A-tolyl and H64A-chlorophenyl; C) alignment of H64Q-H_2O, H64Q-phenyl, H64Q-tolyl, and H64Q-chlorophenyl in $P2_1$ space group; D) alignment of H64Q-H_2O, H64Q-phenyl, and H64Q-tolyl in *P6* space group; E) alignment of V68A/I107Y-H_2O, V68A/I107Y-phenyl, and V68A/I107Y-tolyl. Note: green represents the *met* forms, magenta for the complexes with phenyl, cyan for the ones with tolyl, and yellow for the ones with chlorophenyl.

The residue His64 in wt (Fig. 3-13A) and V68A/I107Y (Fig. 3-13E), and the Gln64 in H64Q (Fig. 3-13C, D) fully or partially alter their inward orientations (initially pointing towards the heme in the distal pocket) to an orientation pointing to the protein exterior with flip angles ~90º. Accordingly, accompanying

the changes in His64 (Fig. 3-13A, E) or Gln64 (Fig. 3-13C, D), the Arg45 residues also changed from “inward” to “outward” orientations in several of structures. The “outward” orientations of H64/Q64 and Arg45 appear to create an open entry to accept the ligands (Fig. 3-13A, C-E). For example, the active-site volumes of wt-H_2O and wt-phenyl, calculated by the program *Hollow*, illustrate the contour of the pores (Fig. 3-14) [38]. The interior surface around the distal pocket was computed using dummy atoms as probes with a radius of 1.4 Å (close to the size of a water molecule). Before any ligands are introduced to wt-H_2O, the cavity (purple) is essentially a closed environment (Fig. 3-14A). After the phenyl group coordinates to Fe in the pocket, and due to the orientation changes of two residues, His64 and Arg45, the cavity opens up (its gate) to accommodate the phenyl group shown in black (inside of the cavity, Fig. 3-14B).

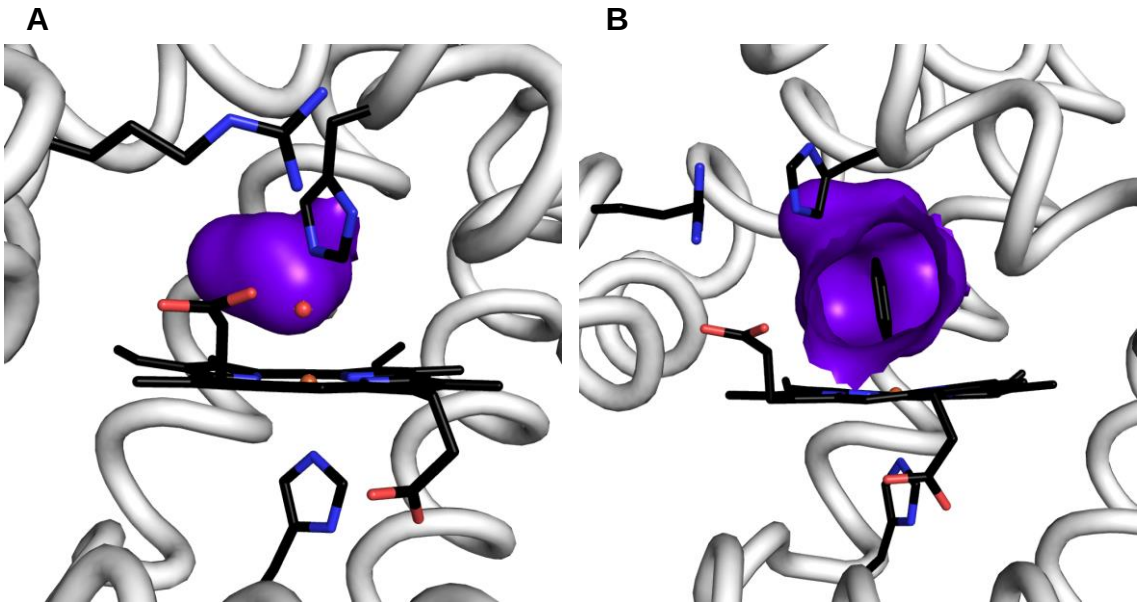

Fig. 3-14. The active-site cavities in wt-H_2O and wt-phenyl. A) a close “mouth” in wt-H_2O, B) an open “mouth” in wt-phenyl.

As described earlier, in H64Q-phenyl (*P6*) and H64Q-tolyl (*P6*), the phenyl and tolyl groups were modeled at 80% and 60% occupancies respectively. The relatively lower electron densities around the ligands (see Fig. 3-9) suggest incomplete reactions. The comparison of the H64Q product structure in the *P6* space group provides structural evidence for the incomplete reactions (Fig. 3-13D). The electron densities of the Arg45 sidechains in all the H64Q structures (*P6*) are not strong enough to determine the precise position of this residue. However, the best modeled positions suggest that Arg45 prefers the inward orientation which does not normally favor ligand binding. This helps explain why the arylhydrazines did not react with these heme proteins to completion.

In most cases, Val68 flipped its orientation from horizontal to vertical (Fig. 3-15), except in the H64A-chlorophenyl structure. Since the chlorophenyl group is further away from Val68 and tilted toward Phe43 to form a 73^{o} angle with the heme plane (Fig. 3-15B and Fig. 3-13B), it is perhaps not necessary for Val68 to flip. The alternative conformations were modeled for the Val68 sidechains in the H64Q (*P6*) structures, e.g. H64Q-phenyl (*P6*) and H64Q-tolyl (*P6*). The Val68 in these two structures seem to prefer the vertical orientation. Since the reactions were not fully complete, the horizontal conformations are not completely switched to the vertical positions. This is perhaps also the reason why Gln64 in these two complexes was best modeled in two conformations (Fig. 3-15D).

The isopropyl of the Leu61 residue at the “top position” in the distal pocket tends to be “horizontal” when ligands bind with iron. Thus, the isopropyl of Leu61 is “vertical” in sw Mb-H_2O, but switches to the “horizontal” orientation after a ligand enters into the pocket. This is seen in the wt-phenyl (Fig. 3-15A), V68A/I107Y-phenyl (Fig. 3-15E) and V68A/I107Y-tolyl (Fig. 3-15E) structures. Alternatively if the isopropyl of Leu61 in sw Mb-H_2O is already the horizontal conformation, it will retain this position after the ligand enters into the pocket. This is exactly what is seen in the H64A-phenyl (Fig. 3-15B), H64A-tolyl (Fig. 3-15B), the three H64Q-aryl structures in the $P2_1$ space group (Fig. 3-15C), H64Q-phenyl (*P6*) (Fig. 3-15D), H64Q–tolyl (*P6*) (Fig. 3-15D), and H64A-chlorophenyl (Fig. 3-15B; the latter just partially changes to the vertical conformation, and gives two alternative conformations in the isopropyl of Leu61 due to the steric effect of chloride).

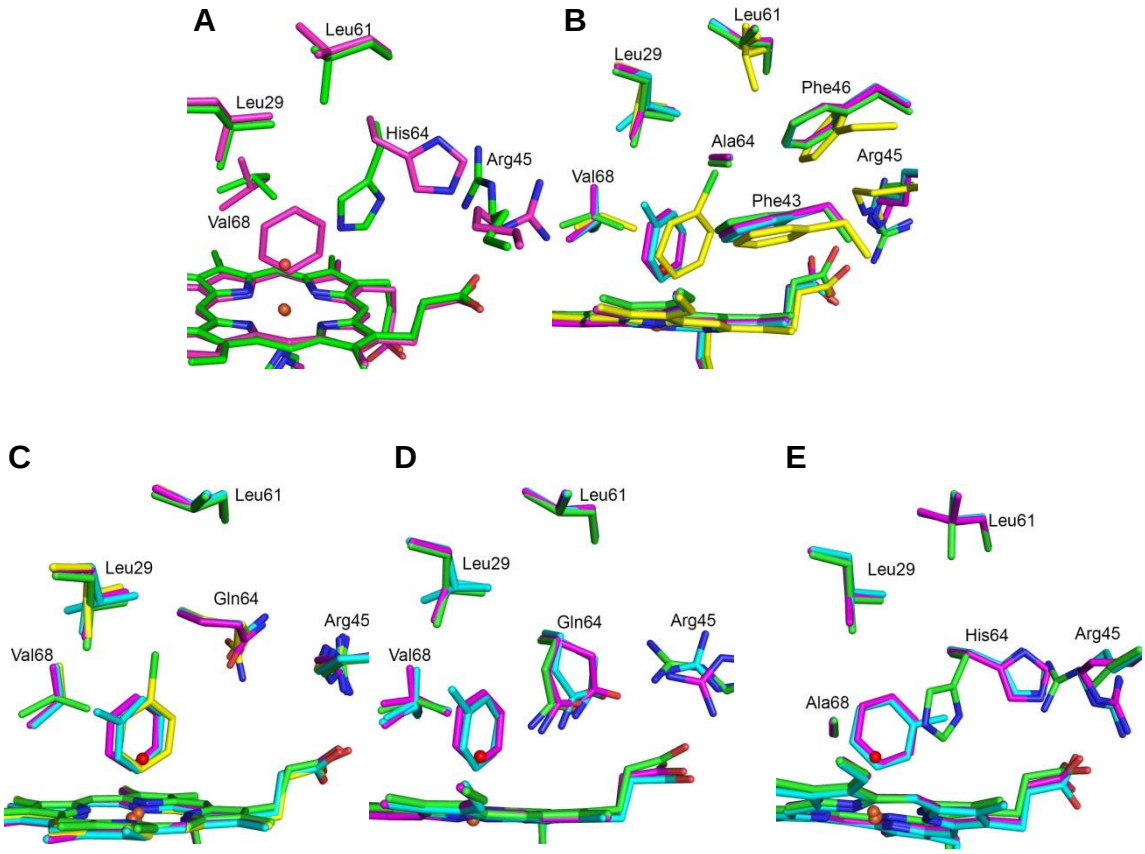

Fig. 3-15. Closer views of the active site environments in the sw Mb precusors and derivatives (zoomed-in from Fig. 3-13). A) wt; B) H64A; C) H64Q ($P2_1$); D) H64Q (*P6*); E) V68A/I107Y. Note: green stands for the *met* forms, magenta for the complexes with phenyl, cyan for the ones with tolyl, and yellow for the ones with chlorophenyl.

The isopropyl group of Leu29 is in the vertical conformation for most of the complexes (wt, H64A and V68A/I107Y); however, the Leu29 in H64Q-tolyl ($P2_1$) and H64Q-tolyl (*P6*) has two conformations, vertical and horizontal, modeled at 50% occupancy each (Fig. 3-15C, D). This may be due to the steric effect from the methyl group of the tolyl moiety.

It is interesting to point out that among the above residues that showed conformational changes of the sidechains (except Arg45 which is in the CD loop of Mb) Leu61, Val68 and His64/Gln64 are all located in the E helix which shows a more important role in this work than previously thought in the interactions with similar ligands.

Some uncommon conformational changes were also observed in this work. A significant movement of the CD loop was observed in the H64A-chlorophenyl structure. The entire CD loop moves down and outward when compared with the other structures (Fig. 3-16). Such a conformational change was not readily observed in the other structures.

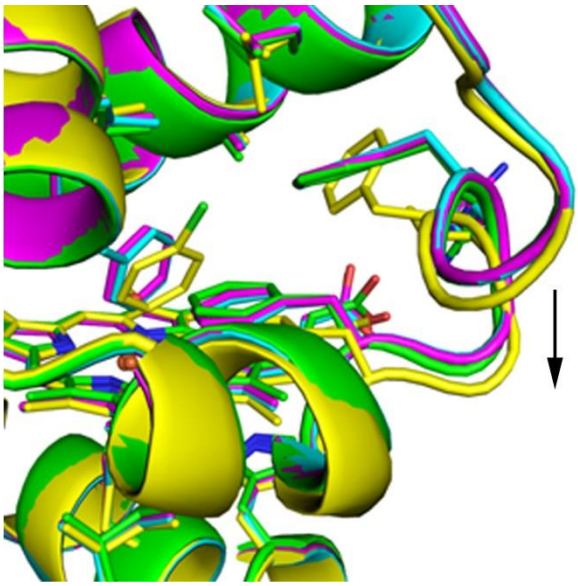

Fig. 3-16. Alignment of the four H64A structures: H64A-H_2O (green), H64A-phenyl (magenta), H64A-tolyl (cyan) and H64A-chlorophenyl (yellow). The arrow indicates the "downward" movement of the CD loop in H64A-chlorophenyl.

I also observed that the phenyl group of the Phe46 residue in the H64A-chlorophenyl product is rotated by ~45^o relative to its position in the H64A-H_2O,

and switched its original inward orientation (pointing towards the heme in the distal pocket) to an orientation towards the protein exterior (Fig. 3-13B). The position change of Phe46 is interesting because it was initially thought to be relatively stable, according to our structural data from the sw Mb complex with NOx ligands (see Chapter 2). In the sw Mb-NOx structures in Chapter 2, the conformational change of Phe46 is not due to the binding of the NOx species, and is only related to the mutations of the other residues in the distal pocket. The example of H64A-chlorophenyl here showed us that ligands other than NOx species can induce changes in Phe46 orientation (Fig. 3-13B). The sidechain of Ile142 in V68A/I107Y-phenyl and V68A/I107Y-tolyl also unexpectedly changed their conformations, unlike that observed in V68A/I107Y-H_2O. Specifically, in the V68A/I107Y-tolyl structure, the methyl group of Ile142 switched its orientation to the reverse orientation (Fig. 3-13E).

3.4.4 A "down shift" was observed for the heme and the proximal residues

The heme and the proximal residues in most of the structures all experienced a small "down shift" of their positions, when compared with their positions in the sw Mb-H_2O precursors. For example, if we zoom into the proximal pocket in Fig. 3-13A as redisplayed in Fig. 3-17, the proximal residues of wt-phenyl in this figure move down by ~0.5 Å as compared with the wt-H_2O. Most of these residues are located in the F helix in Mb.

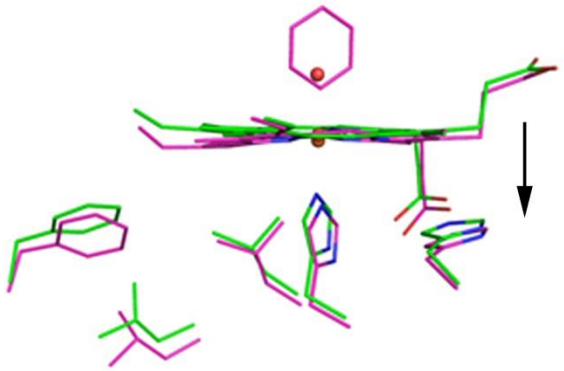

Fig. 3-17. Comparison of proximal pockets of wt-H_2O (green) and wt-phenyl (magenta). The arrow shows the down shift.

An exception to this is the H64A-chlorophenyl derivative. As mentioned earlier, the chlorophenyl ligand in H64A-chlorophenyl tilts away from the normal to the heme plane and forms an 80^o angle with the heme plane, which in turn pushes one side of the heme down (right side of Fig. 3-18) and the other side up (left side of Fig. 3-18). Consequently, half of the proximal residues do experience a down shift (right side of Fig. 3-18) and half of them experience a slight upshift.

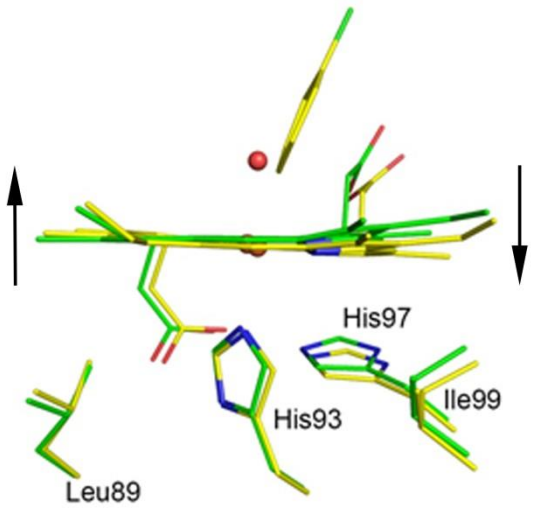

Fig. 3-18. Comparison of proximal pockets of H64A-H_2O (green) and H64A-chlorophenyl (yellow).

3.4.5 Crystal packing mode can affect the active site conformation

Crystals of sw Mb can be grown either in *P2₁* or *P6* space groups. I find that the crystal packing mode can also affect the active site conformation in the structures. The differences are shown in Fig. 3-19.

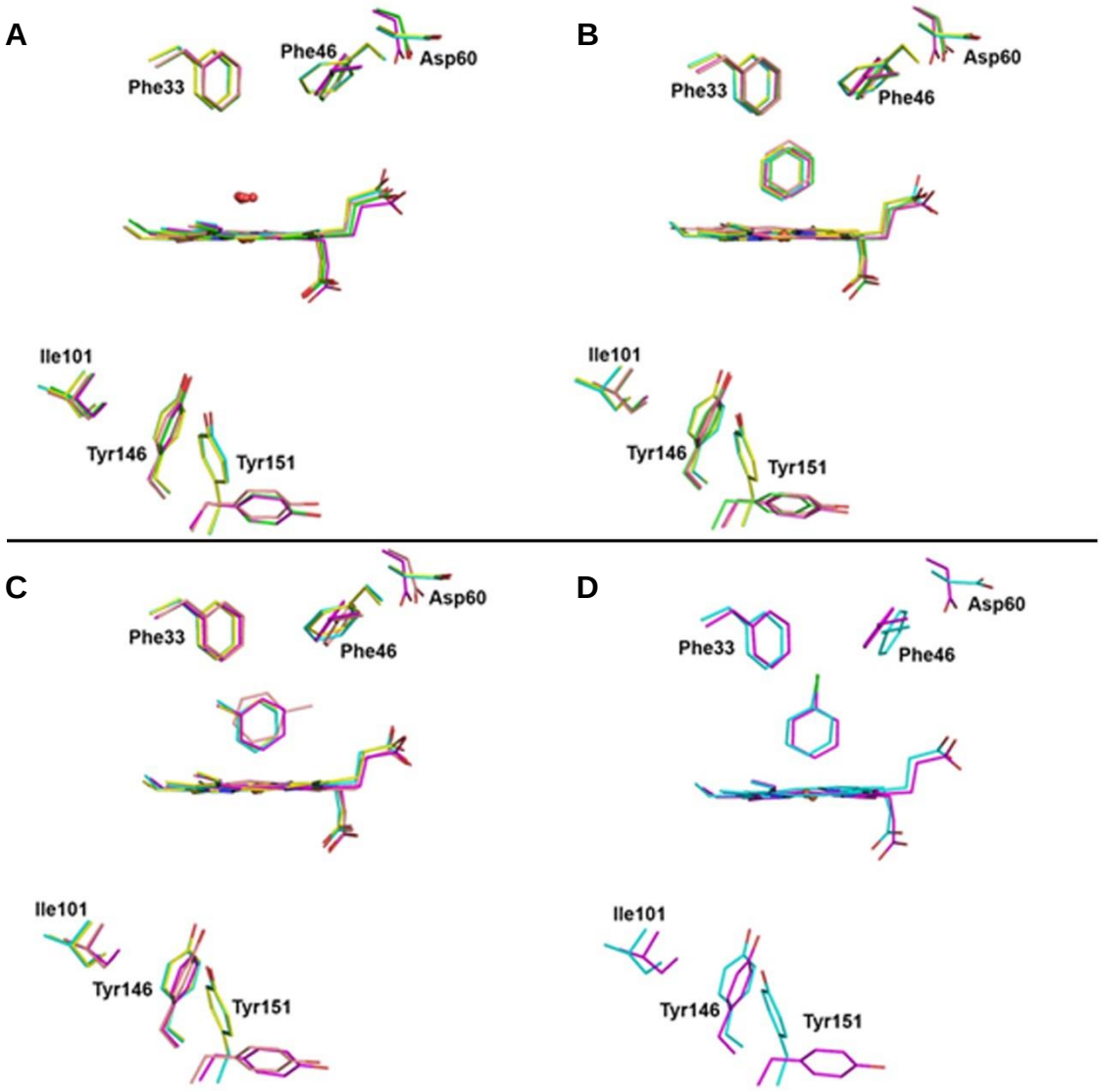

Fig. 3-19. Superimposition of the sw Mb derivatives. A) five structures sw Mb-H_2O; B) five structures sw Mb-phenyl; C) four structures sw Mb-tolyl; D) two structures of sw Mb-chlorophenyl. Each sw Mb structure is labeled by a different color; green (wt (*P2₁*)), cyan (H64A (*P6*)), magenta (H64Q (*P2₁*)), yellow (H64Q (*P6*)), and salmon (V68A/I107Y (*P2₁*)).

The proteins with the same ligands were aligned using their Cα chains. Differences among each set of the structural alignments with the same ligands appear to be mostly caused by the conformational changes associated with the space groups (*$P2_1$*/*P6*) and not by the mutations. Previous results showed that the structures of wt sw Mb in both *$P2_1$* and *P6* space groups are essentially identical, and the major differences were observed only in the sidechains on the protein surface [39, 40]. However, our results show differences not only in the sidechains of the surface residues, but also the interior residues. Selected residues are shown in Fig. 3-19. The residues from H64A *P6* (cyan) and H64Q *P6* (yellow) are all grouped together and slightly shift from *$P2_1$* space group residues (especially the residues shown in Fig. 3-19). An enlarged proximal pocket of Fig. 3-19B for the sw Mb-Ph complex is shown below (Fig. 3-20). All residues in this figure are grouped into two different conformations by colors: the cyan and yellow represent the structures in the *P6* space group; the other three represent those in the *$P2_1$* space group.

The alignment of complexes with chlorophenyl in Fig. 3-19D uses only two structures (H64A-chlorophenyl and H64Q-chlorophenyl (P*2_1*)), but the differences are similar to those shown in Fig. 3-19A-C.

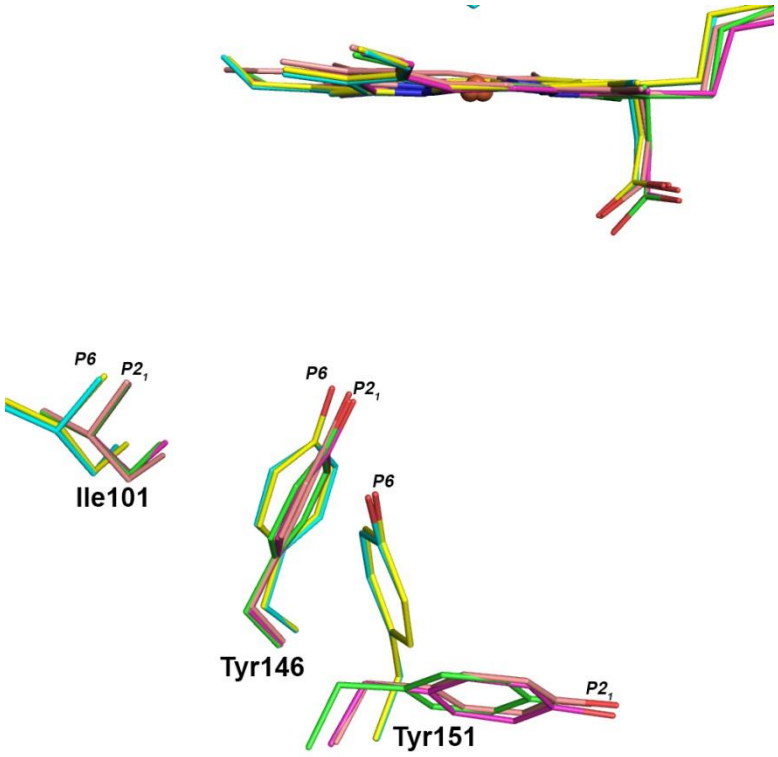

Fig. 3-20. Closer views of the proximal pocket in the sw Mb-Ph derivatives (Zoomed-in from Fig. 3-15B). Each of sw Mb is labeled with different color; green (wt (*P2₁*)), cyan (H64A (*P6*)), magenta (H64Q (*P2₁*)), yellow (H64Q (*P6*)), and salmon (V68A/I107Y (*P2₁*)).

The difference between the *aqua-met* form and complexes discussed above is the function of the two different space groups. For example, after phenyl coordinates to Fe, the isopropyl group of Leu61 either (i) switches from a vertical (Fig. 3-21A) to a horizontal position (Fig. 3-21B) as seen in wt (green) and V68A/I107Y (salmon) or (ii) keeps its horizontal position in H64A (*P6*) (cyan), H64Q (*P2₁*) (magenta) and H64Q (*P6*) (yellow). With this ligand binding, the Leu61 residues in two different groups tend to group together and slightly shift towards each other within two groups no matter how the sidechains change (see the Cα and isopropyl group of Leu61 in Fig. 3-21). This was also observed with other residues such as His/Gln 64 in Fig. 3-21.

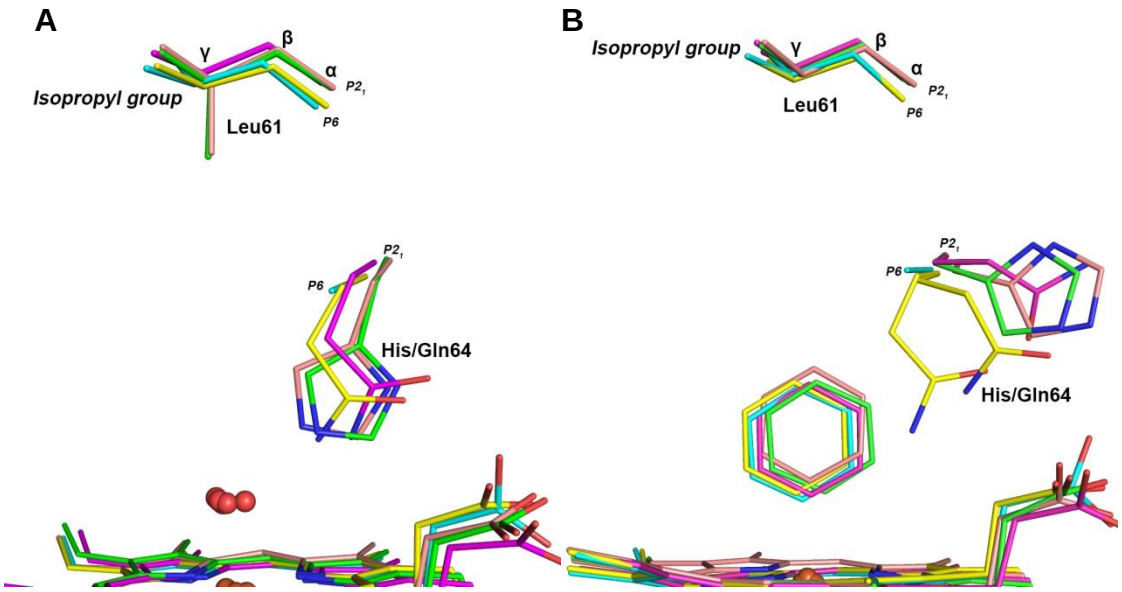

Fig. 3-21. Changes resulting from ligand binding as a function of the two different space groups. A) five structures of sw Mb-H_2O; B) five structures of sw Mb-phenyl. Each of sw Mb is labeled by a different color; green (wt (*P2₁*)), cyan (H64A (*P6*)), magenta (H64Q (*P2₁*)), yellow (H64Q (*P6*)), and salmon (V68A/I107Y (*P2₁*)).

As noted earlier, H64Q can crystallize at pH 7.4 or pH 9 in the *P2₁* and *P6* space groups, respectively. This mutant protein thus provided a very nice control when performing the soaking experiments. The crystals in the *P2₁* space group react much faster than the crystals in the *P6* space group. The H64Q-phenyl and H64-tolyl structures in the *P6* space group still showed the relative low occupancy of the ligands (80% and 60% respectively) and the alternative conformation for both Val68 and Gln64, although the crystals were soaked for more than 10 days, which suggests incomplete reactions. I hypothesized that the crystal packing mode can thus also affect the extent of the reaction. In other words, a crystal in the *P2₁* space group might be more accessible to the ligands than the one in *P6* according to the result using the H64Q mutant. I checked the

crystal packing of those two space groups of H64Q in *Pymol*, by assembling all symmetry mates within 50 Å of a reference point (Fig. 3-22).

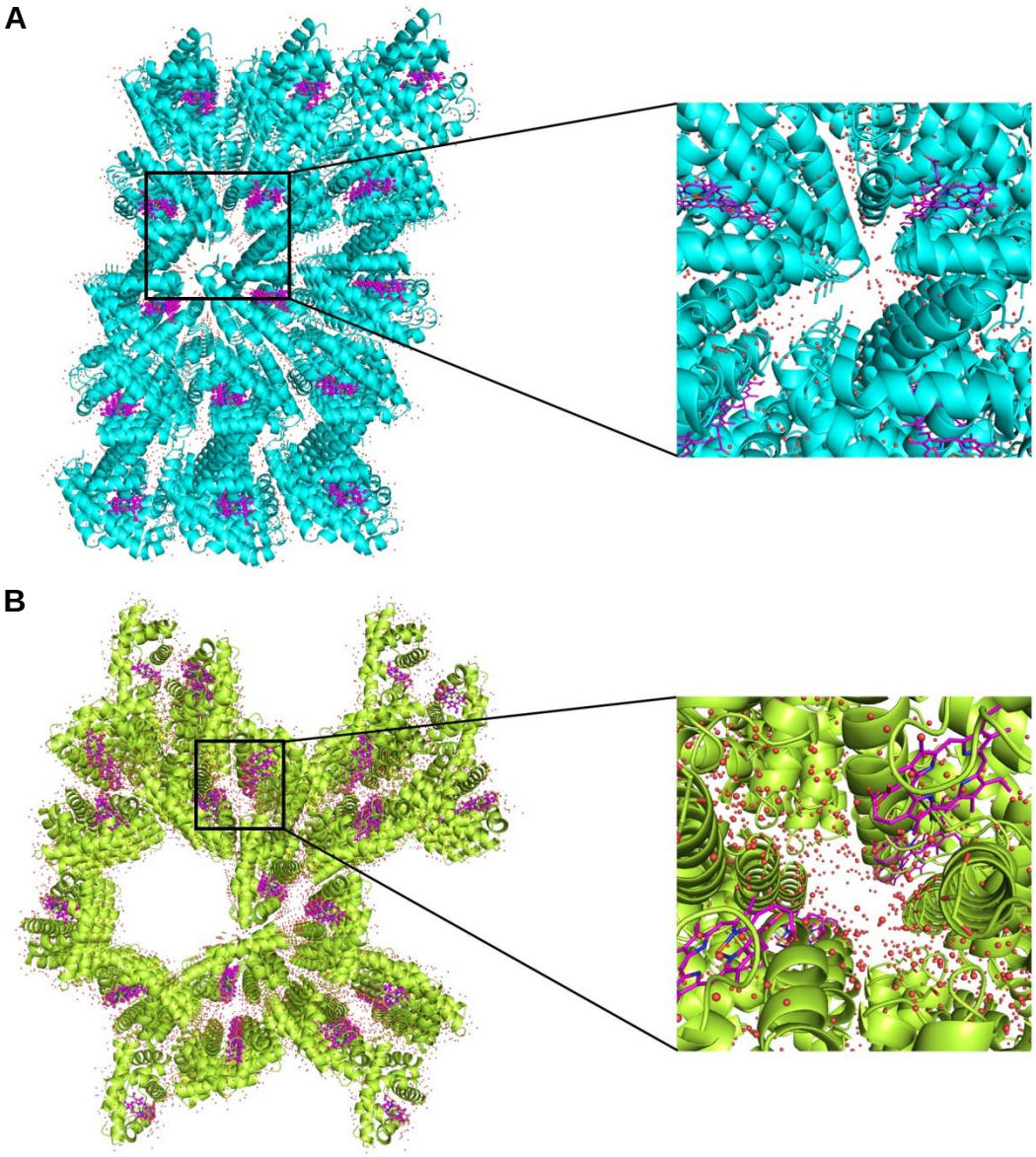

Fig. 3-22. Crystal packing of H64Q-H_2O in the two different space groups $P2_1$ (A) and *P6* (B). The molecules labeled by magenta are heme molecules. The solvent channels around heme were zoomed in on the right panels. The red spots in the two figures are water molecules.

There are 42 monomers in the $P2_1$ space group and 52 in the *P6* space group within a 50 Å radius (Fig. 3-22). We do notice that hemes (labeled by

magenta) in *P2$_1$* and *P6* are exposed to large channels which are accessible to solvents (right panels in Fig. 3-22). The interior solvent volume of the two assemblies generated by Pymol above was calculated using the 3V server [41]. Two probes with radii of 6 Å and 1.5 Å (the approximate size of a water molecule) were rolled through the surface of two assemblies to obtain the solvent channel in Fig. 3-23 with volumes of 260245 Å^3 for *P2$_1$*, and 248317 Å^3 for *P6*. It thus seems that the *P2$_1$* form is slightly more accessible to solvent than *P6*.

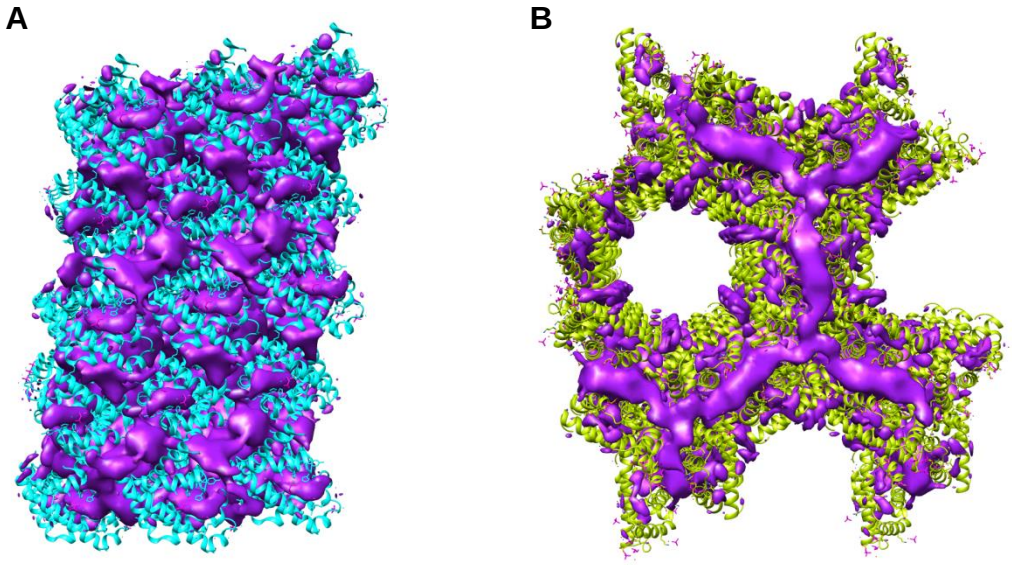

Fig. 3-23. The solvent channels of H64Q in the two different space group *P2$_1$* (A) and *P6* (B). These two assemblies were generated by *Pymol* and saved as the related coordinate files which were input into 3V server. The final images with interior channels were displayed by *Chimera*.

However, it is also evident from Fig. 3-23 that solvent and reagent can have better access to the interior solvent channel in *P6* space group. There are also the experimental data to support this point. I note that the H64A derivatives are in the *P6* space group, but have fast and stable reactions with arylhydrazines to give the H64A-phenyl and H64A-tolyl products. In addition,

the wt and V68A/I107Y crystals with *P2₁* space group have slow reaction times. There is not enough evidence at this time to show conclusively whether the crystal packing mode affects the outcome of the reaction. The comparison of sw Mb-H_2O which shows us another clue is shown in Fig. 3-24 (enlarged picture of Fig. 3-19A).

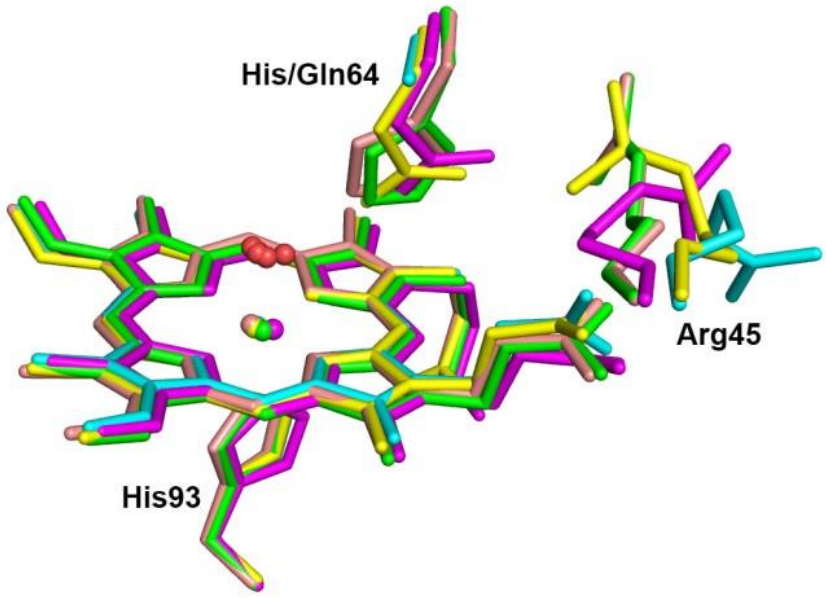

Fig. 3-24. Comparison of the sw Mb-H_2O structures. Each sw Mb is labeled by a different color, green (wt), cyan (H64A), magenta (H64Q (*P2₁*)), yellow (H64Q (*P6*)), and salmon (V68A/I107Y).

The Arg45 in cyan (H64A-H_2O) and magenta (H64Q-H_2O (*P2₁*)) are oriented towards the outside of the heme pocket. The other three Arg45s in wt-H_2O (green), H64Q-H_2O *P6* (yellow), and V68A/I107Y-H_2O (salmon) point to the protein interior which is thought to block ligand entrance (Fig. 3-24) according to the calculated results using *Hollow* (Fig. 3-24). During the soaking

experiments, only H64A and H64Q in $P2_1$ provided products of all three complexes with the best visualization of F_o-F_c maps. In other words, if the starting protein, *met* form (Mb-H_2O), has an outward orientation of Arg45, it might be easier to accommodate the ligands in the pocket.

3.4.6 The Tyr107 in V68A/I107T may direct the orientation of the methyl group in the Mb-tolyl derivatives

The methyl substituent of the tolyl group in the V68A/I107Y derivative ($P2_1$), with His64 in the distal pocket, points to the outside of the distal pocket, but the other three tolyl derivatives with the mutations at position 64 show that this methyl substituent points to the inside (Fig. 3-19C). As noted in Chapter 2, His64 plays a central role in NOx ligand orientations. However, in the V68A/I107Y, it appears that it is the bulky and hydrophilic Tyr sidechain that causes the methyl position to be located toward the protein exterior.

3.5 References

1. Malcamor, L. and A.A. Stark, Mutagenicity and Toxicity of Carcinogenic and Other Hydrazine Derivatives - Correlation between Toxic Potency in Animals and Toxic Potency in Salmonella-Typhimurium Ta1538. *Appl. Environ. Microbiol.* **1982**, *44*, 801-808.
2. Toth, B., Synthetic and Naturally Occurring Hydrazines as Possible Cancer Causative Agents. *Cancer Res.* **1975**, *35*, 3693-3697.
3. Liu, Y.Y. and D. Hoffmann, Quantitative Chromatographic Determination of Maleic Hydrazide in Cigarette-Smoke. *Anal. Chem.* **1973**, *45*, 2270-2273.
4. Sinha, B.K. and R.P. Mason, Biotransformation of Hydrazine Derivatives in the Mechanism of Toxicity. *J. Drug Metab. Toxicol.* **2014**, *5*, 1000168
5. Berger, J., Phenylhydrazine Haematotoxicity. *J. Appl. Biomed.* **2007**, *5*, 125-130.
6. Beaven, G.H. and J.C. White, Oxidation of Phenyl-Hydrazines in the Presence of Oxyhaemoglobin and the Origin of Heinz Bodies in Erythrocytes. *Nature* **1954**, *173*, 389-391.
7. Ringe, D., et al., Reaction of Myoglobin with Phenylhydrazine: A Molecular Doorstop. *Biochemistry* **1984**, *23*, 2-4.
8. Swanson, B.A. and P.R. Ortiz de Montellano, Structure and Absolute Stereochemistry of the 4 N-Phenylprotoporphyrin-Ix Regioisomers Isolated from Phenylhydrazine-Treated Myoglobin. *J. Am. Chem. Soc.* **1991**, *113*, 8146-8153.
9. Ortiz de Montellano, P.R. and D.E. Kerr, Inactivation of Myoglobin by Ortho-Substituted Arylhydrazines. Formation of Prosthetic Heme Aryl-Iron but Not N-Aryl Adducts. *Biochemistry* **1985**, *24*, 1147-1152.
10. Battioni, P., et al., Reaction of Monosubstituted Hydrazines and Diazenes with Rat-Liver Cytochrome-P450 - Formation of Ferrous-Diazene and Ferric Sigma-Alkyl Complexes. *Eur. J. Biochem.* **1983**, *134*, 241-248.
11. Muakkassah, S.F. and W.C.T. Yang, Mechanism of the Inhibitory-Action of Phenelzine on Microsomal Drug-Metabolism. *J. Pharmacol. Exp. Ther.* **1981**, *219*, 147-155.
12. Raag, R., et al., Formation, Crystal-Structure, and Rearrangement of a Cytochrome-P-450cam Iron Phenyl Complex. *Biochemistry* **1990**, *29*, 8119-8126.
13. Ortiz de Montellano, P.R. and D.E. Kerr, Inactivation of Catalase by Phenylhydrazine - Formation of a Stable Aryl-Iron Heme Complex. *J. Biol. Chem.* **1983**, *258*, 10558-10563.
14. Ortiz de Montellano, P.R., Arylhydrazines as Probes of Hemoprotein Structure and Function. *Biochimie* **1995**, *77*, 581-593.
15. Hill, H.A.O. and P.J. Thornalley, Phenyl Radical Production during the Oxidation of Phenylhydrazine and in Phenylphydrazine-Induced Hemolysis. *FEBS Lett.* **1981**, *125*, 235-238.

16. Ortiz de Montellano, P.R., et al., Carbon Radicals in the Metabolism of Alkyl Hydrazines. *J. Biol. Chem*. **1983**, *258*, 8623-8629.
17. Kunze, K.L. and P.R. Ortiz de Montellano, Formation of a Sigma-Bonded Aryliron Complex in the Reaction of Arylhydrazines with Hemoglobin and Myoglobin. *J. Am. Chem. Soc.* **1983**, *105*, 1380-1381.
18. Augusto, O., K.L. Kunze, and P.R. Ortiz de Montellano, N-Phenylprotoporphyrin-Ix Formation in the Hemoglobin-Phenylhydrazine Reaction - Evidence for a Protein-Stabilized Iron-Phenyl Intermediate. *J. Biol. Chem.* **1982**, *257*, 6231-6241.
19. Otwinowski, Z. and W. Minor, Processing of X-ray diffraction data collected in oscillation mode. *Method Enzymol.* **1997**, *276*, 307-326.
20. Winn, M.D., et al., Overview of the CCP4 suite and current developments. *Acta Crystallogr. D* **2011**, *67*, 235-242.
21. McCoy, A.J., et al., Phaser crystallographic software. *J. Appl. Crystallogr.* **2007**, *40,* 658-674.
22. Murshudov, G.N., A.A. Vagin, and E.J. Dodson, Refinement of macromolecular structures by the maximum-likelihood method. *Acta Crystallogr. D* **1997**, *53*, 240-55.
23. Afonine, P.V., et al., Towards automated crystallographic structure refinement with phenix.refine. *Acta Crystallogr. D Biol. Crystallogr.* **2012**, *68*, 352-67.
24. Emsley, P. and K. Cowtan, Coot: model-building tools for molecular graphics. *Acta Crystallogr. D Biol. Crystallogr.* **2004**, *60*, 2126-32.
25. Chen, V.B., et al., MolProbity: all-atom structure validation for macromolecular crystallography. *Acta Crystallogr. D Biol. Crystallogr.* **2010**, *66*, 12-21.
26. Schrodinger, LLC, The PyMOL Molecular Graphics System, Version 1.3r1. **2010**.
27. Read, R.J. and A.J. Schierbeek, A Phased Translation Function. *J. Appl. Crystallogr.* **1988**, *21*, 490-495.
28. Swanson, B.A. and P.R. Ortiz de Montellano, Structure and Absolute Stereochemistry of the 4 N-Phenylprotoporphyrin-Ix Regioisomers Isolated from Phenylhydrazine-Treated Myoglobin. *J. Am. Chem. Soc.* **1991**, *113*, 8146-8153.
29. Ortiz de Montellano, P.R. and D.E. Kerr, Inactivation of myoglobin by ortho-substituted arylhydrazines. Formation of prosthetic heme aryl-iron but not N-aryl adducts. *Biochemistry* **1985**, *24*, 1147-52.
30. Raag, R., et al., Formation, crystal structure, and rearrangement of a cytochrome P-450cam iron-phenyl complex. *Biochemistry* **1990**, *29*, 8119-26.
31. Ringe, D., et al., Reaction of myoglobin with phenylhydrazine: a molecular doorstop. *Biochemistry* **1984**, *23*, 2-4.
32. Mahy, J.P., et al., Reactions of Prostaglandin-H Synthase with Monosubstituted Hydrazines and Diazenes - Formation of Iron(Ii)-Diazene and Iron(Iii)-Sigma-Alkyl or Iron(Iii)-Sigma-Aryl Complexes. *Eur. J. Biochem.* **1994**, *226*, 445-457.

33. Augusto, O., K.L. Kunze, and P.R. Ortiz de Montellano, N-Phenylprotoporphyrin IX formation in the hemoglobin-phenylhydrazine reaction. Evidence for a protein-stabilized iron-phenyl intermediate. *J. Biol. Chem.* **1982**, *257*, 6231-41.
34. Ortiz de Montellano, P.R., Arylhydrazines as Probes of Hemoprotein Structure and Function. *Biochimie* **1995**, *77*, 581-593.
35. Ortiz de Montellano, P.R. and D.E. Kerr, Inactivation of catalase by phenylhydrazine. Formation of a stable aryl-iron heme complex. *J. Biol. Chem.* **1983**, *258*, 10558-63.
36. Kendrew, J.C., et al., A three-dimensional model of the myoglobin molecule obtained by x-ray analysis. *Nature* **1958**, *181*, 662-6.
37. Brucker, E.A., et al., High resolution crystal structures of the deoxy, oxy, and aquomet forms of cobalt myoglobin. *J. Biol. Chem.* **1996**, *271*, 25419-22.
38. Ho, B.K. and F. Gruswitz, HOLLOW: generating accurate representations of channel and interior surfaces in molecular structures. *BMC Struct. Biol.* **2008**, *8*, 49.
39. Phillips, G.N., Jr., Comparison of the dynamics of myoglobin in different crystal forms. *Biophys. J.* **1990**, *57*, 381-3.
40. Phillips, G.N., Jr., et al., Crystal structure of myoglobin from a synthetic gene. *Proteins* **1990**, *7*, 358-65.
41. Voss, N.R. and M. Gerstein, 3V: cavity, channel and cleft volume calculator and extractor. *Nucleic Acids Res.* **2010**, *38*, W555-62.

Chapter 4 Crystal structure and a preliminary functional assay of a non-metal FMN-binding nitroreductase from *Clostridium difficile*

4.1 Introduction

Clostridium difficile is a gram-positive and spore-forming anaerobic bacterium that infects colonic epithelial cells and causes life-threatening diarrhea and colitis [1]. At least 250,000 infections occur each year with about 14,000 associated deaths in the U.S. alone [2]. Both the infection rate and mortality rate continue to increase. Better detection methods, the frequent use of antibiotics and chemotherapeutics, and contaminated hospital environments are all believed to contribute to this documented increase [3, 4]. Individuals younger than 65 years in age are susceptible to *C. difficile* infections (CDIs), accounting for about 50% of all CDIs, but high mortality (~90%) occurs in individuals of age 65 and older [1, 2]. Among all strains of *C. difficile*, the hypervirulent strain R20291 causes more severe diarrhea that correlates with higher morbidity, mortality and recurrences. It was conservatively estimated that at least $1.1 billion per year is needed to treat CDIs in United States [5].

Metronidazole and vancomycin are the commonly used drugs for the treatment of *C. difficile* that reduce morbidity and mortality [6]. Metronidazole (MTZ; see below) is a low-cost nitro-containing drug that has high activity *in vitro*, high level of efficacy, and is postulated to have low potential for the selection of vancomycin-resistant *Enterococcus* (VRE) [6-8]. However, recent

reports show an increased failure of treatments of CDIs with metronidazole [6, 9, 10]. A recurrence rate of 15-35% has been reported for both metronidazole and vancomycin after initial successful therapy [6, 11, 12]. The resistance and reduced susceptibility to metronidazole and vancomycin have been documented [13, 14].

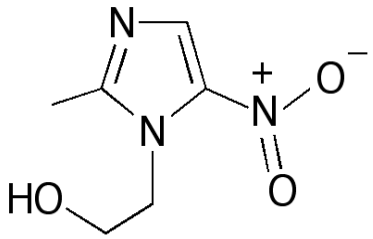

Mtz

Metronidazole typically functions as a prodrug which interacts with nitroreductase proteins in pathogens, and produces toxic metabolites to kill the pathogens. Metronidazole resistance has been related to a nitroreductase in *Bacteroides fragilis* [15-17] and *Helicobacter pylori* [18, 19], but with different mechanisms depending on whether the products from the metabolism of metronidazole by nitroreductases are toxic or non-toxic. Resistance to metronidazole in *B. fragilis* has been shown to be associated with *nim* genes [15-17]. *Nim* genes encode the nitroreductases that convert metronidazole to non-toxic amine derivatives, thus avoiding the formation of toxic nitroso or hydroxylamine derivitatives. These previously silent *nim* genes may be expressed or upregulated in the resistant strain, and thereby reduce nitro-containing durgs to non-toxic products such as amino derivatives which were not found in sensitive strains [15, 16]. In contrast, metronidazole resistance in

H. pylori is related to mutations of the *rdxA* and *frxA* genes, encoding nitroreductases that reduce nitro-containing drugs (e.g., metronidazole) to toxic nitroso or hydroxylamine derivatives [18, 19]. The inactivation of mutated rdxA and frxA prevented the formation of toxic products and further caused metronidazole resistance [19]. Only a few studies on metronidazole resistance in *C. difficile* have been reported. It is interesting to note that a truncated mutation in a nitroreductase was found in both a resistant strain and a sensitive strain with reduced susceptibility, implicating it in metronidazole resistance in *C. difficile* [20].

Nitroreductases are a family of FMN-dependent, NAD(P)H-linked proteins that transform nitro-substituted compounds to their corresponding toxic nitroso, hydroxylamine or non-toxic amine derivatives. This metabolic feature has attracted attention in bioremediation efforts for the cleanup of spent nitro-containing explosives such as TNT in contaminated soils [21]. Recently, more interest has been drawn to clinical biotechnological applications for cancer treatments [22, 23]. Based on the responses to oxygen during the reactions, nitroreductases are characterized as type I or type II (see the scheme below) [24].

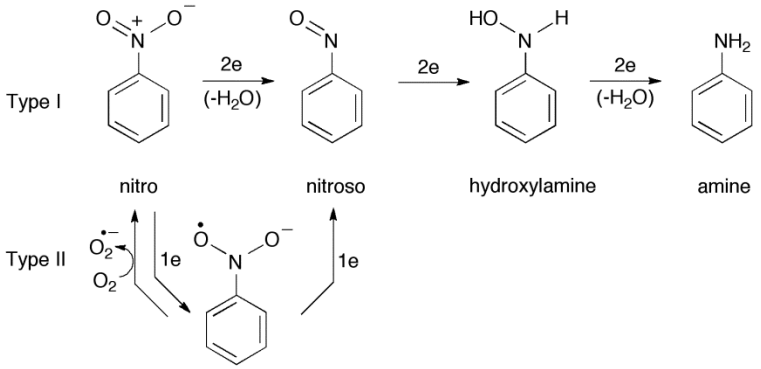

Nitroreductases are widely distributed in bacteria, and also exist in archaea and eukaryotes [24]. They catalyze the reduction of nitrocompounds in a ping-pong bi-bi kinetic mechanism and usually behave as homodimers varying in size (24-30 kDa) for each subunit [24]. The reactivity of nitro substrates with other bacterial nitroreductases is well known. The emergence of metronidazole-resistant *C. difficile* strains has created a critical need for understanding nitroreductase interactions with metronidazole. Only three nitroreductases from *C. difficile* have been reported, and these were from the less-virulent *C. difficile* 630 strain. These structures were deposited in the PDB, but no manuscripts describing the structures have been published. There is currently no structural information of any nitroreductase from the hypervirulent *C. difficile* R20291 strain and no functional assays for the reaction of nitro substrates (e.g., metronidazole) with nitroreductases in any *C. difficile* strain.

In this work, I determined the X-ray crystal structure of a 26 kDa nitroreductase (CDR20291_0684) from the hypervirulent *C. difficile* R20291 strain, which represents the first structural determination of a nitroreductase from the C. *difficile* hypervirulent strain. I also investigated the reaction of metronidazole with this nitroreductase, which is the first confirmation of the reduction of metronidazole by a nitroreductase in *C. difficile*. This work provides a future direction regarding the molecular basis of antibiotic resistance of *C. difficile* to the prodrug metronidazole.

4.2 Materials and methods

4.2.1 Cloning

A putative nitroreductase gene (CDR20291_0684) was identified from the genome sequence of hypervirulent *C. difficile* by a BLAST search against the annotation and conserved domain [25]. The recombinant plasmid pNYCOMPSC-0684 with the nitroreductase gene was constructed by our collaborators at the Albert Einstein College of Medicine (AECOM), and contained a C-terminal His10 tag extension to facilitate its purification.

4.2.2 Expression and purification of nitroreductase

The plasmid pNYCOMPSC-0684 was transformed into *E. coli* BL21 (DE3) competent cells. The nitroreductase was expressed in the cells with auto-induction [26]. In brief, cells were grown in ZY auto-inducing medium [26] supplemented with kanamycin (50 μg/ml), $MgSO_4$ (1 mM), glycerol (0.5%), glucose (0.05%), α-lactose (0.2%), 100 M vitamin B_{12}, and trace metals. Autoinduction is performed in an incubator with shaking. The temperature was set to 37°C for 5 h then adjusted to 22°C and left to incubate overnight.

After the cell pellets were harvested by centrifugation, the resulting yellow pellets were transferred into an anaerobic COY chamber containing 3% H_2 (in N_2). All purification procedures were performed in the chamber. The collected cells were resuspended in the binding buffer (0.1 M sodium phosphate, 0.5 M NaCl, 20 mM imidazole, 2 mM β-mercaptoethanol). The appropriate amounts of DNase, RNase, and PMSF were added in the solution. The sample was sonicated on ice. After centrifugation, the supernatant was

loaded onto a Ni affinity column (MCLAB) equilibrated with binding buffer. The column was then washed with the washing buffer (binding buffer but with 50 mM imidazole). The attached His-tagged protein was eluted from the column with the elution buffer (binding buffer with 250 mM or 500 mM imidazole). Fractions were collected throughtout the column and the presence of protein was verified by SDS-PAGE.

The eluted protein fractions were pooled and concentrated using an Amicon ultra filter with a cutoff of 10 kDa (Millipore). The concentrated sample was applied to a gel filtration Superdex 200 increase 10/300GL column set up on an AKTA FPLC system (GE Healthcare) equilibrated with gel filtration buffer (20 mM Tris, pH 7, 2 mM β-mercaptoethanol). The elution profile of the nitroreductase was monitored and recorded at 280 nm by UV light in an AKTA FPLC. The molecular mass of nitroreductase was estimated relative to the molecular masses of other proteins used as standard proteins; conalbumin (75 kDa), ovalbumin (44 kDa), carbonic anhydrase (29 kDa), and ribonulease A (13.7 kDa). The fractions containing the nitroreductase (by SDS-PAGE) were pooled and concentrated to ~5 mg/ml.

4.2.3 Crystallization of nitroreductase

Broad screen crystallization trials (MCSG1, MCSG2, CSHT, and Wizard) were carried out in the nanoliter scale with a Mosqito robot (TTP Labtech). The sitting drop vapor diffusion method was used by mixing 300 nl of protein and 300 nl of well solutions in MRC 2 subwell plates (Swissci) with 60 µl of well solution. After a couple of days, tiny rod shaped yellow crystals with sizes

around 20 µm formed in MCSG1 (Microlytic) well C8 (0.2 M ammonium sulfate, 25 % PEG 4000, 0.1M sodium citrate, pH 5.6). Larger crystals (~140 µm long) were obtained after manual optimization in 10% PEG 1500, 0.1 M sodium citrate, and pH 5.6. In order to obtain good diffraction data from the crystals, the crystals were washed in a cryosolution of the same composition as that used in the crystal well solution but with 25% ethylene glycol.

4.2.4 Data processing, structure solution and refinement

Selected yellow crystals were sent to the Stanford Synchrotron Radiation Laboratory (SSRL) for X-ray data collection at the BL12-2 beam line.

The diffraction data was processed using HKL3000 [27]. The structure factors were calculated using the CCP4 program suite [28].

The three-dimensional structure of the full-length nitroreductase was solved by molecular replacement in *PHASER* (CCP4) [28, 29] using an ensemble of the superimposed models from PDB_3PXV (*D. hafniense*) and PDB_3EK3 (*B. fragilis*). All refinements were performed by *Refmac5* [28, 30]. The model was rebuilt by *COOT* [31]. The *MolProbity* server was used for structure validation [32].

Ten initial cycles of restrained refinement were run with *Refmac*, and the *R* factor decreased from 0.40 to 0.33. Ligands (FMN, phosphate ion) and water were added to the model based on the F_o-F_c electron density maps in the subsequent refinement cycles. An FMN co-factor restraint file was generated using *ACEDRG* [28]. Two FMN co-factors, one glycerol, and one phosphate anion were added into the model. 138 water molecules were sequentially added

by *COOT*. Two conformations of the sidechains of Asp7 in monomer A and Ile154 in monomer B were modeled with 50% occupancy for each conformation. Some residues in monomer A (the first 5 residues in N-terminus and 18 residues in C-terminus) and monomer B (6 residues in N-terminus and 16 residues in C-terminus) were omitted because of the lack of clear electron density. The final *R* factor and R_{free} are 0.17 and 0.22, respectively.

4.2.5 Assay of nitroreductase activity

The protein concentration was calculated using the calculated extinction coefficient at 280 nm of 21430 l/cm/mol from *ProtParam* [33]. The reduction and re-oxidation of the nitroreductases were examined under anaerobic conditions. All buffers were purged by nitrogen gas for at least 30 min and moved into the anaerobic chamber. The titration experiments were carried out in the chamber as described previously [34]. A sealable quartz cuvette (Starna cells) with a septum was used. In general, ~17 µM of nitroreductase in 3 ml of 20 mM Tris pH 7, was reduced by sequentially adding 1 µl of dithionite (11 additions) at ~20 mM in the same buffer as the protein to obtain the spectrum of reduced form. Re-oxidation of nitroreductase was then performed by also sequentially adding 1 µl of nitro-containing drugs (nitrofurazone or metronidazole; 12 sequential additions each) at 1 mM into the reduced protein. After each addition, the cuvette was sealed and UV-vis spectra were recorded using a Hewlett Packard 8453 spectrophotometer.

4.3 Results

4.3.1 Protein characterization

The nitroreductase (CDR20291_0684) was expressed in good yield (~50 mg/L) in *E. coli*. The purified protein showed a deep yellow color as expected for an FMN-containing protein. The protein was obtained in high purity (>98%) as shown by SDS-PAGE, and the band was located just above the 25 kDa marker band, matching the calculated nitroreductase molecular mass of 26 kDa (Fig. 4-1A). Information from gel filtration of the protein indicates that it was isolated as a dimer; this corresponds well with that previously reported for other bacterial nitroreductases [35-39]. Yellow crystals (~20 µm) were obtained from an initial MCSG1 screen with larger crystals (~140 µm) obtained after manual optimization (Fig. 4-1B).

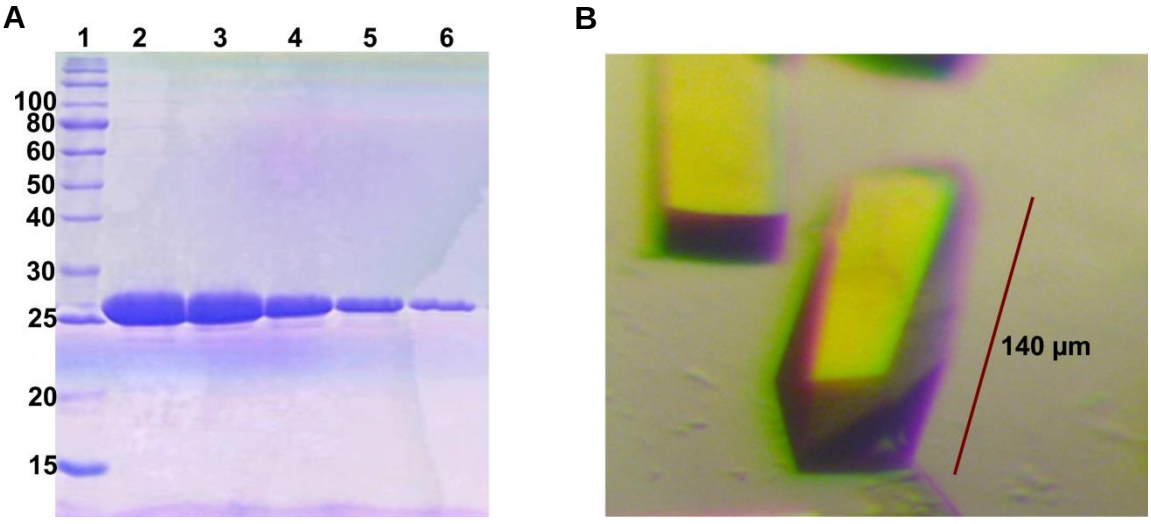

Fig. 4-1. A) nitroreductase characterization by SDS-PAGE analysis of the purified nitroreductase after gel filtration: 1 Marker, 2-6 fractions; B) Crystals of the nitroreductase.

4.3.2 Overall structure of nitroreductase from hypervirulent *C. difficile* R20291

The three dimensional structure at 2.1 Å resolution was obtained from a crystal in the space group $P4_12_12$ (Table 4-1). The crystal structure revealed that the nitroreductase is a homodimer (Fig. 4-2A) with each monomer binding one equivalent of FMN. The cloned protein has 231 amino acid residues including 10 His residues and 8 extra residues in the C-terminus from the plasmid. Based on the electron density map, 208 residues were modeled into monomer A excluding 5 residues in the N-terminus and 18 residues in the C-terminus due to the lack of electron density. 209 residues were modeled into monomer B that lacked clear electron density for 6 residues in N-terminus and 16 residues in C-terminus.

Table 4-1. Data collection and refinement statistics

Protein No.	CDR20291_0684 YP_003217185
PDB ID	5J62
Data collection[a]	
Space group	*P* 4_1 2_1 *2*
Wavelength (Å)	0.98
Cell dimensions (Å, deg)	100.32, 100.32, 99.92 90.00, 90.00, 90.00
Resolution (Å)	50.00-2.12
I/σ[I]	17.33 (0.67)
No. of reflections	
Observed	530168
Unique	55935 (2675)
Multiplicity	9.5 (3.8)
Completeness (%)	99.7 (96.7)
R_{merge}[b]	0.071 (0.782)
Refinement statistics	
No. of protein atoms	3274
R factor (%)[c]	0.17
R_{free} (%)[d]	0.22
RMSD Bond lengths (Å)	0.016
RMSD Bond angles (°)	1.700
B Factor	50.32
Ramachandran plot (%)[e]	
Most favored residues	98.8
Outliers	0.24

[a] Values in parentheses correspond to the highest resolution shells.
[b] $R_{merge}=\Sigma|I-\langle I\rangle|/\Sigma(I)$, where I is the individual intensity observation and $\langle I\rangle$ is the mean of all measurements of I.
[c] $R=\Sigma||F_o|-|F_c||/\Sigma|F_o|$, where F_o and F_c are the observed and calculated structural factors, respectively.
[d] R_{free} was calculated by using 5% of the randomly selected diffraction data which were excluded from the refinement.
[e] As calculated using *MOLPROBITY*.

The protein adopts a classic nitroreductase α+β fold [34, 40] with the FMN cofactors located at the interface of the monomers. Each monomer consists of a β-sheet in the central core surrounded by α-helices (Fig. 4-2A, B).

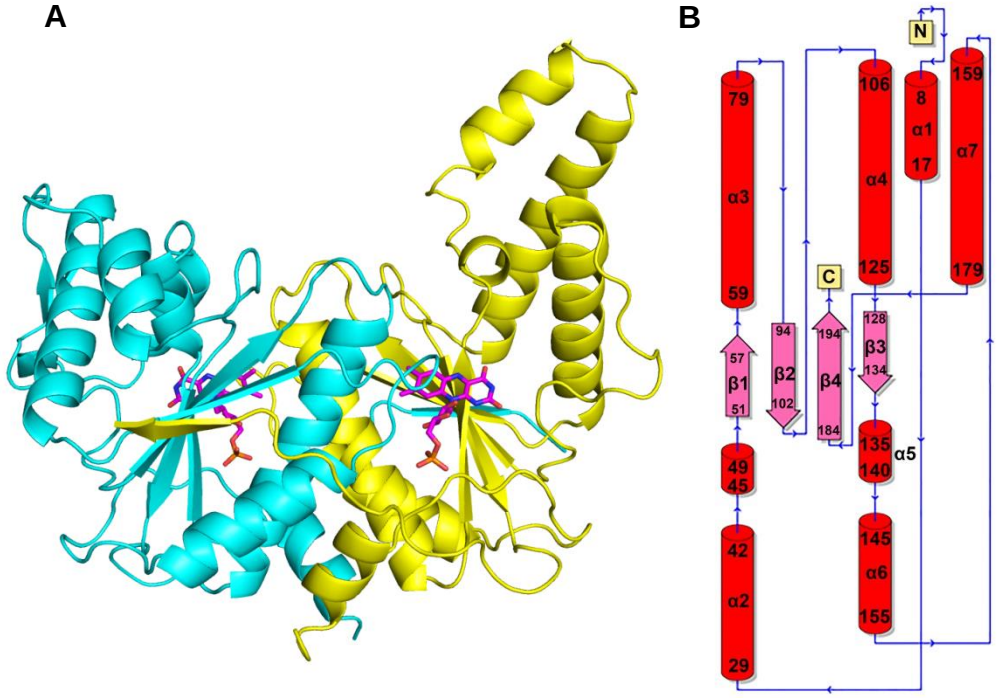

Fig. 4-2. Crystal structure of the nitroreductase. A) Overall crystal structure of nitroreductase showing the dimeric configuration and FMN-binding sites (stick model in magenta); B) Topology of the monomer (using PDBsum).

The five-strand β sheet (β5β1β2β4β3) arrangement is formed from four antiparallel β strands (β1β2β4β3) (Fig. 4-2B) complemented by a fifth strand β5 from the other monomer (Fig. 4-3). Each monomer folded in a similar conformation except one segment comprised of α6 and α7 (see the arrows in the right panel of Fig. 4-3) which stretched out in monomer A instead of folding down and wrapping the α3 in monomer B. The helices of α6 and α7 in monomer B are shorter and partially unfold into a disordered structure in order to wrap

around α3. To stabilize the disordered segment, monomer B forms an extra β sheet out of the β sheet in the central core (circled area in Fig. 4-3 right).

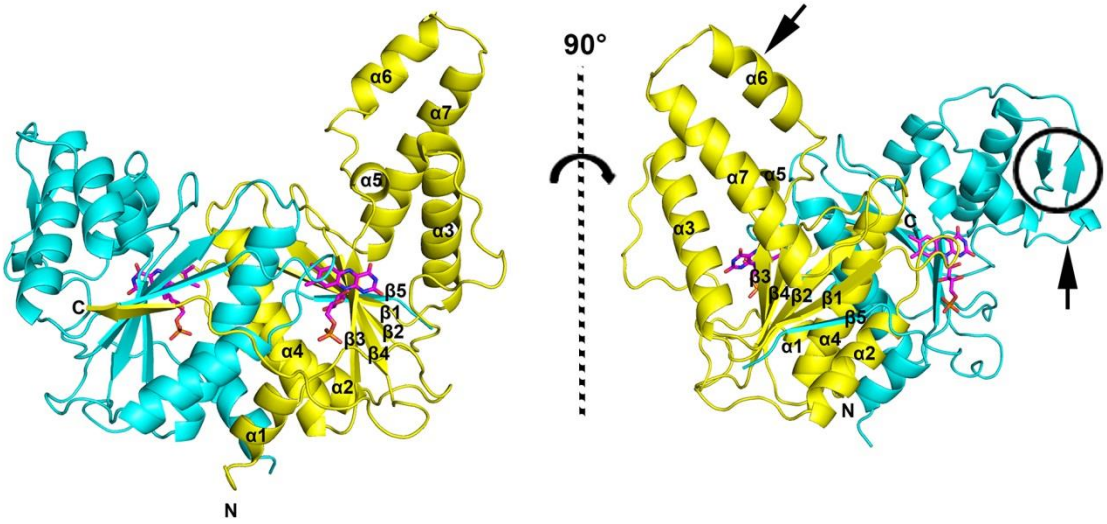

Fig. 4-3. Views of the nitroreductase structure. The structure is shown in two different orientations with a 90° rotation around the vertical axis. The yellow represents monomer A and the cyan represents monomer B. The motifs of the secondary structure in the monomer A are labeled in the structure. Arrows point to the segments with different folding in each monomer. The circled area is the extra β sheet in monomer B.

We searched for homologs of the nitroreductase (CDR20291_0684) using the amino acid sequence (NCBI BLAST). The resulting twelve potential homologs are listed in Fig. 4-4, and all showed <30% sequence identity when compared with our nitroreductase from hypervirulent *C. difficile* strain R20291. Similar results were also obtained from 3D structural comparisons using the Dali server (http://ekhidna.biocenter.helsinki.fi/dali_server/start).

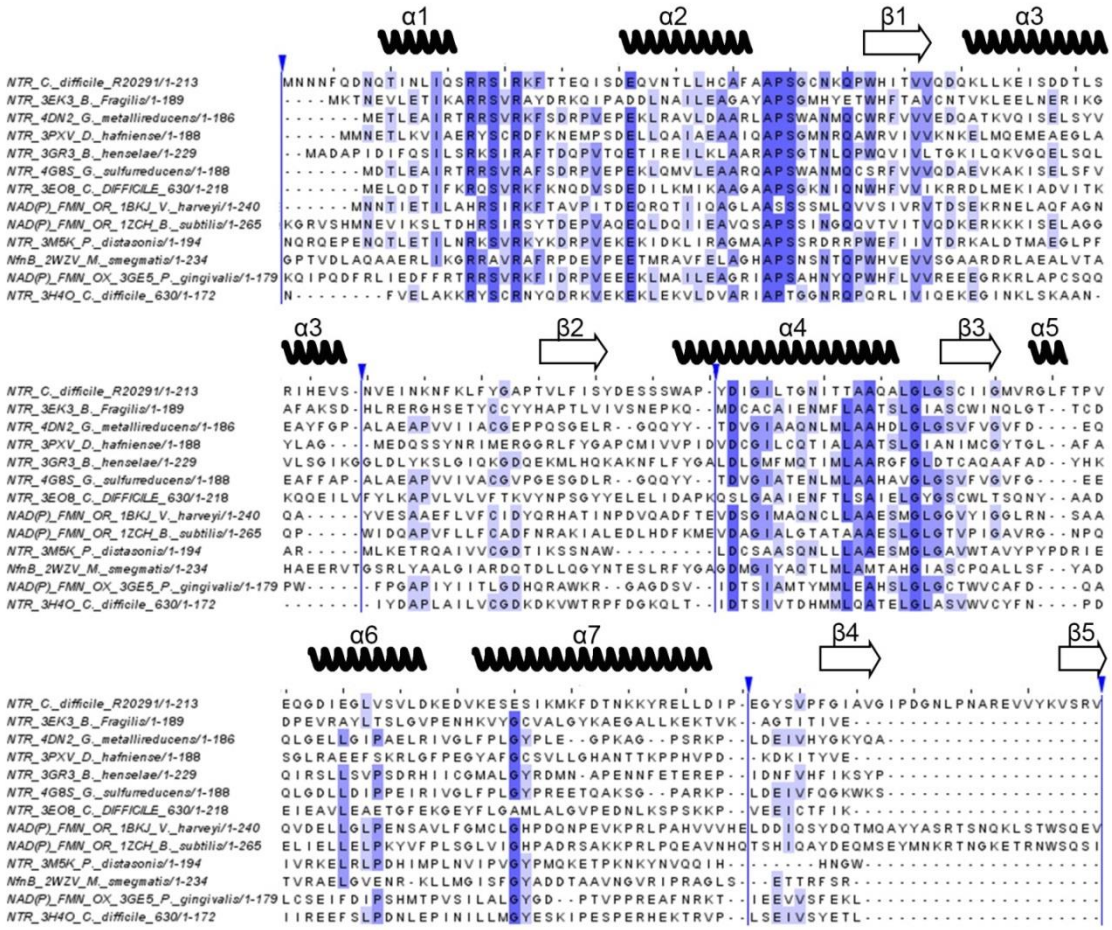

Fig. 4-4. Sequence alignment of *C. difficile* nitroreductases with potential homologs using CLUSTAL in JALVIEW (truncated display). Blue lines stand for the omitted gaps.

The listed proteins in Fig. 4-4 are annotated as either nitroreductases or NAD(P)H:FMN oxidoreductases. The closest homolog of our *C. difficile* nitroreductase, based on sequence alignment, is the nitroreductase from *B. fragilis* (PDB_3EK3). The closest 3D structural homolog is the nitroreductase from *D. hafniense* (PDB_3PXV) as determined using a structural comparisons on the DALI server (RMSD 2.1, Z score 21). Most of the homologs from Fig. 4-4 have a very similar overall protein fold (avg. RMSD 1.5-2.8 Å and Z score 21-15

from DALI server) as our *C. difficile* R20291 nitroreductase even with low sequence identities (an example is shown in Fig. 4-5).

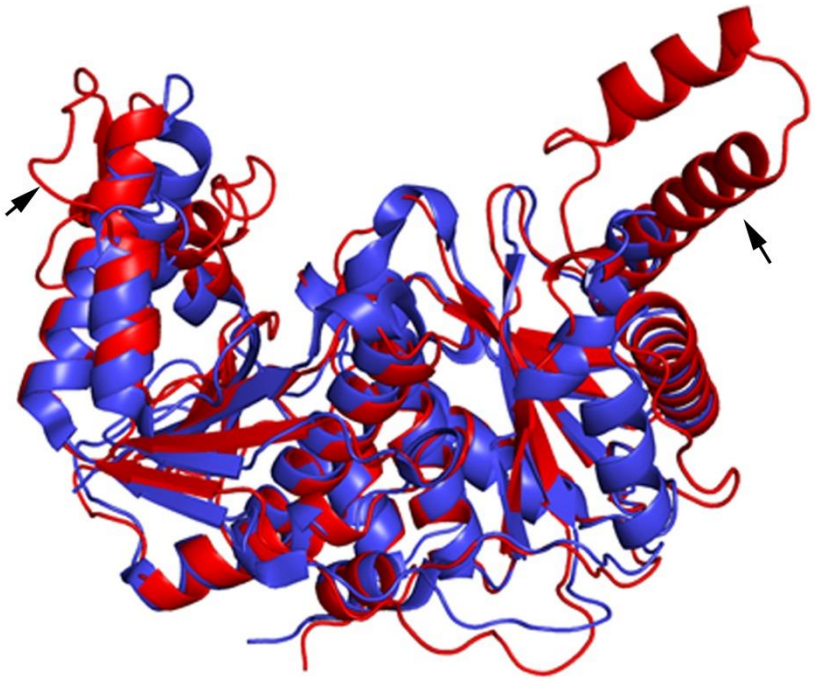

Fig. 4-5. Structural alignment of nitroreductases from hypervirulent *C. difficile* R20291 (red) and from *D. hafniense* (3PXV, in blue) using *PYMOL*. Arrows represent the unique segment in each monomer of nitroreductase from *C. difficile*.

The results from the structural comparisons showed that the segment described above in our nitroreductase (CDR20291_0684) is quite unique. No similar segment has been found so far for any of the other proteins.

4.3.3 FMN co-factor binding sites

The nitroreductase dimer contains two FMN cofactors located near the interface of the monomers (Fig. 4-6). The FMN in the left panel of Fig. 4-6 interacts primarily with most residues from monomer A, and one residue (S45) from monomer B. Two water molecules underneath the FMN isoalloxazine

moiety of monomer A are involved in the interaction network of this FMN. There are no water molecules above the isoalloxazine group. Unlike that observed for the first FMN, a phosphate group is present in the second FMN binding site (right panel in Fig. 4-6). More water molecules above the isoalloxazine group participate in FMN interactions, but there are no water molecules underneath the FMN in this case, probably due to an FMN positional shift after incorporation of a phosphate group. Similar to that seen for the first FMN, the second FMN also interacts mostly with residues from monomer B, but two extra residues (A43 and C47) other than S45 joined this network. C47 and two water molecules stabilize the phosphate group which occupies the proposed substrate binding position. Interestingly, C47 is located in a loop area that is above the FMN plane in both monomers, and this loop area is assumed to interact with substrates (see arrows in Fig. 4-6). C47 does not interact with the first FMN in monomer A but does interact with the phosphate group in the second FMN binding site, which provides additional support for the idea that C47 may function in the interaction with substrates.

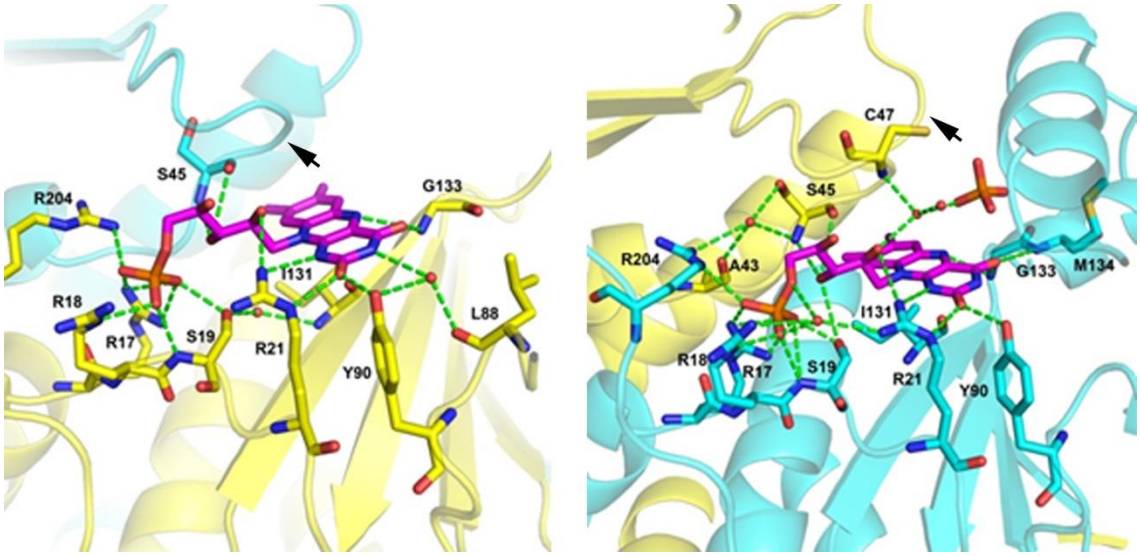

Fig. 4-6. Two FMN binding sites around monomer A (left) and monomer B (right). Monomer A and monomer B are in yellow and cyan respectively. Water molecules involved in the FMN interaction networks are presented by red spheres. Arrows point to the loop that may interact with substrates.

It is apparent that the FMN cofactor in monomer B is exposed to the solvent (Fig. 4-7 right), whereas the other FMN cofactor is blocked due to the interaction with a protein segment (residues 136-180) discussed above in the crystal, partially restricting its access to the solvent region (Fig. 4-7 left panel).

4.3.4 Functional assays

The nitroreductase was reduced anaerobically using dithionite, with a corresponding color change from yellow (oxidized FMN) to colorless (reduced FMN) (Fig. 4-8A). Oxidized nitroreductase has a typical absorption spectrum of

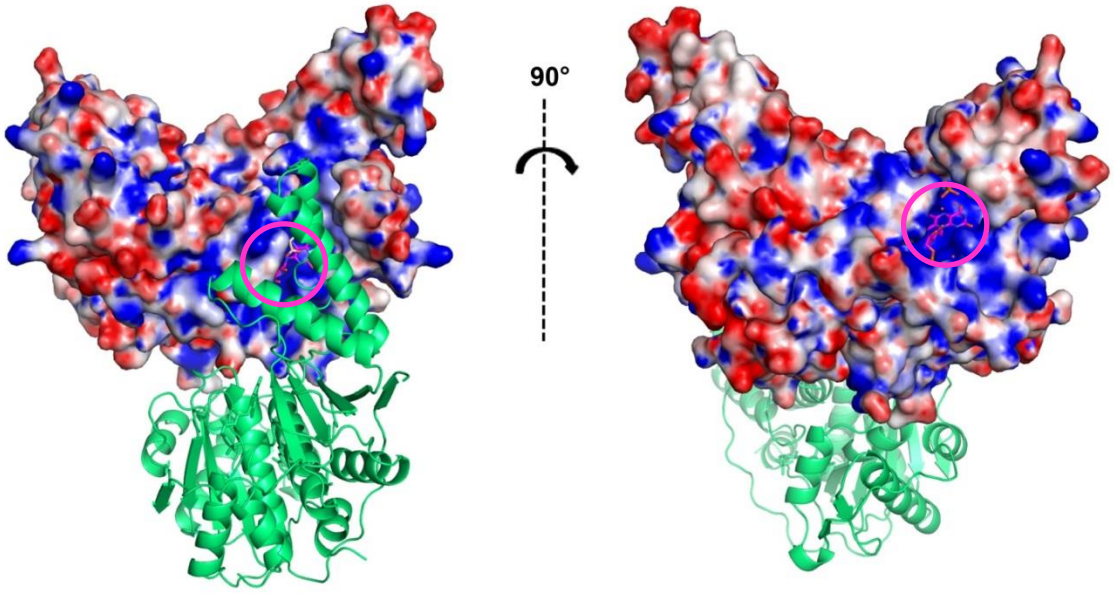

Fig. 4-7. View of the interaction between symmetry mates. The structure is shown in two different views with 90° rotation around the vertical axis. The upper regions of the two panels are the electrostatic surfaces of the nitroreductase with two FMN binding sites circled. A symmetry mate around nitroreductase was labeled green.

a flavoprotein with absorbances at 370 nm and 450 nm. Upon dithionite addition, these absorbances decreased (Fig. 4-8A). Reduced nitroreductase is susceptible to react with oxygen, and even small amount of air leaking into the cuvette will cause changes in the spectra due to the re-oxidation of nitroreductase by oxygen.

Reduced nitroreductase (in the absence of dithionite) can be anaerobically re-oxidized by the addition of nitro-containing metronidazole or nitrofurazone, with a corresponding color change from colorless (reduced FMN) back to yellow (oxidized FMN) (Fig. 4-8B, C). The absorbances at 450 nm increased as the reduced protein (lowest thick dashed line) became oxidized (top thick line).

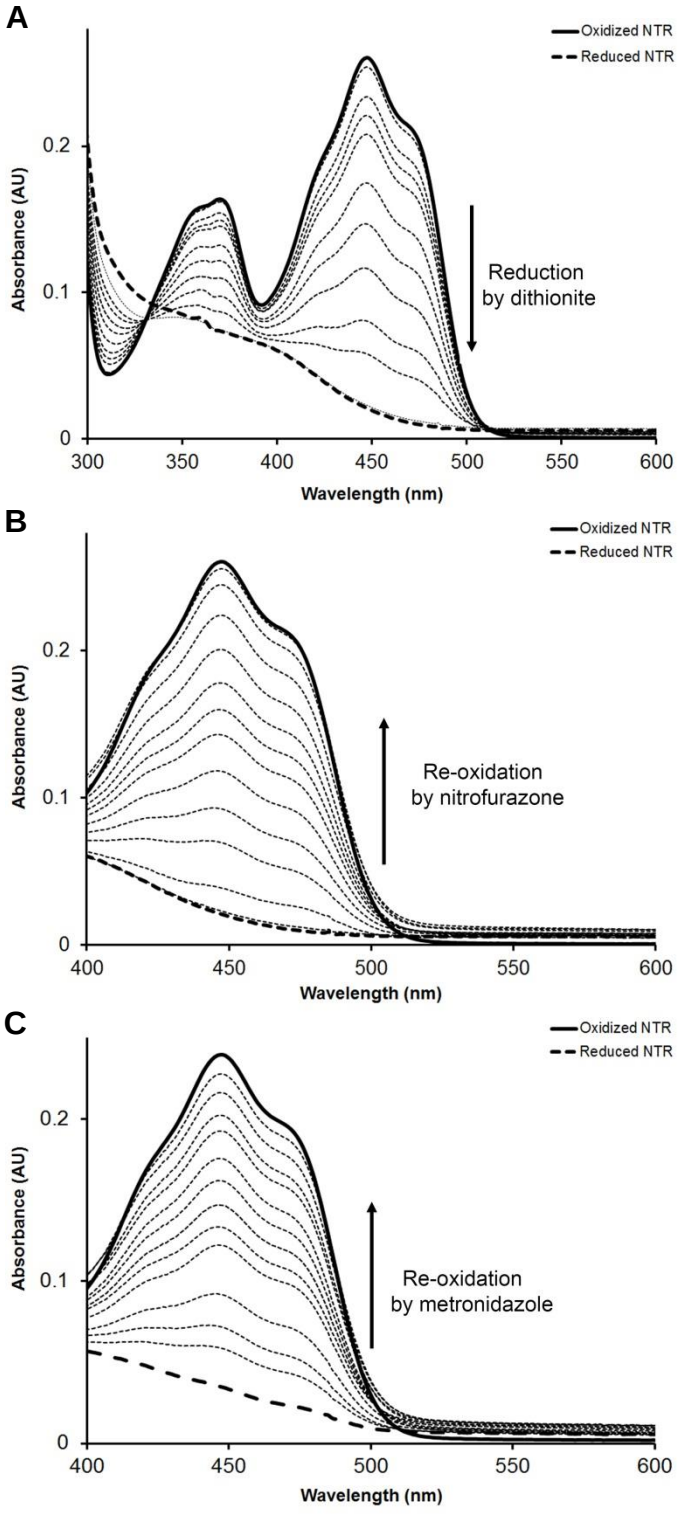

Fig. 4-8. Reduction and re-oxidation of nitroreductase. A) Reduction of nitroreductase by sequential addition of dithionite; B) Re-oxidation of nitroreductase by sequential addition of nitrofurazone; C) Re-oxidation of nitroreductase by sequential addition of metronidazole. Conditions: 20 mM Tris buffer, pH 7, [protein] = 16-17 µM, each addition of [dithionite] = 7 µM, each addition of [substrates] = 0.3 µM.

4.4 Discussion

The overall structure of nitroreductase (CDR20291_0684) displays a conserved fold as observed with other nitroreductase structures (DALI server) even with low sequence similarity. A unique segment (136-180) on each monomer was observed in the structure of this *C. difficile* nitroreductase, however, the segment folded in a different way in each monomer in this homodimer structure. It is not clear what the physiological role is for this different folding of this segment in this nitroreductase. Instead of folding down in monomer B, the segment in monomer A inserts into another monomer A from a neighboring symmetry mate, and blocks the FMN binding site resulting in restricted solvent accessibility to FMN. This implies that the nitroreductase (CDR20291_0684) may interact with other proteins through this unique segment in hypervirulent *C. difficile*, and perhaps performs other roles other than simply work as a nitroreductase. To test this hypothesis, it would be interesting to design a further functional assay to find other interacting proteins, as this might help to determine the physiological role of this nitroreductase *in vivo*.

RdxA, a type I nitroreductase (reduce nitro compounds by a 2e reduction) implicated in metronidazole resistance in *H. pylori*, was reported to have a cysteine (C159) close to the bound FMN co-factor (Fig. 4-9B), which presumably donates a proton to N1 of FMN and contributes to the reduction of metronidazole [40]. Another necessary protonation of N5 in FMN was proposed to be achieved by the light receptor photoropin protein in this single cysteine

system with only one cysteine beneath the isoalloxazine ring [40-42]. Our nitroreductase has a conserved cysteine (C130) underneath the isoalloxazine ring of FMN with an even closer distance of 3.5 Å than the 4.2 Å observed in RdxA, which implies that C130 in nitroreductase from hypervirulent *C. difficile* may perform a similar role to donate a proton to N1 of FMN as with the C159 in RdxA, but may be more active in the metabolism of metronidazole.

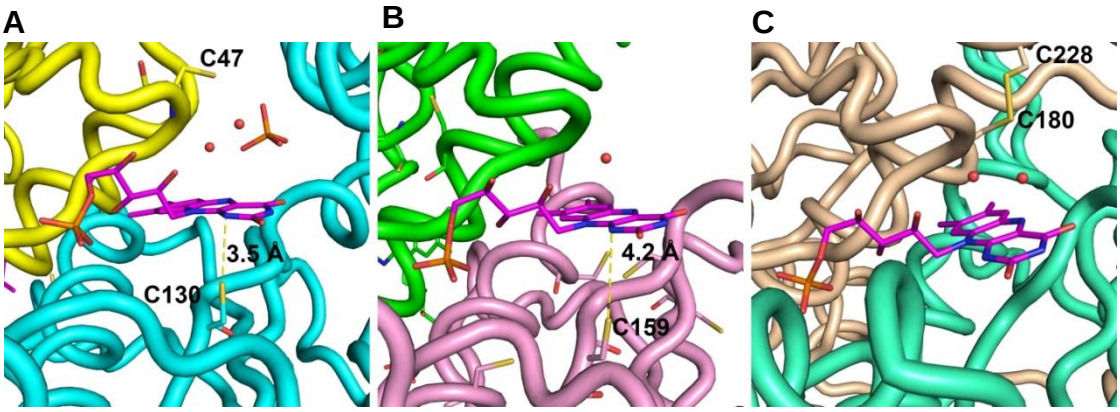

Fig. 4-9. Cysteines around FMN binding site in this nitroreductase from hypervirulent *C. difficile* strain (A), RdxA (PDB ID 3QDL) from *H. pylori* (B) and peroxiredoxin nitroreductase fusion enzyme (PDB ID 4EO3) from *T. maritima* (C). Each monomer in the three structures is distinguished by a different color. FMN co-factors are in magenta. Red spheres represent water molecules.

Perhaps most interesting, however, is the observation of another single cysteine (C47) above the isoalloxazine ring (Fig. 4-9A). This cysteine is located in a loop area which is proposed to interact with substrate. All three proteins in Fig. 9 have this loop. I checked 600 structural homologs (note: homologs here are actually extracted monomers from the published structures) of our nitroreductase using the DALI server, and none of the homologs had a cysteine in this position. We do find another structure with a cysteine in the neighboring position of C47 of this loop area in peroxiredoxin nitroreductase from *T.*

maritima, but it formed a disulfide bond which was confirmed to have a role in structural need instead of catalytic function (Fig. 4-9C) [38]. In our structure, there is no other cysteine to form a disulfide bond; also there are no other residues which could donate a proton to the N5 of FMN from this position. Based on this information, we propose that C47 in the loop with a distance 6.6 Å to N5 could donate a proton to N5 of FMN in nitroreductase with a relative positional adjustment of the loop, which provides another possible mechanism for the protonation of N5 for the unique two cysteine system on each side of the isoalloxazine ring.

In conclusion, the first isolation and structural characterization of a *C. difficile* nitroreductase from the pathogenic strain was obtained. An initial functional assay shows that it indeed functions as a nitroreductase with metronidazole and nitrofurazone (also an antibiotic).

4.5 References

1. Poutanen, S.M. and A.E. Simor, Clostridium difficile-associated diarrhea in adults. CMAJ 2004, **171**, 51-8.
2. Centers for Disease Control and Prevention, Antibiotic resistance threats in the United States. 2013.
3. O'Connor, J.R., S. Johnson, and D.N. Gerding, Clostridium difficile infection caused by the epidemic BI/NAP1/027 strain. Gastroenterology 2009, **136**, 1913-24.
4. Voth, D.E. and J.D. Ballard, Clostridium difficile toxins: mechanism of action and role in disease. Clin. Microbiol. Rev. 2005, **18**, 247-63.
5. Kyne, L., et al., Health care costs and mortality associated with nosocomial diarrhea due to Clostridium difficile. Clin. Infect. Dis. 2002, **34**, 346-53.
6. Leffler, D.A. and J.T. Lamont, Treatment of Clostridium difficile-associated disease. Gastroenterology 2009, **136**, 1899-912.
7. Freeman, J., et al., Surveillance for resistance to metronidazole and vancomycin in genotypically distinct and UK epidemic Clostridium difficile isolates in a large teaching hospital. J. Antimicrob. Chemoth. 2005, **56**, 988-9.
8. Pelaez, T., et al., Reassessment of Clostridium difficile susceptibility to metronidazole and vancomycin. Antimicrob. Agents Chemoth. 2002, **46**, 1647-50.
9. Musher, D.M., et al., Relatively poor outcome after treatment of Clostridium difficile colitis with metronidazole. Clin. Infect Dis. 2005, **40**, 1586-90.
10. Nair, S., et al., Clostridium difficile colitis: factors influencing treatment failure and relapse--a prospective evaluation. Am. J. Gastroenterol. 1998, **93**, 1873-6.
11. Alonso, R., et al., Molecular analysis of relapse vs re-infection in HIV-positive patients suffering from recurrent Clostridium difficile associated diarrhoea. J. Hosp. Infect. 2001, **48**, 86-92.
12. Barbut, F., et al., Epidemiology of recurrences or reinfections of Clostridium difficile-associated diarrhea. J. Clin. Microbiol. 2000, **38**, 2386-8.
13. Baines, S.D., et al., Emergence of reduced susceptibility to metronidazole in Clostridium difficile. J. Antimicrob. Chemoth. 2008, **62**, 1046-52.
14. Huang, H., et al., Antimicrobial resistance in Clostridium difficile. Int. J. Antimicrob. Agents 2009, **34**, 516-22.
15. Gal, M. and J.S. Brazier, Metronidazole resistance in Bacteroides spp. carrying nim genes and the selection of slow-growing metronidazole-resistant mutants. J. Antimicrob. Chemoth. 2004, **54**, 109-16.
16. Reysset, G., Genetics of 5-nitroimidazole resistance in Bacteroides species. Anaerobe. 1996, **2**, 59-69.

17. Schapiro, J.M., et al., Isolation of metronidazole-resistant Bacteroides fragilis carrying the nimA nitroreductase gene from a patient in Washington State. J. Clin. Microbiol. 2004, **42**, 4127-9.
18. Sisson, G., et al., Metronidazole activation is mutagenic and causes DNA fragmentation in Helicobacter pylori and in Escherichia coli containing a cloned H. pylori rdxA plus (nitroreductase) gene. J. Bacteriol. 2000, **182**, 5091-5096.
19. Jeong, J.Y., et al., Sequential inactivation of rdxA (HP0954) and frxA (HP0642) nitroreductase genes causes moderate and high-level metronidazole resistance in Helicobacter pylori. J. Bacteriol. 2000, **182**, 5082-90.
20. Lynch, T., et al., Characterization of a stable, metronidazole-resistant Clostridium difficile clinical isolate. PLoS ONE 2013, **8**, e53757.
21. Kutty, R. and G.N. Bennett, Biochemical characterization of trinitrotoluene transforming oxygen-insensitive nitroreductases from Clostridium acetobutylicum ATCC 824. Arch. Microbiol. 2005, **184**, 158-67.
22. Xu, G. and H.L. McLeod, Strategies for enzyme/prodrug cancer therapy. Clin. Cancer Res. 2001, **7**, 3314-24.
23. Prosser, G.A., et al., Discovery and evaluation of Escherichia coli nitroreductases that activate the anti-cancer prodrug CB1954. Biochem. Pharmacol. 2010, **79**, 678-87.
24. Roldan, M.D., et al., Reduction of polynitroaromatic compounds: the bacterial nitroreductases. FEMS Microbiol. Rev. 2008, **32**, 474-500.
25. Altschul, S.F., et al., Gapped BLAST and PSI-BLAST: a new generation of protein database search programs. Nucleic Acids Res. 1997, **25**, 3389-402.
26. Studier, F.W., Protein production by auto-induction in high density shaking cultures. Protein Expr. Purif. 2005, **41**, 207-34.
27. Otwinowski, Z. and W. Minor, Processing of X-ray diffraction data collected in oscillation mode. Method Enzymol. 1997, **276**, 307-326.
28. Winn, M.D., et al., Overview of the CCP4 suite and current developments. Acta Crystallogr. D Biol. Crystallogr. 2011, **67**, 235-242.
29. McCoy, A.J., et al., Phaser crystallographic software. J. Appl. Crystallogr. 2007, **40**, 658-674.
30. Murshudov, G.N., A.A. Vagin, and E.J. Dodson, Refinement of macromolecular structures by the maximum-likelihood method. Acta Crystallogr D Biol Crystallogr, 1997. **53**(Pt 3): p. 240-55.
31. Emsley, P. and K. Cowtan, Coot: model-building tools for molecular graphics. Acta Crystallogr. D Biol. Crystallogr. 2004, **60**, 2126-32.
32. Chen, V.B., et al., MolProbity: all-atom structure validation for macromolecular crystallography. Acta Crystallogr. D Biol. Crystallogr. 2010, **66**, 12-21.
33. Gasteiger, E., et al., Protein identification and analysis tools on the ExPASy server. 2005: Springer.

34. Chauviac, F.X., et al., Crystal structure of reduced MsAcg, a putative nitroreductase from Mycobacterium smegmatis and a close homologue of Mycobacterium tuberculosis Acg. J. Biol. Chem. 2012, **287**, 44372-83.
35. Haynes, C.A., et al., Structures of nitroreductase in three states: effects of inhibitor binding and reduction. J. Biol. Chem. 2002, **277**, 11513-20.
36. Hou, F., et al., Structure and reaction mechanism of a novel enone reductase. FEBS J. 2015, **282**, 1526-37.
37. Cortial, S., et al., NADH oxidase activity of Bacillus subtilis nitroreductase NfrA1: insight into its biological role. FEBS Lett. 2010, **584**, 3916-22.
38. Couturier, J., et al., In the absence of thioredoxins, what are the reductants for peroxiredoxins in Thermotoga maritima? Antioxid. Redox Sign. 2013, **18**, 1613-22.
39. Choi, J.W., et al., Crystal structure of a minimal nitroreductase, ydjA, from Escherichia coli K12 with and without FMN cofactor. J. Mol. Biol. 2008, **377**, 258-67.
40. Martinez-Julvez, M., et al., Structure of RdxA--an oxygen-insensitive nitroreductase essential for metronidazole activation in Helicobacter pylori. FEBS J. 2012, **279**, 4306-17.
41. Crosson, S. and K. Moffat, Structure of a flavin-binding plant photoreceptor domain: insights into light-mediated signal transduction. Proc. Natl. Acad. Sci. USA 2001, **98**, 2995-3000.
42. Losi, A., The bacterial counterparts of plant phototropins. Photochem. Photobiol. Sci. 2004, **3**, 566-74.